The Effect of Nanoscale Structure on Interfacial Energy

by

Jeffrey James Kuna

B.S. Mechanical Engineering
Northwestern University, 2004

SUBMITTED TO THE DEPARTMENT OF MATERIALS SCIENCE AND ENGINEERING IN PARTIAL FULFILLMENT OF THE REQUIREMENTS FOR THE DEGREE OF

DOCTOR OF PHILOSOPHY IN MATERIALS SCIENCE AND ENGINEERING

at the
MASSACHUSETTS INSTITUTE OF TECHNOLOGY

February 2011

Signature of Author: _____
Department of Materials Science and Engineering
January 12, 2011

Certified by: _____
Francesco Stellacci
Professor of Materials Science and Engineering
Thesis Supervisor

Accepted by: _____
Christopher Schuh
Chair, Departmental Committee on Graduate Students

The Effect of Nanoscale Structure on Interfacial Energy

Jeffrey James Kuna

Abstract

Interfaces are ubiquitous in nature. From solidification fronts to the surfaces of biological cells, interfacial properties determine the interactions between a solid and a liquid. Interfaces, specifically liquid-solid interfaces, play important roles in many fields of science. In the field of biology, interfaces are fundamental in determining cell-cell interactions, protein folding behavior and assembly, and ligand binding. In chemistry, heterogeneous catalysts greatly increase reaction rates of reactions occurring at the interface. In materials science, crystallization and the resulting crystal habit are determined by interfacial properties, and interfaces affect diffusion through polycrystalline materials. In nanotechnology, much work on self-assembly, molecular recognition, catalysis, electrochemistry and numerous other applications depends on the properties of interfaces.

The structure and properties of interfaces have been studied experimentally using a variety of techniques including various forms of microscopy, wetting measurements, and scattering techniques. Conventionally, the typical interface considered was highly homogeneous and exhibited a uniform composition and roughness. In contrast, many of the interfaces encountered in biological or nanotechnological systems have surfaces with a greater degree of complexity. While the surface may be compositionally homogeneous over a large area, these surfaces are structured and have a complex surface topology. On a mixed interface, several different chemical groups may be present on the surface, and the chemical composition can vary on a sub-nanometer length scale.

Structured systems are inherently difficult to experimentally measure. Most techniques available to characterize interfaces average properties over the entire surface and are not sensitive to nanoscale variations. Furthermore, many of these techniques are incapable of distinguishing global, surface-dependent properties from artifactual influences. Many surface characterization techniques require a large, flat, smooth surface. Preparation of mixed interfaces is an experimental challenge as well as many mixed interfaces with nanoscale structure are present on objects that are themselves nanoscale, such as proteins. Several technological hurdles exist that limit the ability to produce nanoscale mixed interfaces large enough for conventional measurements.

In this thesis, the effect of surface structure on wetting behavior was investigated. Interfaces can be characterized by the energy required to form them, a quantity called interfacial energy. Models have been developed to describe the interfacial energy of mixed interfaces for a wide range of surfaces. These models only account for the composition of the surface. The wetting behavior of mixed surfaces has also been related to artifact-dependent wetting effects (namely the effect of a boundary or asperity). No attempt has been made to incorporate surface structure into a global expression of interfacial energy.

This thesis will study how the structure of an interface determines the resulting interfacial energy. Surfaces prepared with chemical domains of different length scales demonstrate and interfacial energy trend with significant deviation from the current best model. Specifically, the observed trend is non-linear, unlike the conventional model, and furthermore in some cases, is non-monotonic. These deviations are shown to stem from the surfaces' intrinsic structure and are not an artifact of the measurement process or surface defects.

The deviations from the predicted trend are explained by the molecular scale structure of the solvent. The two proposed mechanisms, cavitation and confinement, arise when surface features are smaller than a solvent-dependent length. With cavitation, non-wetting surface features below a size threshold are more wetting than would be expected. With confinement, wetting patches become less wetting as their dimensions are decreased. Molecular dynamics simulations support the proposed mechanisms. Additional experimental results provide further experimental evidence of the proposed molecular-scale wetting phenomena.

Thesis advisor: Francesco Stellacci

Contents Overview

Chapter 1: Introduction to Interfacial Energy 9

Chapter 2: Interfacial Energy of Patchy Surfaces 48

Chapter 3: The Experimental Systems and Methods 60

Chapter 4: Experimental Results 86

Chapter 5: The Breakdown of Cassie-Baxter Theory and Considerations for a New Theory 105

Chapter 6: Conclusions and Future Work 124

Appendix: Experimental Methods 134

Biographical Note 138

Table of Contents

Chapter 1: Introduction to Interfacial Energy 9
- 1.1 Introduction 9
- 1.2 Interfacial Energy 9
- 1.3 Surface Energy vs. Interfacial Energy, the Work of Adhesion and other Definitions 14
- 1.4 Thermodynamic Treatments of Interfacial Energy 16
- 1.5 The Origin of Interfacial Energy: Intermolecular Forces 23
- 1.6 Relating Experiment to Theory 31
- 1.7 Extending Young's Equation 34
- 1.8 Experimental Determination of Interfacial Energy 39
- 1.9 Measurement Difficulties: Hysteresis and Pinning 40
- 1.10 Conclusion 44
- 1.11 References 45

Chapter 2: Interfacial Energy of Patchy Surfaces 48
- 2.1 Interpretation of Contact Angle and the Three-Phase Line 48
- 2.2 Self-Assembled Monolayers as Model Patchy Surfaces 51
- 2.3 Molecular Scale Patchiness 54
- 2.4 Statement of Research 56
- 2.5 References 58

Chapter 3: The Experimental Systems and Methods 60
- 3.1 Preparation of Model Heterogeneous Surfaces 60
- 3.2 Self-Assembled Monolayers 61
- 3.3 Introduction to Gold Nanoparticles 63
- 3.4 Purification Methods 67
- 3.5 Phase Separation with a Nanoparticle's Monolayer 69
- 3.6 Characterization Methods for Nanoparticles 76
- 3.7 Production of Films of Nanoparticles 78
- 3.8 Methods Used to Determine Interfacial Energy 80
- 3.9 References 83

Chapter 4: Experimental Results 86
- 4.1 Preparation of Surfaces with Large Domains 86
- 4.2 Wetting Behavior of Surfaces with Large Domains 88
- 4.3 Synthesis of MHol/OT Nanoparticles 90
- 4.4 Preparation of Nanoparticle Films 91
- 4.5 Wetting Behavior of Surfaces with Molecular Domains 94
- 4.6 MUDol/OT Nanoparticle Films 96
- 4.7 Exploring Films with Other Chemistries 97
- 4.8 Results 99
- 4.9 References 103

Chapter 5: The Breakdown of Cassie-Baxter Theory and Considerations for a New Theory 105
5.1 The Need for a New Theory 105
5.2 A General Framework 106
5.3 Cavitation and Solubility of Small Hydrophobic Objects 108
5.4 Confinement: Liquid in Narrow Spaces 111
5.5 Competing Interactions 113
5.6 Molecular Dynamics Simulations of Interfacial Water 114
5.7 Experimental Confirmation 119
5.8 References 122

Chapter 6: Conclusions and Future Work 124
6.1 Conclusion 124
6.2 Future Experimental Directions 125
6.3 Extending the Work Computationally 129
6.4 Link to Biology 130
6.5 Technological Applications 132
6.6 References 133

Appendix: Experimental Methods 134
Biographical Note 138

Figures and Illustrations

1.1 Interfacial Energy Examples....11
1.2 Work of Adhesion/Cohesion....15
1.3 Tolman's Model....19
1.4 Fowkes' Model....25
1.5 Spreading Coefficient....27
1.6 Young's Equation....32
2.1 Contact Line Caveats....50
2.2 Monolayer Structure....51
2.3 Monolayer C.A Length Invariance....52
2.4 CB Theory and Monolayers....53
2.5 Hydrophilic Patches....55
2.6 Protein Interfaces....56
3.1 Monolayer Formation....61
3.2 Monolayer Phase Separation....63
3.3 Nanoparticle Monolayer Phase Separation....70
3.4 Nanoparticle Monolayer Morphology....71
3.5 Nanoparticle Monolayer Simulations....72
3.6 Phase Separation Driving Force....72
3.7 Nanoparticle Solubility....75
3.8 Nanoparticle Interfacial Energy Simulations....76
3.9 SAM-AFM....81
4.1 MHol/OT Contact Angle Results....88
4.2 SAM Morphology and AFM/CA Correlation....90
4.3 NP Films....93
4.4 MHol/OT W_{sl}....94
4.5 MHol/OT W_{sl} CA and AFM Correlation....95
4.6 MUDol/OT W_{sl}....96
4.7 Charged NP Films....99
5.1 Interfacial Density Profiles....107
5.2 Cavity Formation Energy....111
5.3 MD Models....115
5.4 MD Density Profiles....116
5.5 MD Density Profiles....117
5.6 Averaged Domain Densities....118
5.7 Linear Deviations at 0M and 3M NaCl....121

Tables

4.1 Nanoparticle Size Distribution....88
4.2 Nanoparticle Film Roughnes....93

Acknowledgements

I would like to acknowledge and thank my advisor, Francesco Stellacci, for his guidance, support, and inspiration throughout my studies. He has taught me much, and it was a pleasure to work with him.

Additionally, I enjoyed collaborating with Kislon Voïtchovsky. His AFM expertise bolstered my own experimental claims, and I learned a lot from our frequent discussions.

The members of SuNMaG have always been friendly and supportive. In particular, Benjamin Wunsch has been an excellent friend and co-worker. He was always eager to discuss and diagnose issues with chemistry. It was also a pleasure to work with Osman Bakr and Jin Young Kim who provided help with TEM. Additionally, Randy Carney and I often discussed preparation of charged ligands and charged nanoparticles.

Finally, I thank my family. I would especially like to thank my mother for her support and encouragement. I would not be where I am today without my first chemistry set, countless electrical parts, and frequent trips to the library.

Chapter 1: Introduction to Interfacial Energy

1.1 Introduction

Interfacial energy is a commonly encountered thermodynamic concept that plays a fundamental role in a wide range of fields due to the ubiquity of interfaces themselves. In materials science, interfacial energy determines crystalline shape, the movement of grain boundaries, and surface reconstruction. It is an important parameter in the formation and stability of emulsions and colloids. In biology, interfacial energy controls membrane structure, and many biological self-assembly processes are driven by interfacial energy. Interfacial energy is also important in tribology and fluid mechanics where it dominates the formation of thin liquid films and capillary flow.

Several theories have been developed to calculate the interfacial energy of specific systems. As the field of material science rapidly grows, models for calculating interfacial energy given a surface's properties must be developed. Current best models of general systems only incorporate surface composition and roughness. Especially in the fields of nanotechnology and biology where surfaces are commonly highly complex and not adequately described using few parameters, new treatments for interfacial energy must be developed to deal with nuances of surface structure.

1.2 Interfacial Energy

Interfacial energy is defined as the energy per unit area required to extend an interface between two dissimilar materials. In introductory thermodynamics and fluid mechanics textbooks[1,2], this term is often presented as an intrinsic property of an interface, γ, and is

simply treated as the intensive property associated with the extensive property of interfacial area, as shown in the example expression for the variation in energy of a two component system in eq. 1.1 below:

$$dG = pdV - sdT + \mu dN_1 + \mu dN_2 + \gamma dA \tag{1.1}$$

The value γ is treated as a constant whose value depends on the identities of the materials in contact, with more detailed treatments including the identity and concentration of species adsorbed to the interface, if any.

In the field of materials science, the assignment of a single, constant value to interfacial energy is universal. In treatments of nucleation, we find the enthalpic driving force associated with the formation of bonds offset by the cost of forming an interface.[3] In simple treatments, the interfacial energy of the forming nuclei is giving a constant value. In another topic central to the field of materials science, our understanding of crystal growth relies heavily on interfacial energy. Rather than assigning a solitary interfacial energy to a crystal that is dependent on the identities of the two abutting materials, consideration for the crystallographic orientation of the exposed facets must be considered.[3,4] The interfacial energy of the entire crystal then, must be decomposed as the sum of the interfacial energies of each facet. The crystallographic orientation defines the density of the energy of dangling bonds present, and in turn the relative stability and resulting growth behavior of the crystal facets.

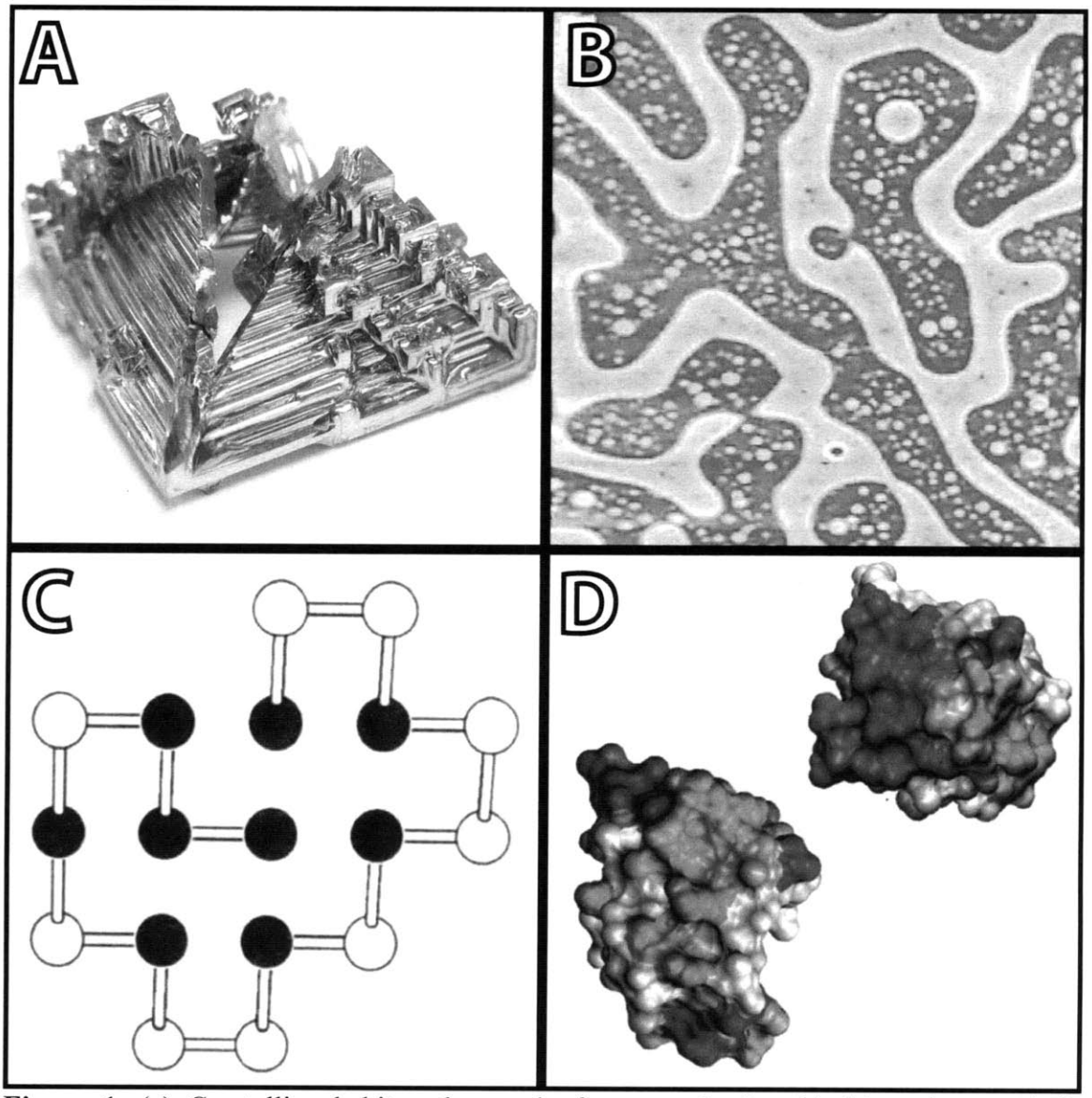

Figure 1. (a) Crystalline habit and growth, for example for this bismuth crystal, is determined by minimization of interfacial energy. (b) Under certain conditions, a mix of polymers can separate, or demix, driven by interfacial energy. Here a spun-cast film of polystyrene and poly(methyl methacrylate) form a striking pattern after demixing.[5] (c) Protein folding is another natural process driven by interfacial energy. In conceptual 2-dimensional lattice models[6], hydrophilic residues (black beads) aggregate in the protein's interior while hydrophilic groups (white beads) adorn the exterior. (d) An actual protein has a far more complex surface, however. Here, hydrophobin is shown from two angles.[7] The shading represents hydrophobic groups (blue), hydrophilic groups (red) and intermediate groups (white). (Images taken from sources without permission, with the exception of (a), taken from wikimedia.org under the Creative Commons license.)

Interfacial energy also plays a vital role in another area of materials science—colloidal systems and dispersions, and largely determines their formation, resultant stability and

coalescence behavior.[8,9] Here, interfacial energy is again treated as a function of the identities of the two abutting materials. However, since surfactants are commonly present at these interfaces and exhibit a large impact on interfacial energy, the role of the surfactant is included in the expression for interfacial energy as a function of concentration and the identity of the surfactant.[10,11] It is important to note that because in general the surfactants present at the interface largely lack structure and are randomly distributed, the interfacial energy can again be treated isotropically with satisfactory results. In more complex surfactant systems, especially those involving multiple components, interfacial energy is approached as a function of the components' identities and concentrations, and curvature of the interface.[12-14] Interestingly, we note that the importance of a structural parameter can be seen in these systems: surfactants individually are viewed as having a structure, and not simply as point-like objects. Thus we see a nascent understanding that orientation of these objects is important and that each component (hydrophilic head and hydrophobic tail) is seen as distinct and, at least conceptually, having two different interfacial energies.

Another field in materials science where interfacial energy plays a prominent role is polymer science. Mixtures of polymers may undergo morphological changes driven by differences in interfacial energy in polymer demixing.[5,15] Here the polymer chains phase separate to reduce total interfacial energy. Much recent work has been focused on designing block copolymer systems that spontaneous self-assemble to generate a large variety of patterns and shapes as a foundation for more complex assemblies.[16-19]

Within the field of biology, the infamously difficult question of protein folding can be reduced to an attempt to minimize interfacial energy. In early conceptual models of the progression of protein folding[20-23], each residue, or amino acid, of a protein was labeled as either hydrophobic or hydrophilic, or equivalently, low- or high-interfacial energy. The interfacial energy of the entire protein was sequentially reduced by folding the protein to reduce the total number of residues exposed while maximizing the ratio of hydrophilic residues to hydrophobic residues on the exterior.[22] While this model is simpler than the more complex computational models developed since, it is the common intuitive model for protein folding. Furthermore, the idea of grading each residues' relative hydrophobicity or hydrophilicity, or hydropathy, individually is still common today[24,25], and has been refined via the development of a numeric hydropathy scale that quantitatively relates the residues.[23,26] A common method of presenting the morphology of a protein displays a mesh of the surface accessible surface area of the protein which is colored based on the relative hydrophilicity of the nearest residue.[27]

The conceptual insight to treat interfacial energy per residue was the key to beginning to understand the behavior of these complex systems. The growing complexity of a system under study is often accompanied by a decrease in the surface homogeneity. For such systems, especially those whose structure and function are strongly dependent on interfacial energy, the assumption of a constant interfacial energy for the entire system becomes questionable and the importance of structure in interfacial energy becomes apparent. Biological systems are inherently patchy at the molecular scale and many artificial systems are beginning to exploit such patchiness to direct self-assembly and

control material behavior.[28] Just as an understanding of crystallographic growth would have been impossible for not the insight that the crystallographic orientation of a crystal's facet determines interfacial energy in addition to the composition of the crystal, a thorough understanding of the behavior and design of materials with structured interfaces is impossible without the development of a theory of interfacial energy that includes structural information.

1.3 Surface Energy vs. Interfacial Energy, the Work of Adhesion and other Definitions

Before further examining the theoretical development of interfacial energy, it would be helpful to define and demonstrate several terms and the thermodynamic relations between them. The materials used to develop these descriptions must be assumed to be isotropic and continuous, but may be taken to be liquids, gases, or solids, with the only exception that interfaces cannot exist between two gases.

The work of cohesion of a material, denoted W_{11}, is defined as the work required to divide a material to produce two new surfaces of unit area in a vacuum (Fig. 2). As this produces two new units of area of surface, half of the work of cohesion is equal to the surface energy (γ_1) of the material. If two dissimilar materials are separated, the energy per unit of area is defined as the work of adhesion (W_{12}). Whereas the surface energy depended on the identity of one material, the work of adhesion is a function of the identity of two materials.

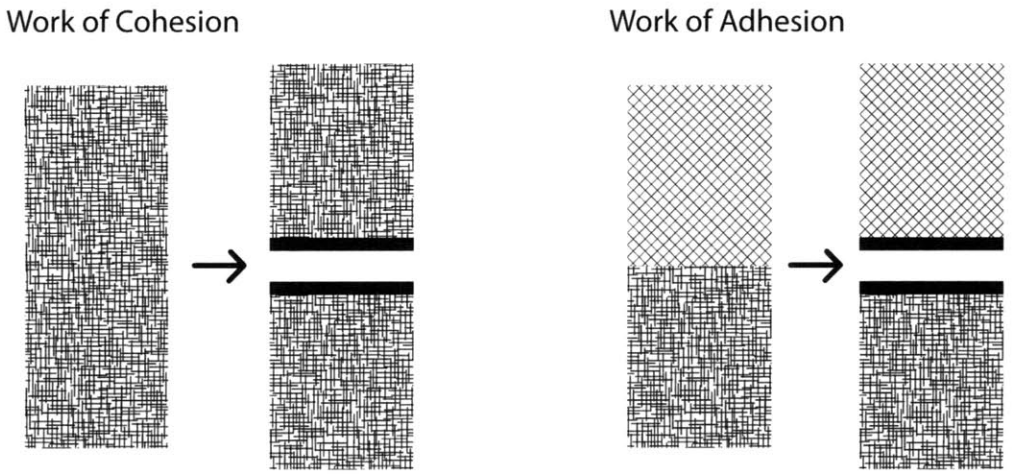

$$W_{11} = 2\gamma_{11} \qquad W_{12} = \frac{1}{2}W_{11} + \frac{1}{2}W_{22} - \gamma_{12}$$

$$\gamma_{11} = \frac{1}{2}W_{11} \qquad \gamma_{12} = \gamma_{11} + \gamma_{22} - W_{12}$$

Figure 2. The work of cohesion (left) is the energy required to separate a material from itself to generate 2 new units of surface area. The energy required is twice the surface energy. The work of adhesion (right) is the energy required to separate two distinct materials. The work of adhesion is the difference between the sum of the materials' surface energies and their interfacial energy.

Interfacial energy is defined as the energy per unit area required to produce an interface between two materials. The expression for interfacial energy is:

$$\gamma_{12} = \gamma_1 + \gamma_2 - W_{12} \tag{1.2}$$

where γ_1 and γ_2 are the surface energies of each material, and W_{12} is the work of adhesion for the two materials. To understand the origin of this expression, it is important to consider the formation of an interface in vacuum. To form an interface, a unit area of each material must first be created; this energetic cost is simply the sum of the surface energies of each material. The attractive interaction between these new surfaces upon joining them to form the interface performs work (W_{12}). Thus the energy required to form an interface is equivalent to the difference between the work required to form the

individual surfaces and the work returned to the system upon joining them. In this thesis, the interaction between a liquid and a solid will be expressed in terms of the work of adhesion rather than reporting the interfacial energy directly, due to the direct applicability of the Young-Dupré equation (Eq. 1.21) and its specificity in describing the attractive interactions. The interfacial energy may be viewed as an expression with two terms that describe the individual materials and a third term, the work of adhesion, that captures the interaction between these materials.[8]

As a final note: surface tension and interfacial tension are commonly conflated. The surface tension (or surface energy) of numerous materials is often presented in literature but it is important to remember that unless the measurements were performed under vacuum, the measured values more accurately describe the interfacial tension (or energy) of the interface between the material and the ambient atmosphere. Interfacial tension is thus a more apt term, but it is commonly reserved for the tension of an interface between two liquids.[8]

1.4 Thermodynamic Treatments of Interfacial Energy

J. W. Gibbs was the first to develop a thermodynamic model of the behavior of interfaces. While significant advances have been made in the knowledge of interfaces, Gibbs' concepts are still commonly referenced and are the foundation of all current theory.[8,29-31] Gibbs' conceptual model of an interface was an infinitesimally thin layer between two phases that could be described by its area and curvature. On either side of this layer, or dividing surface, the materials are homogeneous and uniformly distributed

and at the dividing surface itself, an abrupt transition from one material to the other occurs. The interfacial tension would act in plane at this dividing surface.[32]

Such a model necessarily contains several assumptions, and it is important to note these assumptions and how they impact the nature of the interface. First, and most obviously, the interface itself has no structure—it is not a volume but a geometric boundary. Second, by assuming both substances are homogeneous, the interface is entirely isotropic and therefore does not contain structure. Finally, this treatment neglects the molecular nature of the materials and the nature of the interactions between molecules of the same and different phases.

In 1937, Fowler attempted to incorporate the concept of intermolecular forces into a theory of interfacial tension.[33] His theoretical system was a planar interface of a vapor in contact with a liquid. An analytical expression was developed for the surface tension that required knowledge of the potential between two particles in the system and the distribution function of each material. This formulation was shown to yield a poor approximation of the surface tensions of argon and mercury. He conjectured that interfacial tension might depend on structure within the liquid. In the example given, this structure was conjectured to be highly ordered and crystalline in nature, with planes of varying bond density. Such structure does not exist in liquids and is relevant only to solids. This treatment attempts to incorporate intermolecular forces, but it still assumes an isotropic and homogeneous interface.

R. C. Tolman returned to a purely thermodynamic treatment and refined Gibbs approach by considering the structure of the interface.[31] This conceptual model is especially notable because it serves as the basis for a majority of refinements made since to the structure of a liquid interface.[34] Rather than confining the transition between phases to occur abruptly at a dividing surface, in Tolman's model, the transition occurs over a finite volume whose thickness was conjectured to be on the order of several molecular diameters. Within this transition region, the properties of each phase would deviate from the bulk properties as the dividing surface is approached. This treatment is more robust as it accounts for the finite extent of the interface, but cannot itself provide a means of describing the structure of the interface.[31]

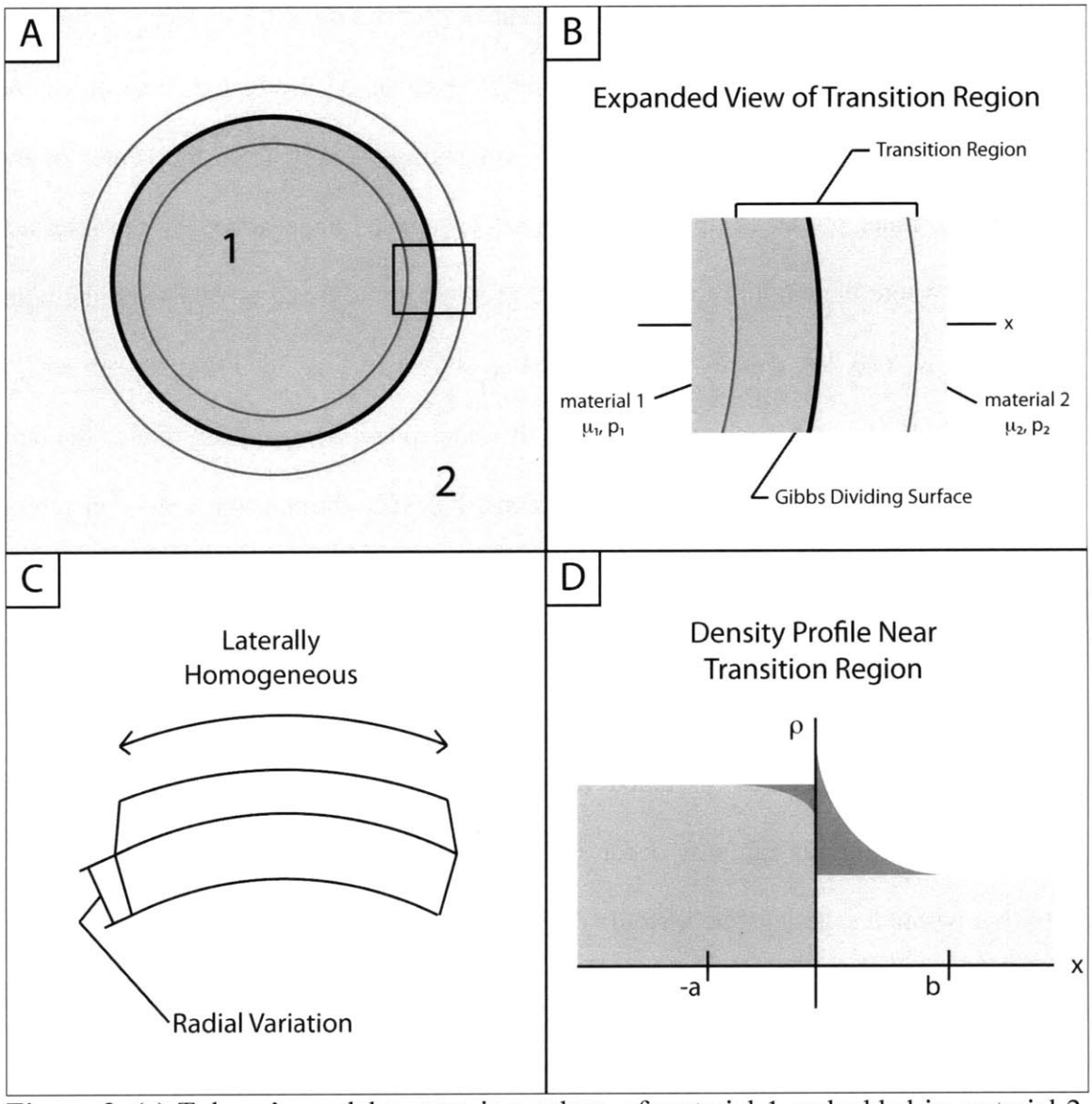

Figure 3. (a) Tolman's model system is a sphere of material 1 embedded in material 2. (b) The dividing surface separates the two materials. The interface is assumed to not be diffuse. (c) The system exhibits spherical symmetry. Any variation occurs only along the outward direction. Variations within spherical shells are not accounted for with this treatment. (d) Along the radially axis, variations in the material density is allowed to occur. Hypothetical deviations from the bulk density of each material, indicated as the gray shaded regions, are shown as colored regions.

Tolman's theory is based on a two-phase system with spherical symmetry, as shown in Fig. 3a. A closer view of the interface is shown in Fig. 3b. The dark line is the dividing surface. As the transition occurs over a finite distance, there exist multiple ways to define the location of the dividing surface, and its location is selected to simplify the

mathematics. For this system, regardless of selection of the dividing surface, all surfaces will be spherical shells, and will lie parallel to each other. Here, the location of the dividing surface is taken as x=0 on an axis emanating radially from the center of the system. The inner phase, composed of material 1, remains unperturbed by the interface until x=-b, where the equilibrium density and pressure are allowed to vary from the bulk. From x=-b to x=0, the density profile varies as shown in Fig. 3d. From x=0 to x=a, a similar region exists where the properties of the outer phase deviate from that of the bulk at equilibrium. Fig. 1d illustrates what the density profile through the transition region might look like. The gray shaded profiles represent the density profiles of each phase (material 1 on the negative x-axis, material 2 opposite) if the phases remained homogenous. The red and green shaded profiles represent the density deficiency or excess. From the geometry assumed in this treatment, namely spherical symmetry, variations in the liquids can only occur radially. As defining a surface with structure, or variation within a spherical shell, would defy the assumptions made in this treatment, this approach is unsuitable for describing interfaces at structured surfaces. It is however a convenient model to explain simple, homogeneous surfaces.

It is instructive to compare Tolman's treatment of the interface with the expression for the interfacial energy (Eq. 1.2). In Tolman's model, the system is comprised of a homogenous sphere of material 1 embedded in a homogeneous phase of material 2. The systems total energy can be expressed as the sum of the energy of each phase: $E_1 + E_2$. When the transition layer is allowed to form, a correction term E_s is added to the total energy. This derivation neatly parallels the derivation of and expression for interfacial

energy (Eq. 1.1) in terms of surface energies and the work of adhesion presented in the previous section. The work of adhesion does not only reflect the attractive forces between the surfaces, but also includes the work done when the interface restructures. The E_s term in Tolman's theory, however, should not be interpreted as the energy of the transition region, but rather must be viewed as the energetic deviation upon relaxation from the system containing the non-relaxed, abrupt interface.

Tolman found that a necessary condition for equilibrium was

$$\mu_i + \phi = const. \tag{1.3}$$

where μ_i is the intrinsic chemical potential of component i and ϕ is the potential due to external forces field. The forces experienced are the intermolecular forces present between molecules of the same phase, and between the two phases. Furthermore, if μ_i is defined as

$$\mu_i = \psi + \frac{p}{\rho} \tag{1.4}$$

where ψ is the Helmholtz free energy, p is the pressure, and ρ is the density, after substitution, taking the derivative with respect to position, and substituting $f_x = d\phi/dx$ we find the expression:

$$\frac{d\psi}{dx} - \frac{p}{\rho^2}\frac{d\rho}{dx} + \frac{1}{\rho}\frac{dp}{dx} + \frac{d\phi}{dx} = 0 \tag{1.5}$$

The imbalance of forces near the interface is responsible for changes in density and pressure in the transition region. Away from the transition region, the potential due to intermolecular forces is constant and Eq. 1.4 reduces to μ_i=*const.* The physical origin of

the interfacial energy or tension can now be succinctly stated: unbalanced forces acting on the fluid at the interface change the local density from that of the bulk material, and this altered density in turn changes the average cohesive force at the interface, the sum of which is the interfacial tension.

The thickness of the transition region, even at the time Tolman formulated his theory, was known to be only a few molecular diameters. The applicability of thermodynamic concepts is questionable over such minimal extents, especially when large variations occur. The thermodynamic treatment rendered by Tolman did not provide an understanding of the actual structure of the liquid interface, and such a conceptual understanding would require the development of a theory that could incorporate molecular theory.

A statistical mechanical basis for surface tension was developed in 1949 by Kirkwood and Buff[30] that incorporated the variations in density local to the interface. Similar to Fowler, they utilized a planar interface separating two fluid phases. While they did permit variations from the bulk density, they assumed the density only varied as a function of distance from the dividing plane. Interfacial tension was calculated as the stress acting at the interface necessary to offset the pressure variations that would occur in each phase if the interfacial tension were not present. The expression for interfacial tension is similar to an expression developed by Tolman,

$$\gamma = \int_{-\infty}^{\infty} p - p'(z)dz \tag{1.6}$$

The authors are careful to point on that an assumption made by Tolman, that the pressure p'(z) can be equated to the pressure of the bulk material at the same density, is inaccurate and must be treated using statistical mechanics. While the Kirkwood-Buff theory is capable of reproducing the same results as Fowler by reducing the transition region to a plane, it is more general since it makes no stipulations of the region local to the dividing surface. The theory is shown to reproduce the findings of Tolman, as well as approximate the surface tension of liquid argon.[30]

More recent numerical treatments have built on the knowledge of the interfacial structure. Notably, several attempts to clarify the density profile of gas/liquid and liquid/liquid interfaces using Monte Carlo or molecular dynamics simulations have been made. The success of these attempts is strongly dependent on the accuracy of the force field used. Additionally, the impetus behind many studies in this area is greater knowledge of the nature of liquid/vapor phase transitions, and not the measurement of mechanical properties such as interfacial tension.[34]

1.5 The Origin of Interfacial Energy: Intermolecular Forces

Even the earliest treatments of interfacial energy identified the lack of symmetry and the resulting force imbalance at the interface as the cause of interfacial tension. In the prior century, significant work has been directed at cataloguing and explaining the varieties of forces that can exist between molecules. All of the intermolecular forces are electromagnetic in origin and stem from interactions between dipoles or charges. A liquid whose molecules contain permanent dipoles is said to be a polar liquid, whereas a liquid that does not is termed non-polar. Non-polar liquids and polar liquids alike can

experience van der Waals forces due to fluctuations in the distribution of charge resulting in temporary dipoles, while interactions between two permanent dipoles (Keesom forces) and permanent and induced dipoles (Debye forces) require either both or one of the molecules to be polar.[8]

As the interfacial tension is so strongly determined by the nature and strength of the forces acting at the interface, efforts were made to decompose the interfacial tension according to the forces responsible. One early and rather successful attempt was made by Fowkes, who regarded interfacial tension as the sum of several components, each attributable to a class of forces.[35] For instance, the interactions present in liquid mercury could be classed as either metallic bonds or dispersion forces. In water, the interactions were either dispersion forces or polar interactions, which included hydrogen-bonding effects. As hydrocarbons are a non-polar liquid, their interfacial energy is wholly attributable to dispersion forces and only contains this one term.

$$\gamma_{Hg} = \gamma_{Hg}^{m} + \gamma_{Hg}^{d} \tag{1.7}$$

$$\gamma_{H_2O} = \gamma_{H_2O}^{p} + \gamma_{H_2O}^{d} \tag{1.8}$$

$$\gamma_{HC} = \gamma_{HC}^{d} \tag{1.9}$$

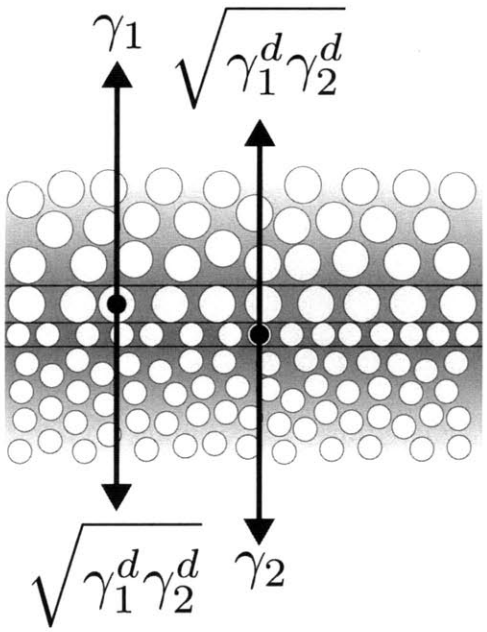

Figure 4. Fowkes' model of a liquid-liquid interface assumes an interface comprised of two monolayers of each liquid (demarcated by horizontal lines). Each monolayer experiences two forces: one toward their respective bulk, equivalent to the surface energy and a second toward the interface due to dispersive forces, with the magnitude as calculated by the Berthelot relation.

Fowkes employs a simplistic model of the interface as two abutting monolayers of liquid backed by their respective bulk phases. The interfacial tension is taken to be the sum of the attractive forces parallel to the dividing surface experienced within each monolayer of liquid (see Fig. 4). If one of the materials is taken to be non-polar, the only interaction that can occur between the two materials are van der Waals forces. The magnitude of this interaction is taken to be the geometric mean of each phase's dispersion component by the Berthelot relation. (In a similar route, Girifalco and Good[36] had previously attempted to calculate the work of adhesion directly from two materials' interfacial energy. This approach was unsuccessful as it ignored the nature of the interactions present.) In this model, each monolayer would experience its full surface tension drawing it toward the bulk and the dispersion interaction previously calculated drawing it toward the dividing

plane. Summing the contributions for both monolayers yields the total energy of the interface:

$$\gamma_{12} = \gamma_1 + \gamma_2 - 2\sqrt{\gamma_1^d \gamma_2^d} \tag{1.10}$$

Here the superscript denotes the fraction of surface energy from dispersive interactions. While this derivation oversimplifies the structure of the interface and liberally employs the surface energy as an additive force, the resulting expression is useful to examine as it parallels the expression given for the interfacial energy, with the work of adhesion given by the attractive force explained previously, $^2\sqrt{\gamma_1^d \gamma_2^d}$. Experimentally, this formulation was tested by measuring the spreading of various hydrocarbons on water and mercury. Spreading occurs when wetting a surface is so favorable the contact angle is nonexistent, causing a drop to spread completely wetting the surface. With a hydrocarbon (HC) on water, this will only occur if the surface tension of water is greater than the sum of the surface tension of the hydrocarbon and the interfacial tension of their interface (see Fig. 5), or more succinctly if:

$$\gamma_{H_2O} - (\gamma_{HC} + \gamma_{H_2O/HC}) > 0 \tag{1.11}$$

The expression on the left hand side is termed the spreading coefficient and its sign indicates whether or not spreading would occur. By applying the previous equation (Eq. 1.10) to simplify the spreading coefficient, an efficient method of quantifying the dispersion component of water emerges. Note that this simplification is possible because it is assumed the surface tension of hydrocarbons is purely due to dispersive interactions. If the simplified coefficient is positive,

$$2\sqrt{\gamma_{HC}\gamma^{d}_{H_2O}} - \gamma_{HC} > 0 \tag{1.12}$$

spreading will occur. Indeed, the hydrocarbons with surface tensions less than $\gamma^{d}_{H_2O}$, 21.8 dynes/cm, are found to spread.[37] Curiously, it was also found that this relation only held true for purely aliphatic hydrocarbons. Aromatic hydrocarbons were found to interact with water more strongly than would be expected from purely van der Waals interactions. As aromatics are more polarizable than aliphatics, dipole-induced dipole related forces would be expected for these solvents.[8]

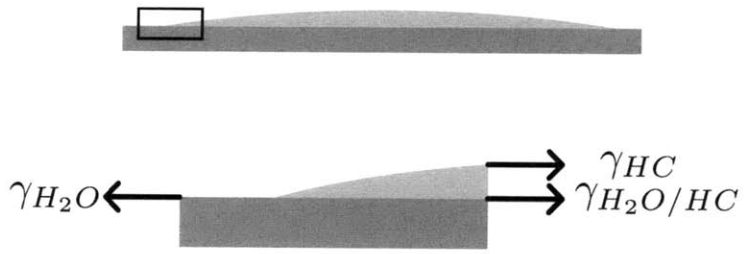

Figure 5. The sign of the spreading coefficient determines if a liquid will spread on a liquid surface. It is derived by consideration of the forces acting on the three-phase line. For a very wetting liquid with a negligible contact angle, the interfacial tensions act in the same plane leading to Eq. 1.11.

The concept of spreading was also central to an attempt to understand the wettability of solid surfaces by Zisman.[38] Spreading on a solid surface occurs when the contact angle of a drop is zero, or equivalently when its cosine is one. If spreading occurs, a liquid drop would spontaneously spread to cover the surface; this state is termed complete wetting. By plotting the cosines of the contact angle for various hydrocarbon liquids on a given surface against their surface tensions, the surface tension when complete wetting begins could be extrapolated. As the liquids used were mostly aliphatic hydrocarbons (namely n-alkanes), the discrepancy that would occur when using polar solvents was not readily

apparent. Due to the number of interactions between a liquid and solid (H-bonds, polar forces, dispersion forces), the wetting behavior of a solid cannot be reduced to a single parameter, such as the critical wetting surface tension.

Owens and Wendt continued the analysis of Fowkes, and extended it to interfaces between phases which can interact via hydrogen bonding in addition to dispersion forces.[39] In this case, the surface tension of water could be written as:

$$\gamma_{H_2O} = \gamma^d_{H_2O} + \gamma^p_{H_2O} \tag{1.13}$$

Using twice the geometric mean of each component as before, the work of adhesion can be expressed as:

$$\gamma_{sl} = \gamma_s + \gamma_l - 2(\sqrt{\gamma^d_s \gamma^d_l} + \sqrt{\gamma^h_s \gamma^h_l}) \tag{1.14}$$

where the final term represents the work of adhesion. Here, the subscript represents the phase (s=solid, l=liquid). If no superscript is present, the term represents the total surface energy. Otherwise, the superscript represents the surface energy component due to dispersive (d) or hydrogen-bonding (h), interactions. By using two different solvents that are fully characterized, i.e. the dispersion and hydrogen-bonding components of each liquid are known, measurements of the liquids' contact angles on a solid surface can be used to calculate the dispersion and hydrogen-bonding components of the surface. In the original publication, this method is shown to provide reasonable values.

Later work sought to refine the calculation of the interactions at the interface. The classification of a material's ability to hydrogen bond by a single coefficient is rather

inaccurate. It is well understood that hydrogen bonding occurs between a hydrogen bond donor and a hydrogen bond acceptor, and that a substance's ability to perform one role is not equivalent to the ability to perform the other. Therefore, a further distinction must be made in the decomposition of the surface energy terms to describe attractive interactions of a substance due to its role as a hydrogen bond donor or acceptor.[40,41] This further specification appears as another term in the interfacial energy:

$$\gamma_{12}^{AB} = 2(\sqrt{\gamma_1^+\gamma_1^-} + \sqrt{\gamma_2^+\gamma_2^-} - \sqrt{\gamma_1^+\gamma_2^-} - \sqrt{\gamma_1^-\gamma_2^+}) \qquad (1.15)$$

Here the subscript denotes the phase, and the superscript indicates the donor (+) and acceptor (-) components of the acid-base (AB) interaction. The necessity of clearly delineating the varieties of forces acting at an interface demonstrates that numerous factors must be taken into account and that the behavior of interfaces cannot be easily summarized by a single factor.[36,38,42]

Recent work has challenged the need to examine the forces operating at the interface and has supported the view that interfacial energy can be reduced to a single parameter. Kwok et al. has argued against the validity of decomposing the interfacial energy by nature of intermolecular forces and has instead claimed that the contact angle is solely indicative of the surface tension of the probe liquid. In a series of studies, the advancing contact angle of drops of numerous liquids on a silicon wafer coated with a fluorinated compound was measured. Of the 30 liquids studied, 9 displayed constant contact angles as the drop size increased while the remainder displayed stick-slip motion.[43] In another study by the same researchers, the interfacial tensions of immiscible liquids were studied to test the validity of Van Oss's approach. If a positive interfacial energy is calculated, it

was posited that the liquids should be immiscible, and vice versa. It was found that several liquid pairs with positive interfacial energies were in fact miscible.[44]

The spreading behavior of the first study is consistent with pinning of the three-phase line at defects on the surface. (See section 1.9.) From the published data, a large range of angles was observed[43], yet, for a given liquid, the minimum angle achieved when the drop becomes unpinned and advances, is essentially constant. This indicates the contact line pinning with the drop periodically relaxing to a non-pinned shape. Such measurements were excluded from Kwok's treatment, and only those that spread evenly were included. Furthermore, the use of a fluorinated substrate was a poor choice as fluorinated materials have unique interactions with both 'polar' and 'non-polar' materials. The second study[44] on miscibility is more experimentally sound but has theoretical pitfalls. While Van Oss suggests that the interfacial energy of two liquids can be estimated knowing the nature of the intermolecular interactions present, it is never suggested that such calculation is an exact form or that it can completely capture the behavior of the liquids at the interface. Finally, the assumption that two liquids will be miscible if the calculated interfacial energy is zero or negative is flawed as the entropic contribution to the free energy of mixing is completely ignored. For these reasons, this thesis will adopt the conventional view that the strength and nature of interactions at the interface are critical to understanding wetting behavior, and furthermore, wetting behavior cannot be summarized by a single parameter.

1.6 Relating Experiment to Theory

Several methods exist for determining the interfacial energy of a solid liquid interface. The most common is goniometry, where the angle of contact of a small drop is measured and from which the interfacial tension can be calculated. In addition, there exist force-based techniques that can directly measure interfacial tension by recording the force exerted upon a probe in contact with a liquid. This section concludes with a novel technique developed in the scope of this thesis that measures interfacial energy with a scanning probe microscope.

The original development of a measurement of interfacial energies was made by Young in 1805.[45] This method, commonly referred to as goniometry or more commonly contact angle measurements, is commonly used today. The basic technique can be described as thus: A drop of limited volume is placed upon a flat surface to be analyzed. Upon contact, the drop will attain an equilibrium angle with the surface. This angle is called the contact angle and describes the relative interfacial energies of the solid/liquid, solid/vapor, and liquid/vapor interfaces.

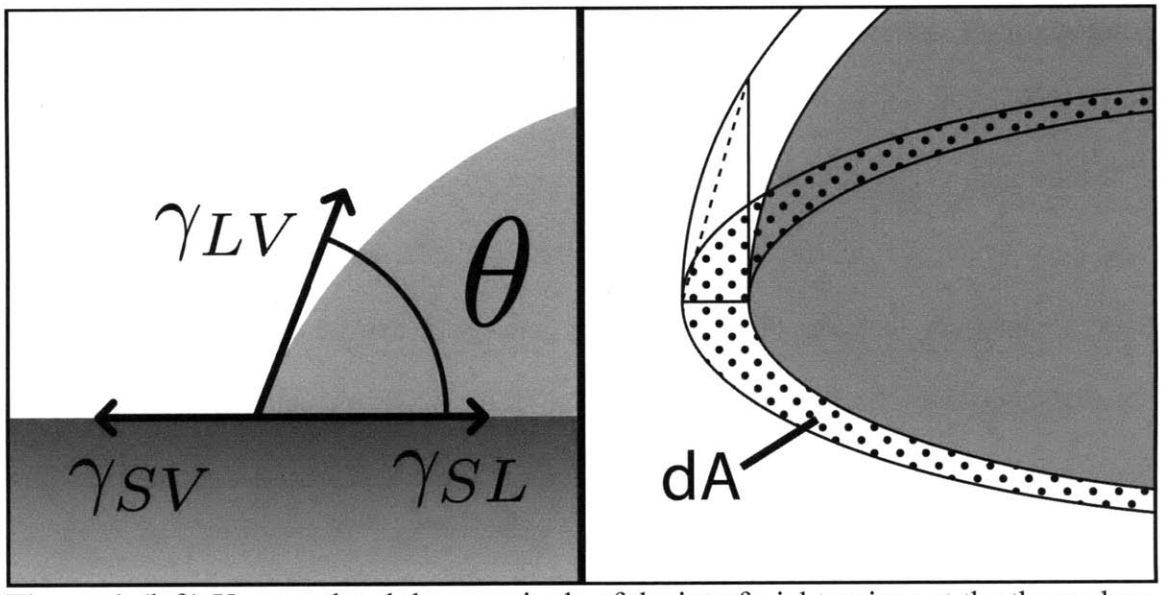

Figure 6. (left) Young related the magnitude of the interfacial tensions at the three-phase boundary of a sessile drop on a flat surface to the contact angle between the liquid-air and liquid-solid interfaces. (right) This equation must be employed judiciously as the liquid-solid interfacial tension calculated is only representative of the annular region immediately neighboring the drop's boundary. The differential area considered in the derivation is shaded.

In Young's original derivation, the equilibrium angle was calculated via force balance requirements at the 3-phase line. This derivation is briefly summarized in Fig. 6, and it yields the familiar equation:

$$\gamma_{sv} = \gamma_{sl} + \gamma_{lv}cos(\theta) \tag{1.16}$$

While the end result is the same, it is instructive to consider an alternate derivation of Young's equation[8,46] that is posed in terms of an energy balance. While volume is being added to the drop, the 3-phase line will advance requiring the advancement of two interfaces (solid/liquid and liquid/vapor) and the retraction of the solid/vapor interfaces. The relationship uniting the interfacial energies and their differential areas shown in Fig. 6 is given below:

$$\gamma_{sl}dA_{sl} + \gamma_{lv}dA_{lv} + \gamma_{sv}dA_{sv} = dE \tag{1.17}$$

The contact angle is measured at equilibrium, so the drop volume is taken to be constant. The differential areas can be simplified by realizing that the change in A_{sl} is opposite to the change in A_{sv}. Additionally, the differential area dA_{lv} can be geometrically related to dA_{sl} via the geometric relation:

$$dA_{lv} = dA_{sl}cos(\theta) \tag{1.18}$$

Upon substitution into the original equation, and requiring all derivatives of energy to be zero at equilibrium, we find the original Young's formula (Eq 1.16). While the end result is the same, the derivation reveals an important caveat of Young's formula. The contact angle measured does not reflect the interfacial energy of the entire wetted solid/liquid interface. Instead, it is only sensitive to the interfacial energy of an annular section local to the 3-phase line depicted in Fig. 6.

As described in Section 1.3, another important quantity that will be used to relay the measurements made in this thesis is the work of adhesion, W_{sl}. The expression for the work of adhesion is derived from the definition of interfacial energy (Eq. 1.19) with Young's equation (1.20), and is termed the Young-Dupré relation[8] (Eq. 1.21). In contrast to the version of Young's equation given above (Eq. 1.16), γ_s replaces γ_{sv} and γ_l replaces γ_{lv} in the version below (Eq. 1.20) due to the negligible influence of the gaseous phase on the interfacial energies of the liquid and solid.

$$\gamma_{sl} = \gamma_s + \gamma_l - W_{sl} \tag{1.19}$$
$$\gamma_s = \gamma_{sl} + \gamma_l cos(\theta) \tag{1.20}$$
$$W_{sl} = \gamma_l(1 + cos(\theta)) \tag{1.21}$$

In this thesis the work of adhesion will be the preferred means of expressing interfacial measurements. As shown previously, the work of adhesion is directly related to the interfacial energy and describes the strength of the interaction between the solid and liquid. Furthermore, it is experimentally attractive, as its calculation requires only measurement of the contact angle and the probe liquid's surface tension. An understanding of this expression will also simplify interpretation of the following discussions on the wetting of non-ideal surfaces.

1.7 Extending Young's Equation

The surfaces in the derivations previously described are assumed to be perfectly planar and perfectly homogenous. However, only very few surfaces of scientific and technological interest will have a roughness in which the flat approximation would suffice. To allow measurements on textured surfaces, it is necessary to adjust the previously derived formula to incorporate the effect of surface roughness.

The first and most commonly used correction for roughness was developed by Wenzel in 1936.[47] The roughness is characterized using a term *r*, the roughness factor, defined as the ratio of the area of the actual surface to the geometric or projected surface. Young's equation can be recalculated using this factor to yield:

$$r(\gamma_{sv} - \gamma_{sl}) = \gamma_{lv}cos(\theta) \tag{1.22}$$

The measured angle corresponds the macroscopic angle measured. It is straightforward to relate the macroscopic contact angle measured on a rough surface to the contact angle

that would be measured on ideally smooth surface of the same material. The observed contact angle is related to the ideal contact angle via the relation:

$$r * cos(\theta_{ideal}) = cos(\theta_{observed}) \tag{1.23}$$

From this it is clear to see the effect roughness has on the contact angle: for surfaces that have a contact angle less than 90°, increasing roughness reduces the contact angle, or increases wetting. For surfaces with contact angles greater than 90°, increasing roughness increases the contact angle.

It is important to understand the origin of the *r* factor. Roughness is often reported as the root mean square (RMS) of the deviation from a surface's average height, as measured using profilometry. Wenzel recognized this measure did not satisfactorily capture the effect on wetting and highlighted a study in which samples exhibited the same contact angle yet differed nearly two orders of magnitude in RMS roughness.[48] The effect of roughness is better captured from calculating the total area of the interface. Such a measurement was impossible when Wenzel's work was originally performed but is now achievable with scanning probe techniques.

Furthermore, Wenzel makes a salient point that the "type" of roughness is absolutely critical.[48] For demonstration, he considers a grooved surface that resembles a sawtooth curve. Every surface with this profile has the same *r*-factor: 1.41. However, the importance of the scale of the effects can be seen with a simple thought experiment. A surface that is otherwise smooth with the sawtooth profile of a period greater than the drop size would report a contact angle equivalent to the angle that would be measured on

an ideally flat surface. Furthermore, decreasing the period of the roughness below the size of the liquid molecules would produce a surface whose solvent accessible area is equivalent to a flat surface. Thus, at both extremes of the length scale, the roughness of the surface cannot be probed by the liquid.

Furthermore, the type of roughness has a significant effect on the local contact angle. Early attempts to understand contact angle hysteresis sought to link geometric variations experienced by the three-phase line while advancing and receding to the macroscopic angle measured. As hysteresis is observed with surfaces that can be practically considered perfectly flat, this model is only one plausible cause of hysteresis. Roughness can also influence the anisotropy of a surface's wetting behavior. Grooved[49,50] or striped[51] surfaces show that droplets do not present the same contact angle in both directions. Surfaces can be fabricated with strongly anisotopic surface patterning to control the motion and growth of a liquid in contact with the surface.[52] The roughness experienced by an expanding drop is proportional to the projected length of the local surface perpendicular to the contact line.

Wenzel's work was primarily motivated by a study of waterproofing materials, generally applied to flat surfaces. Cassie and Baxter, also studying waterproofing materials, sought to extend Wenzel's theory to porous surfaces, namely fabrics that had been treated with a water repellant coating.[53] Porous surfaces in contact with a drop of water do not present a simple interface between a solid and a liquid. Rather, the liquid forms a mixed interface: a solid/liquid interface is formed where the drop contacts the surface, but a liquid/vapor

interface exists in the pores or voids in between fibers. If f_1 is defined as the surface fraction of the solid/liquid interface and f_2 is defined as the surface fraction of the liquid/vapor interface, with $f_1+f_2 = 1$, the solid interface's contribution to Young's equation can be treated as the weighted average of its components. Writing the energy to advance the solid/liquid interface a unit area in terms of f_1 and f_2, we find:

$$E_{adv} = f_1(\gamma_{sv} - \gamma_{sv}) + f_2\gamma_{lv} \tag{1.24}$$

The first term, is a product of the solid/liquid interface fraction f_1 and the interfacial energy difference of the interface being formed between the liquid and solid, and the interface being destroyed between the solid and vapor. The second product reflects the energy required to extend the liquid over the pores, creating a liquid/vapor interface.

For a flat surface, Young's equation can be rearranged to give an expression for E_{adv}:

$$\gamma_{sv} - \gamma sl = \gamma_{lv} cos(\theta_{observed}) = E_{adv} \tag{1.25}$$

By equating the two equations, an expression for the macroscopically measurable contact angle can be found:

$$\gamma_{lv} cos(\theta_{observed}) = f_1(\gamma_{sl} - \gamma_{sv}) + f_2\gamma_{lv} \tag{1.26}$$

Just as with Wenzel's formula, it was possible to translate the observed angle to the angle that would be measured on a perfectly smooth surface, it is possible to relate the material's contact angle to the measured angle:

$$cos(\theta_{ideal}) = \frac{\gamma_{sv} - \gamma_{sl}}{\gamma_{lv}} \tag{1.27}$$

$$cos(\theta_{observed}) = f_1 cos(\theta_{ideal}) - f_2 \tag{1.28}$$

If f_2, the fraction of the interface composed of the interface spanning pores, were zero, the previous equation reduces to Wenzel's formula, with f_1 replacing r. The Cassie-Baxter relation is used to understand the wetting observed on superhydrophobic surfaces.[54-56] These surfaces, which both exist naturally and are engineered, demonstrate contact angles with water exceeding 150°. The characteristics in common with all of these surfaces are a high degree of roughness and a surface that is intrinsically non-wetting. The non-wetting surface prevents the liquid from being drawn into the surface via capillary action, and the extreme roughness only permits a fraction of the droplet to contact the solid. As the fraction of the interface that is liquid/vapor increases, the observed angle approaches 180°, independent of the material's intrinsic wettability. Because of this property, the production and design of such surfaces is a technological goal.

While the Cassie-Baxter expression was developed to described rough surfaces that could trap air, it can be used more generally as an expression of interfacial energy for a heterogeneous surface. This treatment has been successfully applied to systems that possess heterogeneous surfaces containing domains of different chemical composition and wetting behavior.[51,57-60] There have been extensions made to this model to further increase its accuracy by accommodating for the geometry of the surface[51,57]; however, these extensions are not generalizable and are system dependent. For this reason, the standard Cassie-Baxter equation will be treated as the benchmark model for expressing interfacial energy.

1.8 Experimental Determination of Interfacial Energy

Contact angle remains the most common and most accessible method of measuring the interfacial energy of a solid/liquid interface. This technique has been described in the preceding section and remains straightforward to perform. It must be noted that the measurements obtained are only valid if certain conditions are met. Only drops that are clearly advancing or receding and are not affected by surface imperfections (Section 1.9.) are admissible.

Tensiometry is a mechanical technique for measuring interfacial tension. This technique directly measures the force exerted on an interface; by lowering and raising a specimen in and out of a liquid, interfacial area is created and destroyed, respectively. By canceling the buoyant force exerted by the liquid on the object, the force due to interfacial tension can be accurately measured.[61] The specimen must be smooth and possess a constant perimeter along the immersion direction as the interfacial tension is directly calculated by dividing the force measured by the sample's perimeter. Tensiometry can also be used to directly measure the surface energy of a liquid: using a perfectly wetting calibration standard, the resulting interfacial tension will exactly represent the surface tension of the liquid being measured. Two standard probes exist for conducting this measurement: the Wilhelmy plate and the DeNuoy ring, which are functionally equivalent but with different geometries.

Tensiometry is an attractive method of measuring interfacial tension because it easily allows measurement of advancing and receding angles. While the primary limitation in measuring contact angle hysteresis in sessile drop technique is ensuring the drop

perimeter is evenly advancing and receding, this is automatically accounted for by the geometry of the interface under study in tensiometry. Furthermore, tensiometry is capable of measuring highly wetting surfaces that exhibit low contact angles that are difficult to measure using goniometry.

The final technique to measure interfacial energy was recently developed by a collaborator and myself. This technique utilizes scanning probe microscopy to generate a mapping of interfacial energy over a nanoscale region, and it relies on measuring the energy dissipated while imaging a liquid/solid interface. Details of this method will be given in the following chapter. This technique is especially useful as it establishes the interfacial energy away from the three-phase contact line and ensures the region measured is free of defects.

1.9 Measurement Difficulties: Hysteresis and Pinning

The measurement techniques discussed so far have presented the measurement of contact angle as a straightforward method that produces certain results. However, much care must be spent in the acquisition and interpretation of the data gathered as large errors can occur due to the unique challenges of measuring contact angle. While contact angle so far has been presented as a geometric feature resulting from the underlying physical interactions at the interface, its value for a given liquid-solid interface is not unique. Most surfaces can actually report a large range of values depending on the last motion of the three phase line, and this dependence on the history and current motion of the contact line is referred to as contact angle hysteresis (CAH). The advancing and receding angles represent the extreme points of this range of values. To ensure reliable measurements,

one requirement is that the direction of motion be confirmed. That is, to report contact angle values of a drop that is clearly advancing as advancing (and likewise for receding) and not simply the angle observed of a sessile drop on the surface.

One cause of CAH is the presence of defects on the surface being measured. Even surfaces that are close to perfectly flat can contain small imperfections, either hills or holes in the surface. These imperfections can pin the three-phase line preventing from evenly advancing (or receding) over the surface. Because such defects prevent a barrier to a spreading drop, they will cause the apparent contact angle to be greater than what it would be for an ideally flat surface. For a receding drop, the three phase line may be pinned at the defect and cause the contact angle to appear lower than what it ideally would be if the surface were smooth.

Pinning defects have been studied in great detail because they represent a problem in performing and interpreting measurements as well as a challenge in the design of microfluidic systems.[62] The geometry, relative stability, and movement of drops on superhydrophobic surfaces is dominated by pinning at the numerous projections from the surface.[63] Pinning defects however also present a means of engineering surfaces that present anisotropic wetting properties. By fabricating surfaces with oriented grooves or raised plateaus, the contact angle becomes dependent on direction, and such surfaces are of interest for directing the motion of liquids on surfaces.[64]

With regards to characterizing surfaces of unknown surface energy, it is ideal to reduce the probability of pinning. This is done by producing surfaces with few intrinsic defects and by exercising caution to not damage the surface prior to and during measurements.

Furthermore, while measuring the contact angle on such surfaces, one must remain vigilant that the drop grows evenly and smoothly, as pinning would result in anisotropic spreading and an asymmetric shape. Additionally, the drop must grow evenly around the edges, as a translational motion would indicate the drop is pinned at one edge with additional growth pushing the center of the drop further from the pinned edge.

In additional to roughness-related defects, chemical heterogeneity can also induce pinning defects. For example, the motion of a drop on a hydrophilic patch on a hydrophobic surface will remain constant until the drop edge contacts the hydrophobic background. At this point the drop will become pinned and not grow in width until the advancing contact angle of the hydrophilic surface is reached.[65,66]

Numerous treatments for contact angle hysteresis have been proposed. One approach is dependent on the density of defects on the surface. Surfaces prepared with a variable concentration of defects generated via ion bombardment have shown the presence of even a limited number of defects can have an appreciable affect on the contact angle measured. As the number of defects increases, the surface roughness increases and approaches the treatment given by Wenzel.[67]

Another approach to understanding contact angle hysteresis which is more germane to smooth but chemically heterogeneous surfaces considers the effect of the surface morphology or patterning on the shape of the three phase line.[57] By pinning three phase line at certain points and forcing it to conform to chemically patterned domains, the tortuosity of the three phase line is increased and is lengthened beyond what would be calculated for a simple spherical cap, as is assumed by Young's equation. The length of

the drop and three phase region would need to be increased and would follow a formulation similar to Wenzel's treatment of roughness.

Finally, even smooth and chemically homogenous surfaces can exhibit contact angle hysteresis as well. While the reasons of hysteresis were historically assumed to be related to surface roughness or defects, experiments performed on flat molecular monolayers demonstrated a reproducible CAH.[68-72] Hysteresis in this case is assumed to be due to adsorption of the probe liquid to the interface, affecting the contact angle and causing history dependent behavior for the measured angle. Indeed, humidity related effects on contact angle have been observed demonstrating water adsorbed to the solid-air interface can affect the contact angle.[73]

While there exist many treatments to describe contact angle hysteresis, no consensus exists to quantitatively analyze the mechanisms responsible. As the focus of this thesis is the determination of the interfacial energy of chemically heterogeneous systems, contact angle hysteresis will not be fully considered. Problems that affect the validity of the advancing angle measurement, however, will be considered: namely surface roughness and the presence of defects capable of pinning the three-phase line. This will be accomplished by producing surfaces that approach ideal smoothness, exhibit complete coverage, have a limited number of pinning defects, and ensuring the measurements represent non-pinned droplets.

Besides CAH, other complications for experimental validity exist. The solid surface is assumed to be perfectly rigid, but this is not always the case. The forces acting at the perimeter of the drop can induce deformations in the underlying substrate. The tiny

deformations at the edge would lead to a contact angle measurement that is different from the actual angle formed by the liquid-vapor interface and the now deformed solid-liquid interface. Such deformations have been observed to be time dependent, consistent with time dependent mechanical behavior observed in the deformation or rearrangement of solids.[74]

Finally, many interesting interfaces exist that are not stable to permit traditional contact angle measurements. One pertinent example would be the measurement of protein films. Films of proteins can be cast from solution and allowed to dry. As the proteins remain soluble in the probe liquid, water, measurement of the resulting contact angle would need to be performed rapidly to limit the amount of protein that would be dissolved into the probe liquid. Such measurements are of questionable validity as ideally the contact angle represents a thermodynamically stable value.

1.10 Conclusion

Interfacial energy reflects the strength of solvent-surface forces at the interface. The imbalance of forces at the interface redistributes the local solvent, and this difference in density produces the interfacial tension. This tension can be measured experimentally; additionally and more commonly, interfacial energies can be deduced from drop shape analysis. The numerous interactions between the liquid and solid must be accounted for individually to accurately predict interfacial energy.

From the list of complications of contact angle measurement, the requirements for an ideal substrate for measurements is found. Rigid substrates are preferable as they limit

deformation. Surface roughness should be minimized to prevent pinning, and the surface should be as uniform as possible. Additionally, only surfaces that remain stable during measurement will be studied.

1.11 References

(1) Munson, B. R.; Young, D. F.; Okiishi, T. H. *Fundamentals of Fluid Mechanics*; Fifth ed.; John Wiley & Sons, Inc., 2005.

(2) Callister, W. D.; Rethwisch, D. G. *Materials Science and Engineering: An Introduction*; Seventh ed.; John Wiley & Sons, 2007.

(3) Balluffi, R. W.; Allen, S. M.; Carter, W. C. *Kinetics of Materials*; First ed.; Wiley-Interscience, 2005.

(4) Burton, W. K.; Cabrera, N. *Discussions of the Faraday Society* **1949**, 33-39.

(5) Walheim, S.; Boltau, M.; Mlynek, J.; Krausch, G.; Steiner, U. *Macromolecules* **1997**, *30*, 4995-5003.

(6) Dill, K. A.; Bromberg, S.; Yue, K.; Chan, H. S.; Ftebig, K. M.; Yee, D. P.; Thomas, P. D. *Protein Science* **1995**, *4*, 561-602.

(7) Acharya, H.; Vembanur, S.; Jamadagni, S. N.; Garde, S. *Faraday Discuss.* **2010**, *146*, 353-365.

(8) Israelachvili, J. *Intermolecular and Surfaces Forces: Second Edition*; Second ed.; Academic Press: Boston, 2000.

(9) Hiemenz, P. C.; Rajagopalan, R. *Principles of Colloid and Surface Chemistry*; Third ed.; Marcel Dekker, Inc.: New York, 1997.

(10) Myers, D. *Surfactant Science and Technology*; Third ed.; Wiley-Interscience: Hoboken, 2006.

(11) Eastoe, J.; Dalton, J. S. *Advances in Colloid and Interface Science* **2000**, *85*, 103-144.

(12) Funasaki, N.; Hada, S. *The Journal of Physical Chemistry* **1979**, *83*, 2471-2475.

(13) Ljunggren, S.; Eriksson, J. C.; Kralchevsky, P. A. *Journal of Colloid and Interface Science* **1997**, *191*, 424-441.

(14) Menger, F. M.; Littau, C. A. *Journal of the American Chemical Society* **1993**, *115*, 10083-10090.

(15) Hooper, J. B.; Schweizer, K. S. *Macromolecules* **2006**, *39*, 5133-5142.

(16) Farrell, R. A.; Petkov, N.; Morris, M. A.; Holmes, J. D. *Journal of Colloid and Interface Science* **2010**, *349*, 449-472.

(17) Matsen, M. W.; Bates, F. S. *Macromolecules* **1996**, *29*, 7641-7644.

(18) Klok, H. A.; Lecommandoux, S. *Adv. Mater.* **2001**, *13*, 1217-1229.

(19) Lin, Y.; Boker, A.; He, J. B.; Sill, K.; Xiang, H. Q.; Abetz, C.; Li, X. F.; Wang, J.; Emrick, T.; Long, S.; Wang, Q.; Balazs, A.; Russell, T. P. *Nature* **2005**, *434*, 55-59.

(20) Ikai, A.; Tanford, C. *Nature* **1971**, *230*, 100-102.

(21) Tanford, C. *Science* **1978**, *200*, 1012-1018.
(22) Dill, K. A. *Biochemistry* **1990**, *29*, 7133-7155.
(23) Tanford, C. *Journal of the American Chemical Society* **1962**, *84*, 4240-4247.
(24) Kyte, J.; Doolittle, R. F. *J. Mol. Biol.* **1982**, *157*, 105-132.
(25) Black, S. D.; Mould, D. R. *Anal. Biochem.* **1991**, *193*, 72-82.
(26) Cornette, J. L.; Cease, K. B.; Margalit, H.; Spouge, J. L.; Berzofsky, J. A.; Delisi, C. *J. Mol. Biol.* **1987**, *195*, 659-685.
(27) Strong, M.; Sawaya, M. R.; Wang, S. S.; Phillips, M.; Cascio, D.; Eisenberg, D. *Proc. Natl. Acad. Sci. U. S. A.* **2006**, *103*, 8060-8065.
(28) Murnen, H. K.; Rosales, A. M.; Jaworsk, J. N.; Segalman, R. A.; Zuckermann, R. N. *Journal of the American Chemical Society*, *132*, 16112-16119.
(29) Willard, A. P.; Chandler, D. *The Journal of Physical Chemistry B* **2010**, *114*, 1954-1958.
(30) Kirkwood, J. G.; Buff, F. P. *The Journal of Chemical Physics* **1949**, *17*, 338-343.
(31) Tolman, R. C. *The Journal of Chemical Physics* **1948**, *16*, 758-774.
(32) Gibbs, J. W. *Scientific Papers of J. Willard Gibbs*; Longmans, Green, and Co.: New York, 1906; Vol. 1.
(33) Fowler, R. H. *Proceedings of the Royal Society of London. Series A, Mathematical and Physical Sciences* **1937**, *159*, 229-246.
(34) Widom, B.; Rowlinson, J. S. *Molecular Theory of Capillarity*; Dover Publications, 2003.
(35) Fowkes, F. M. *The Journal of Physical Chemistry* **1963**, *67*, 2538-2541.
(36) Girifalco, L. A.; Good, R. J. *The Journal of Physical Chemistry* **1957**, *61*, 904-909.
(37) Harkins, W. D. *The Journal of Chemical Physics* **1941**, *9*, 552-568.
(38) Zisman W, A. In *Contact Angle, Wettability, and Adhesion*; American Chemical Society: Washington, D.C., 1964, p 1-51.
(39) Owens, D. K.; Wendt, R. C. *Journal of Applied Polymer Science* **1969**, *13*, 1741-1747.
(40) Van Oss, C. J.; Chaudhury, M. K.; Good, R. J. *Chemical Reviews* **1988**, *88*, 927-941.
(41) Van Oss, C. J.; Good, R. J.; Chaudhury, M. K. *Langmuir* **1988**, *4*, 884-891.
(42) Good, R. J.; Girifalco, L. A. *The Journal of Physical Chemistry* **1960**, *64*, 561-565.
(43) Kwok, D. Y.; Neumann, A. W. *Advances in Colloid and Interface Science* **1999**, *81*, 167-249.
(44) Kwok, D. Y.; Gietzelt, T.; Grundke, K.; Jacobasch, H. J.; Neumann, A. W. *Langmuir* **1997**, *13*, 2880-2894.
(45) Young, T. *Philosophical Transactions of the Royal Society of London* **1805**, *95*, 65-87.
(46) Good, R. J. *Journal of the American Chemical Society* **1952**, *74*, 5041-5042.
(47) Wenzel, R. N. *Industrial & Engineering Chemistry* **1936**, *28*, 988-994.

(48) Wenzel, R. N. *Journal of Physical and Colloid Chemistry* **1949**, *53*, 1466-1467.
(49) Seemann, R.; Brinkmann, M.; Kramer, E. J.; Lange, F. F.; Lipowsky, R. *Proc. Natl. Acad. Sci. U. S. A.* **2005**, *102*, 1848-1852.
(50) Biben, T.; Joly, L. *Physical Review Letters* **2008**, *100*, 186103.
(51) Drelich, J.; Wilbur, J. L.; Miller, J. D.; Whitesides, G. M. *Langmuir* **1996**, *12*, 1913-1922.
(52) Jokinen, V.; Leinikka, M.; Franssila, S. *Adv. Mater.* **2009**, *21*, 4835-4838.
(53) Cassie, A. B. D.; Baxter, S. *Trans. Faraday Soc.* **1944**, *40*, 0546-0550.
(54) Patankar, N. A. *Langmuir*, *26*, 7498-7503.
(55) Forsberg, P. S. H.; Priest, C.; Brinkmann, M.; Sedev, R.; Ralston, J. *Langmuir* **2009**, *26*, 860-865.
(56) Spori, D. M.; Drobek, T.; Zü rcher, S.; Ochsner, M.; Sprecher, C.; Mü hlebach, A.; Spencer, N. D. *Langmuir* **2008**, *24*, 5411-5417.
(57) Woodward, J. T.; Gwin, H.; Schwartz, D. K. *Langmuir* **2000**, *16*, 2957-2961.
(58) Woodward, J. T.; Schwartz, D. K. *Langmuir* **1997**, *13*, 6873-6876.
(59) Woodward, J. T.; Ulman, A.; Schwartz, D. K. *Langmuir* **1996**, *12*, 3626-3629.
(60) Bierbaum, K.; Grunze, M.; Baski, A. A.; Chi, L. F.; Schrepp, W.; Fuchs, H. *Langmuir* **1995**, *11*, 2143-2150.
(61) Javadi, A.; Mucic, N.; Vollhardt, D.; Fainerman, V. B.; Miller, R. *Journal of Colloid and Interface Science*, *351*, 537-541.
(62) Mognetti, B. M.; Yeomans, J. M. *Phys Rev E Stat Nonlin Soft Matter Phys* **2009**, *80*, 056309.
(63) Chatain, D.; Lewis, D.; Baland, J.-P.; Carter, W. C. *Langmuir* **2006**, *22*, 4237-4243.
(64) Malvadkar, N. A.; Hancock, M. J.; Sekeroglu, K.; Dressick, W. J.; Demirel, M. C. *Nat. Mater.*, *9*, 1023-1028.
(65) Gao, L.; McCarthy, T. J. *Langmuir* **2007**, *23*, 3762-3765.
(66) Gao, L.; McCarthy, T. J. *Langmuir* **2009**, *25*, 14105-14115.
(67) Ramos, S. M. M.; Charlaix, E.; Benyagoub, A. *Surf. Sci.* **2003**, *540*, 355-362.
(68) Folkers, J. P.; Laibinis, P. E.; Whitesides, G. M. *J. Adhes. Sci. Technol.* **1992**, *6*, 1397-1410.
(69) Laibinis, P. E.; Bain, C. D.; Nuzzo, R. G.; Whitesides, G. M. *The Journal of Physical Chemistry* **1995**, *99*, 7663-7676.
(70) Laibinis, P. E.; Fox, M. A.; Folkers, J. P.; Whitesides, G. M. *Langmuir* **1991**, *7*, 3167-3173.
(71) Laibinis, P. E.; Whitesides, G. M. *Journal of the American Chemical Society* **1992**, *114*, 1990-1995.
(72) Laibinis, P. E.; Whitesides, G. M.; Allara, D. L.; Tao, Y. T.; Parikh, A. N.; Nuzzo, R. G. *Journal of the American Chemical Society* **1991**, *113*, 7152-7167.
(73) Hu, H.; Larson, R. G. *Journal of Physical Chemistry B* **2002**, *106*, 1334-1344.
(74) Evans, S. D.; Sharma, R.; Ulman, A. *Langmuir* **1991**, *7*, 156-161.

Chapter 2: The Interfacial Energy of Patchy Surfaces

The previous chapter introduced the concept of interfacial energy, discussed its origins and outlined a few generalized models used to describe the interfacial energy of various systems. This chapter will focus solely on the interfacial energy of patchy surfaces in contact with liquid. Patchy surfaces, as the name suggests, are comprised of chemically homogeneous domains or patches. In general, patchy surfaces lack the extreme roughness required for super-hydrophobic Cassie-Baxter wetting, but can exhibit moderate roughness. Domains can range in size from molecular- to micron-scale depending on the process used to produce them. The chapter will conclude with the statement of research of this thesis.

2.1 Interpretation of Contact Angle and the Three-Phase Line

The contact angle measurement discussed in the previous chapter remains the primary method of quantifying interfacial energy. As highlighted in Section 1.6, the primary caveat for interpreting the contact angle is to recognize that it represents the interfacial energy of the solid in the annular area, the three-phase region, near the drop perimeter. For homogeneous, flat surfaces, the value of interfacial energy derived from contact angle is clearly that of the solid liquid interface. However, surfaces that contain patches with dissimilar surface properties will require a more complex interpretation.

The primary concern when using contact angle to measure the interfacial energy of patchy surfaces is the location of the three-phase line. For a surface with large patches, a drop may lie entirely within one patch, or it may encompass several patches but its three-phase line only contacts one material. This scenario is graphically represented in

Fig. 1A, where the red and yellow regions reflect hydrophilic and –phobic patches, respectively. Here, the contact angle reflects that the surface is wetting when a portion of the contact area is hydrophobic.

In another instance, a drop may be pinned at the boundary of a patch. This instance is shown in Fig 1B. In this case, increasing the volume of the drop will result in the contact angle increasing from the contact angle of the interior patch to the contact angle of the outer patch. A range of possible contact angles is possible, and only one angle represents the average interfacial energy of the surface. Experiments using lithographically patterned surfaces demonstrate that the contact line location is of utmost importance[1-4] and that the surface fraction terms of the Cassie-Baxter relation must be interpreted in terms of the contact line rather than the entire solid-liquid contact area.

The situation becomes more complicated when the patch size is significantly smaller than the drop size. Depending on the system under study, the shape of the contact line may be perturbed by the patches. Ideally, the contact line will accurately sample all patches on the surface in their representative proportions, as demonstrated by the lower arc in Fig. 1C. It is possible that the contact line will be partially pinned at non-wetting patches, resulting in a convoluted line that spans the wetting region and is pinned at the boundaries of the non-wetting patches, as demonstrated by the upper arc in Fig. 1C. This contact line will be longer than estimated by the drop shape and will not sample the patches proportionally. Several attempts have been made to incorporate contact line

geometry in the interpretation of interfacial energy, but these attempts are tied to specific surface geometries and are not easily generalizable.[5,6]

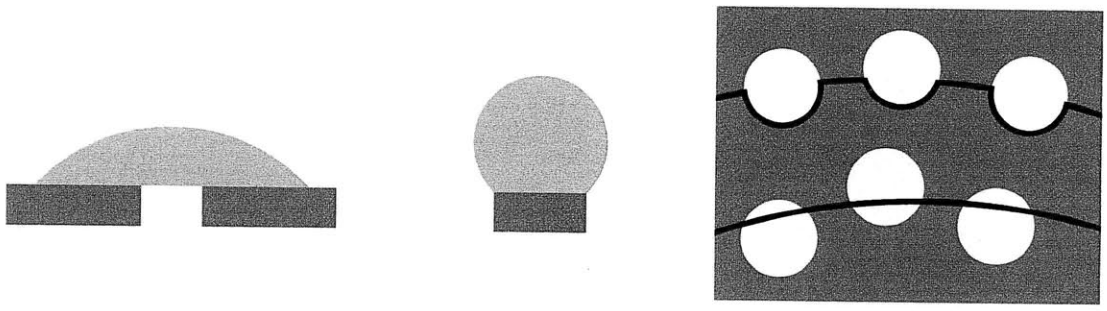

Figure 1. Three examples of the complications that arise from using contact angle techniques to measure the interfacial energy of patchy surfaces. (a) A drop significantly larger than the hydrophobic patch (yellow) will only reflect the interfacial energy of the hydrophilic matrix (red). (b) Conversely, a drop on a hydrophilic patch will represent only the interfacial energy of the hydrophilic patch until the drop encounters the boundary with a hydrophobic matrix. At this point, the drop boundary will be pinned and the contact angle will increase until equal to that of the hydrophobic matrix. At this point the contact line will continue to advance. (c) In the case of smaller patches, a drop's contact line will ideally accurately sample all patches on the surface (lower arc). This assumption underlies the Cassie-Baxter relation. In some cases, however, the contact line will become pinned at the hydrophobic patches, resulting in a convoluted shape (upper arc).

Even in the case where the contact line intercepts patches to yield a compositionally accurate sample of the surface, the nature of the solid-liquid interface complicates the interpretation of the contact angle. The structure of the interfacial liquid must transition between patches, and this transition occurs over a finite distance. For a bi-component surface, this transition length creates a third patch type corresponding to the boundary region. The relationship between the surface fraction that is comprised of this boundary region is system-dependent, but the boundary region fraction clearly increases for intermediate compositions, where its presence causes the greatest deviance from the prediction Cassie-Baxter trend.

Measurements of the trend in interfacial energy with respect to composition can yield an estimate for the boundary region width, and thus the transition length, given the surface morphology can be measured. Deviations from the linear Cassie-Baxter trend were observed for a partial monolayer formed on a gold surface.[7] These surfaces resembled Fig. 1C, where the partial monolayer comprised non-wetting patches on the more wetting gold substrate. The Cassie-Baxter expression was modified to include a third term corresponding to the boundary region at the edges of the monolayer patches and its interfacial energy was estimated to be the same as the partial monolayer. Calculating the average boundary length per unit area from AFM images, the boundary width was found to be approximately 5 nm, a length consistent with the size of the adsorbed molecule.

2.2 Self-Assembled Monolayers as Model Patchy Surfaces

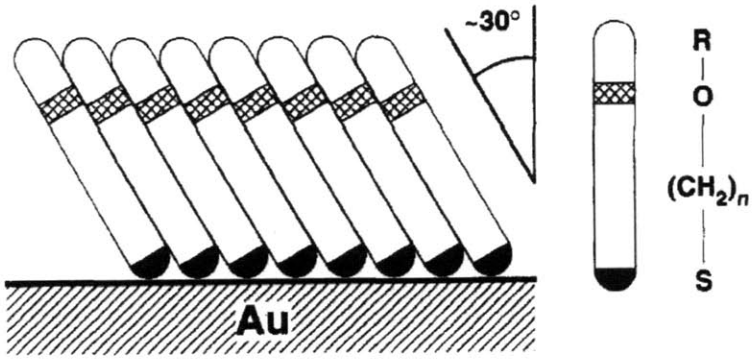

Figure 2. Self-assembled monolayers form dense two dimensionally ordered arrays on gold surfaces. Individual thiol molecules (right) adsorb at an angle to the gold surface via gold-thiol bonds. Only the headgroups (labeled R) are solvent accessible. Taken without permission.[8]

Self-assembled monolayers (SAMs) are a versatile tool used to study wetting behavior of surfaces with various chemical groups exposed, and provide a straightforward route to produce patchy surfaces. Their structure, history, and preparation are described further in Chapter 3. Briefly, SAMs are two-dimensional arrays of molecules adsorbed to a solid

surface. They form dense structures with nearly complete coverage commensurate to the underlying crystal lattice and are relatively stable at ambient conditions. The most common system of SAMs is alkylthiols on gold. Alkylthiols are linear molecules with a thiol terminal group at one end that bonds to the gold surface. The other end is exposed and can be any functional group. In addition to be able to select the exposed functional group, SAMs form from alkylthiols of a large range of lengths, offering another parameter that can be varied.

The wetting behavior of SAMs has been extensively studied by Whitesides.[8-21] SAMs with identical terminal groups but varying lengths were prepared on gold, as well as silver and copper. The contact angle of water on these SAMs remains constant after the thiol length exceeds 8 methylene units.[19] As longer thiols form more stable and denser monolayers with greater coverage, this result shows that the wetting behavior is sensitive to the exposed chemical group and not the thiol length.

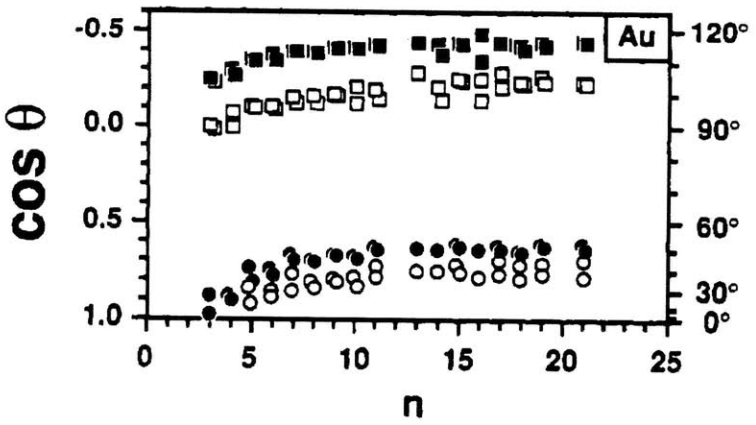

Figure 3. The contact angle becomes invariant when the thiols used to form SAMs exceed a certain length. The contact angle of water (squares) and hexadecane (circles) on SAMs is plotted against the number of methylene units in the alkylthiol. Advancing (filled) and receding (open) values for the contact angle remain constant for SAMs composed of thiols containg eight or more carbon atoms. Taken without permission.[19]

Patchy SAMs can be easily generated by using a solution of two or more thiols when forming the SAM. Monolayers composed of dissimilar thiols tend to phase-separate. The resulting monolayer will contain homogeneous patches composed of each thiol, and the size of each domain will be tens of nanometers or larger. The models for non-homogeneous interfaces discussed in the previous chapter can be verified by measuring two component SAMs formed from thiols with dissimilar wetting properties. In one study by Whitesides[18], SAMs were formed from thiols terminated with either hydrophobic methyl groups or hydrophilic alcohol groups. When the thiol lengths were similar, the wetting varied as predicted by the Cassie-Baxter relation: increasing the hydrophilic fraction of the surface made the surface increasingly wetting.

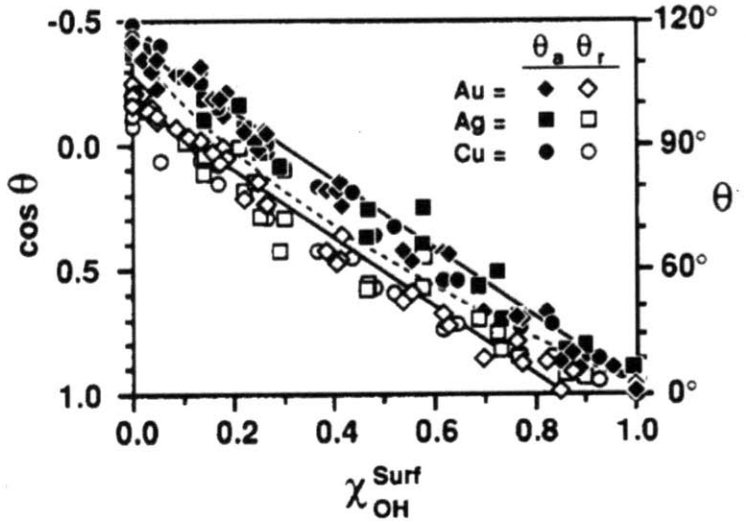

Figure 4. Patchy surfaces were produced by forming mixed SAMs of methyl and alcohol terminated alkylthiols. The resulting linear trend with respect to surface composition confirms the validity of the Cassie-Baxter relation.[18] The contact angle and its cosine are given for SAMs formed on gold, silver and copper substrates.

One interesting exception from this trend was observed in a series of SAMs where the hydrophilic thiol was significantly longer than the hydrophobic thiol.[12] In this series, a peak was observed in the wettability at an intermediate composition. This unexpected

trend was attributed to the increased disorder of the protruding hydrophilic tails separated by interposed hydrophobic thiols. While increasing the hydrophobic content of the surface reduces the number of hydrophilic groups present on the surface, it increases the flexibility of the groups capable of interacting with the solvent. Due to the extra 'fluidity' of the surface, the surface hydrophilicity would actually increase at intermediate compositions.

2.3 Molecular Scale Patchiness

So far, surfaces prepared with a patch size of several nanometers or more have been discussed. Patchy surfaces for which the patch or domain size is molecular scale are actually far more common in naturally occurring biological surfaces. Understanding the interfacial energy of such surfaces is experimentally challenging because it is difficult if not impossible to adapt classical measurement techniques (*e.g.* contact angle measurements) to these systems. For this reason, such surfaces are primarily studied computationally. However, using these computational techniques, traditional, experimentally accessible values such as interfacial energy and contact angle are difficult to extract.

One study on the wetting and dewetting of patchy parallel plates sheds insight on how molecular-scale patchy surfaces interact with liquids.[22] Two hydrophobic plates, each 3.2 nm square, separated by 0.6 nm were shown to cause dewetting, or the depletion of water, between the plates. By adding only three hydrophilic hydroxyl groups to each plate, a stable film of water was found to persist between the plates (Fig. 5). Reducing the number of hydrophilic groups or reducing the pressure would induce dewetting, leading

to only transient films of water forming between the plates for very short durations. This study demonstrates how sensitive the wetting/dewetting transition can be for molecular-scale systems. A similar analysis was carried out by the same group analyzing the stability of a protein dimer. Melittin is a natural, plate-shaped protein with a flat hydrophobic surface. Hydrophobic interactions induce assembly of melittin into dimers, but it was observed a small mutation in the protein adding a hydrophilic group to the center of the hydrophobic patch would impede dewetting and thus dimerization.[23]

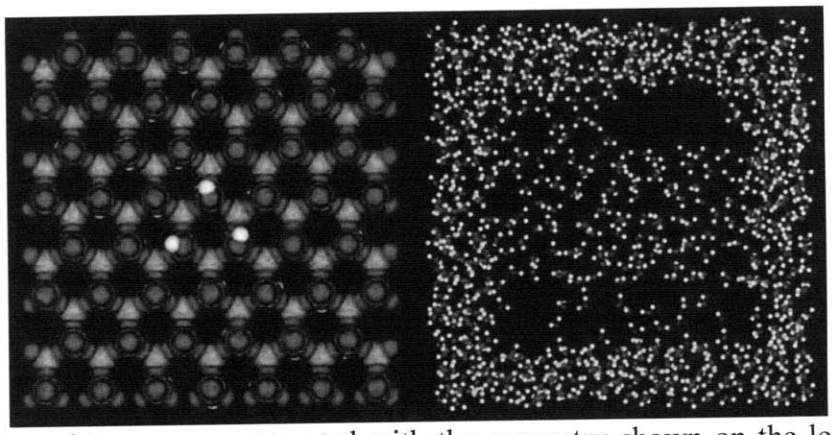

Figure 5. Two plates were constructed with the geometry shown on the left. The plate width is 3.2 nm. The plate is hydrophobic with the exception of the three hydroxyl groups in the center. The right image is snapshot of the water film between the plates, demonstrating that the few hydroxyl groups can stabilize a sheet of water between the hydrophobic plates.

The previous studies demonstrate that wetting is a collective phenomenon, and that it is difficult to separate wetting behavior patch-by-patch. A growing consensus is emerging that the entire surface must be considered since neighboring regions can significantly influence wetting. This is clearly demonstrated in a recent publication reanalyzing the hydropathy of a protein. Using the probability of cavity formation as a new metric of surface hydrophobicity, a new interpretation of protein hydropathy emerges. These patchy surfaces were once interpreted as having domains that were either highly

hydrophobic or hydrophilic, but it is now seen (Fig. 6) that these domains are moderately hydrophilic.[24]

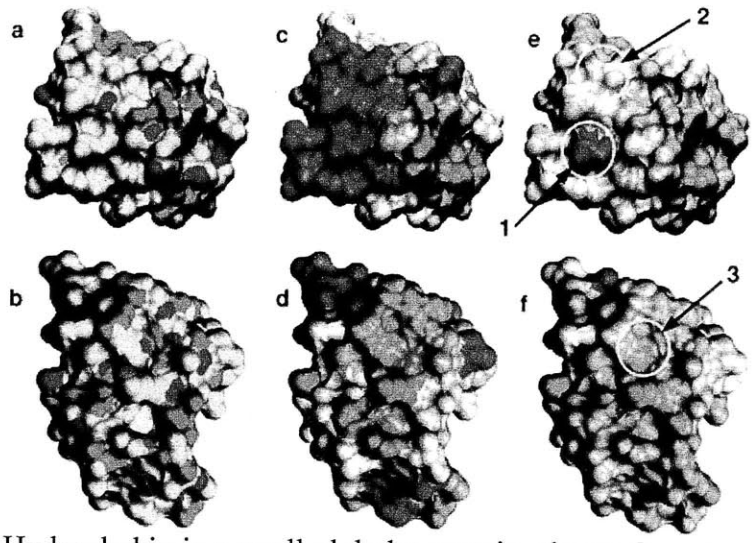

Figure 6. (a,b) Hydrophobin is a small globular protein, shown from two angles. Carbon is colored cyan, nitrogen red, oxygen blue, and sulfur yellow. (c,d) The surface of hydrophobin colored using the hydropathy scales developed by Kyte and Dolittle.[25] Red corresponds to hydrophilic, blue to hydrophobic and white to intermediate hydrophilicity. (e,f) The surface of hydrophobin is plotted using cavitation frequency as the metric for surface hydrophilicty, with red and blue corresponding to hydrophilic and hydrophobic regions as in (c,d). It is notable that the large hydrophobic region seen in (c) is more hydrophilic than would be expected, and that the entire protein surface is relatively hydrophilic despite the presence of many hydrophobic patches.[24]

2.4 Statement of Research

The original motive for the Cassie-Baxter expression was to describe wetting behavior on textiles, surfaces where the domains are significantly larger than the cases discussed in this chapter and where roughness is non-negligible. Regardless, the expression has been found valid for a large number of surfaces. When using contact angle measurements to probe interfacial energy, as long as the three phase line contacts a representative region of the surface and is not pinned, the derived interfacial energy can be taken as accurate for the entire surface.

Self-assembled monolayers are a particularly useful tool for probing the validity of the Cassie-Baxter relation. They are exceptionally smooth and can be fabricated with great control over the number and type of functional groups presented on the surface. Using these model patchy surfaces, the Cassie-Baxter relation was found to be the most accurate descriptor of the surfaces' interfacial energy. However, in certain cases, small adjustments to this trend were necessary, namely when additional disorder was present due to the flexibility of the molecules used to produce the monolayer. This disorder was evident either at the boundary of monolayer patches or when molecules of different length were used to form a mixed monolayer.

More recent results in computational modeling of patchy surfaces show the case for interpreting patchy surfaces is even more complex when the domains are molecular-scale. At this size scale, local wetting becomes a collective process and becomes sensitive to the composition of neighboring regions. Adding a small number of hydrophilic groups to a hydrophobic patch greatly increases the wettability of the entire region. In the case of protein surfaces, which are a complex patchwork of hydrophobic and hydrophilic regions, local variations were attenuated and the overall interfacial energy was intermediately wetting.

These recent results prove that the wetting of patchy surfaces is not always as straightforward as applying the Cassie-Baxter relation. While this relation may generally hold for surfaces where the domains span several nanometers or more, it appears to lose

validity when the patches grow too small. The apparent breakdown of the Cassie-Baxter treatment at small size scales is the central topic of this thesis.

The first question is whether or not such a breakdown occurs when domain size becomes commensurate in size to the solvent molecules. The computational models examined show that wetting behavior varies at smaller scales, and it is desirable to find experimental support for this occurring. Furthermore, identifying the size range at which this behavior becomes observable is an experimental goal of this thesis.

Second, possible reasons behind the size-dependence of interfacial energy will be investigated. The ideal outcome of this line of research is a new formulation for calculating the interfacial energy of a patchy surface that is applicable for domains of all sizes and patterns. In order to replace or extend the Cassie-Baxter formula, it is necessary to understand when and why it breaks down, and what mechanisms must be considered when adapting it to molecular-scale patchy surfaces.

2.5 References

(1) Gao; McCarthy, T. J. *Langmuir* **2007**, *23*, 13243-13243.
(2) Gao, L.; McCarthy, T. J. *Langmuir* **2007**, *23*, 3762-3765.
(3) Gao, L.; McCarthy, T. J. *Langmuir* **2009**, *25*, 14105-14115.
(4) Gao, L.; McCarthy, T. J. *Langmuir* **2009**, *25*, 7249-7255.
(5) Forsberg, P. S. H.; Priest, C.; Brinkmann, M.; Sedev, R.; Ralston, J. *Langmuir* **2009**, *26*, 860-865.
(6) Seemann, R.; Brinkmann, M.; Kramer, E. J.; Lange, F. F.; Lipowsky, R. *Proc. Natl. Acad. Sci. U. S. A.* **2005**, *102*, 1848-1852.
(7) Woodward, J. T.; Gwin, H.; Schwartz, D. K. *Langmuir* **2000**, *16*, 2957-2961.
(8) Laibinis, P. E.; Bain, C. D.; Nuzzo, R. G.; Whitesides, G. M. *The Journal of Physical Chemistry* **1995**, *99*, 7663-7676.

(9) Bain, C. D.; Troughton, E. B.; Tao, Y. T.; Evall, J.; Whitesides, G. M.; Nuzzo, R. G. *Journal of the American Chemical Society* **1989**, *111*, 321-335.

(10) Drelich, J.; Wilbur, J. L.; Miller, J. D.; Whitesides, G. M. *Langmuir* **1996**, *12*, 1913-1922.

(11) Folkers, J. P.; Gorman, C. B.; Laibinis, P. E.; Buchholz, S.; Whitesides, G. M.; Nuzzo, R. G. *Langmuir* **1995**, *11*, 813-824.

(12) Folkers, J. P.; Laibinis, P. E.; Whitesides, G. M.; Deutch, J. *The Journal of Physical Chemistry* **1994**, *98*, 563-571.

(13) Haag, R.; Rampi, M. A.; Holmlin, R. E.; Whitesides, G. M. *Journal of the American Chemical Society* **1999**, *121*, 7895-7906.

(14) Harder, P.; Grunze, M.; Dahint, R.; Whitesides, G. M.; Laibinis, P. E. *Journal of Physical Chemistry B* **1998**, *102*, 426-436.

(15) Holmlin, R. E.; Chen, X.; Chapman, R. G.; Takayama, S.; Whitesides, G. M. *Langmuir* **2001**, *17*, 2841-2850.

(16) Kim, E.; Whitesides, G. M. *Journal of Physical Chemistry B* **1997**, *101*, 855-863.

(17) Laibinis, P. E.; Fox, M. A.; Folkers, J. P.; Whitesides, G. M. *Langmuir* **1991**, *7*, 3167-3173.

(18) Laibinis, P. E.; Whitesides, G. M. *Journal of the American Chemical Society* **1992**, *114*, 1990-1995.

(19) Laibinis, P. E.; Whitesides, G. M.; Allara, D. L.; Tao, Y. T.; Parikh, A. N.; Nuzzo, R. G. *Journal of the American Chemical Society* **1991**, *113*, 7152-7167.

(20) Mrksich, M.; Whitesides, G. M. *Annu. Rev. Biophys. Biomolec. Struct.* **1996**, *25*, 55-78.

(21) Prime, K. L.; Whitesides, G. M. *Science* **1991**, *252*, 1164-1167.

(22) Giovambattista, N.; Debenedetti, P. G.; Rossky, P. J. *J. Phys. Chem. C* **2007**, *111*, 1323-1332.

(23) Giovambattista, N.; Lopez, C. F.; Rossky, P. J.; Debenedetti, P. G. *Proc. Natl. Acad. Sci. U. S. A.* **2008**, *105*, 2274-2279.

(24) Acharya, H.; Vembanur, S.; Jamadagni, S. N.; Garde, S. *Faraday Discuss.* **2010**, *146*, 353-365.

(25) Kyte, J.; Doolittle, R. F. *J. Mol. Biol.* **1982**, *157*, 105-132.

Chapter 3: The Experimental System and Methods

3.1 Preparation of Model Heterogeneous Surfaces

In Chapter 1, the origin of interfacial energy was shown to be the intermolecular forces acting at the interface and the resulting reorganization of the local liquid. This effect has been studied primarily for homogeneous surfaces where the chemical composition and surface morphology is constant at every point. Studies have also probed the effect of wetting on heterogeneous surfaces, but the interfaces studied have generally contained several, large homogeneous domains such as those of the patchy monolayers discussed in Chapter 2. The interfaces of interest are heterogeneous at a significantly smaller size range, commensurate in size to the liquid molecules and thickness of the interface itself. Due to the difficulty of producing surfaces with controlled composition and controllable domain size in the size range of interest, the wetting behavior of such surfaces is largely experimentally unexplored, and is best understood computationally. While theories have been developed to describe wetting trends on heterogeneous surfaces, it is not known whether or not they break down once the domain size becomes comparable to the interfacial thickness.

To experimentally probe the wetting behavior of patterned surfaces, surfaces with controlled composition and tunable domain size must be produced. Furthermore, to facilitate experimental measurements, ideal candidate surfaces would be smooth, without defects, and relatively stable. Two relatively new classes of materials, self-assembled monolayers (SAMs) and nanoparticle films will be used. The structure, background, and preparation of surface systems studied in this thesis are described below.

3.2 Self-Assembled Monolayers

Self-assembled monolayers were first studied in the 1950s by Zisman[1,2] and later by Nuzzo, Allara and Whitesides in the 1980s[3,4] when it was found that linear alkanes with a terminal functional group would adsorb to form ordered arrays on clean surfaces of aluminum oxide or coinage metals. While molecular monolayers had been previously studied by Langmuir-Blodgett techniques[5], the monolayers formed on solid substrates exhibit remarkable, two-dimensional ordering and permitted measurements of a flat, stable surface. While several chemistries exist for tethering organic molecules to inorganic substrates, the gold-thiol system has been especially prominent in surface chemistry research due to the stability of the resulting monolayer stemming from the strength of the thiol-gold bond and the chemical non-reactivity of gold surfaces.

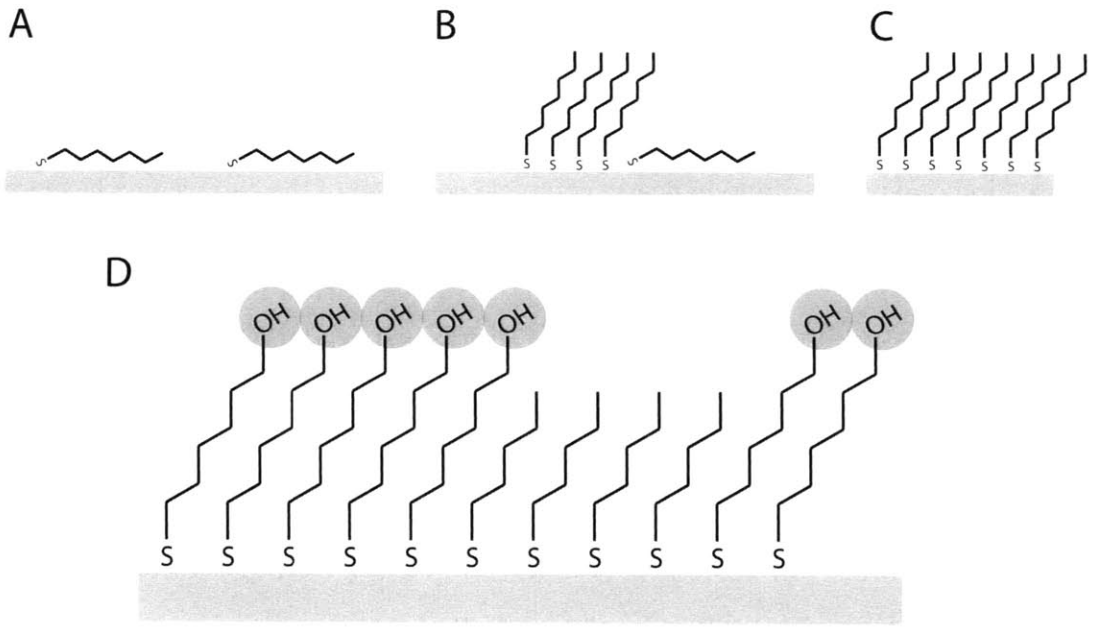

Figure 1. Self-assembled monolayers form on gold using alkylthiols. (A) SAM formation proceeds when alkylthiols begin to adsorb parallel to the gold surface. (B) As additional thiols adsorb, the thiols form islands that stand upright. (C) Thiols continue to adsorb until the surface is almost completely covered. (D) Mixed SAMs can be formed by using

two or more thiols. Here thiols with methyl (yellow) and alcohol (red) headgroups form a mixed SAM.

Work performed in the 90s on thiol on gold SAMs highlighted the flexibility of the system and established thiol-gold SAMs as a platform to enable experimental studies on topics ranging from wetting[3] to catalysis[6] to electrical behavior of single-molecules.[7-9] Because the monolayer is highly ordered and presents a known chemical group at a known orientation, the study of wetting behavior on SAMs has been especially useful.[10,11] A large amount of data exists relating wetting behavior to the identity, position and orientation of the chemical group at the surface.[12-14] Despite this large body of work, the predictive power for more complex chemical groups is low, and the origin of hysteresis on simple SAMs is still poorly understood.[15-17] Despite these shortcomings, SAMs remain a powerful tool to explore interfacial behavior and many studies were devoted to understanding the interaction of biological materials and SAMs.[18]

SAMs are formed by slow adsorption onto a (111) gold surface from solution, commonly over a period of days, resulting in nearly complete coverage of the surface in a hexagonal array commensurate to the underlying gold lattice.[16,19] Growth occurs in two phases: an initial period of adsorption and a second phase where surface density increases accompanied by a reorientation of the molecules perpendicular to the surface.[20] As discussed in Chapter 2, SAMs can be formed using a mixture of thiols. During the growth of a SAM comprised of two or more components, the varying strength of interactions between different species results in phase separation.[21] The kinetics of this phase separation have been measured, and the minimum domain size is observed to be tens of nanometers or larger.[22] Some special ordered states can occur for certain compositions of

mixed SAMs[23] as well, though the vast majority of alkylthiol SAMs form a $\sqrt{3} \times \sqrt{3}R30°$ reconstruction on the surface.[14] Thus while SAMs present a way to produce surfaces with a great degree of order and compositional control, the domain size is not controllable parameter and is determined by the adsorbed species.

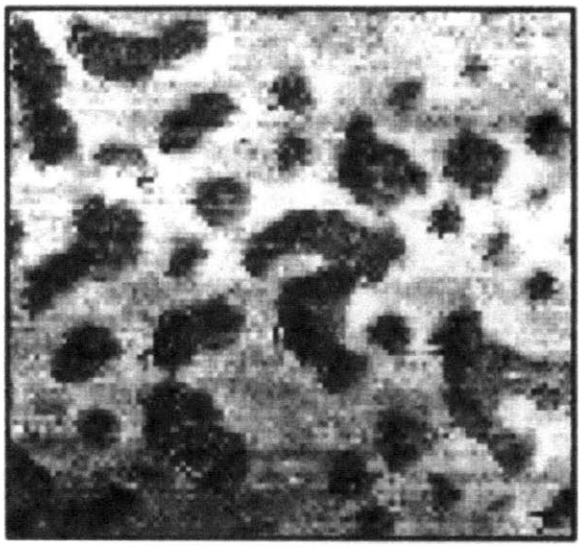

Figure 2. Scanning tunneling microscopy can image the domains formed when a bicomponent SAM phase separates. In the STM image shown, hexadecanethiol and mercaptohexadecanoic acid form domains, with hexadecanethiol appearing darker. The imaged region is approximately 40 nm by 40 nm. Image taken from reference 22.

SAMs will be used in this work as a model heterogeneous surface due to the ease of fabrication and control of composition. The minimal domain size is an order of magnitude greater than the liquid molecule diameter and interfacial thickness. It is expected the wetting behavior of these surfaces will conform to the theories developed previously for heterogeneous surfaces due to the relatively large domain sizes exhibited by these surfaces.

3.3 Introduction to Gold Nanoparticles

Gold nanoparticles are small (<100 nm) crystals of gold, protected with a SAM, that can be synthesized as a solution or dried and treated as a powder. A great deal of research has

focused on using nanoparticles for labeling, detection, and construction of larger objects.[6] In this work, gold nanoparticles present a facile route to generate a SAM with molecular scale domains. The SAM present on the nanoparticle surface is similar in structure to the SAM formed on flat surfaces, with thiol groups bound to the gold surface and head groups comprising the accessible surface. The curvature induced by confining the SAM to the surface of a curved, gold core induces a unique form of phase separation that will be discussed later this chapter.

The existence of gold nanoparticles has been known since Michael Faraday's experiments in colloidal gold in the 1850s.[6] More recently, Turkevitch published a widely used synthesis to generate citrate ion stabilized gold nanoparticles in 1951.[24] In the procedure, an aqueous solution of hydrogen tetrachloroaurate ($HAuCl_4$) is prepared to which sodium citrate is added. The sodium citrate reduces the Au^{3+} ions in solution generating gold crystals with an average diameter of 20 nm protected with a layer of citrate ions. This synthetic procedure is flexible and can be used to generate particles of very different sizes by varying the gold:citrate ratio.[25] Such gold particles are still used in a wide variety of research.[6]

One downside of citrate stabilized and other double layer stabilized particles is that it is impossible to separate the solid solute to permit further post-processing and purification. If a solution of citrate stabilized particles is dried, the gold cores will coalesce and the particles will no longer dissolve.

An important turning point in nanoparticle chemistry occurred with the development of a synthesis that yielded gold nanoparticles that were protected with a self-assembled monolayer. These nanoparticles can be filtered and dried, and subsequently redissolved with no change in the particles. The original synthetic procedure that produced SAM-protected gold nanoparticles was develop by Brust in 1994.[26] This synthesis utilized two phases, one water and the other toluene, to dissolve the gold salt and thiols, respectively. In the procedure, the two phases are stirred in the same vessel and gold salt is dissolved in the aqueous phase. Gold ions are transferred to the organic phase via a phase transfer agent; in the original synthesis this was tetraoctylammonium bromide (TOAB). A thiol compound, originally dodecanethiol, is added and the formation of a gold thiolate complex is observed with the loss of color in the solution. The gold ions are reduced by the slow addition of aqueous sodium borohydride. The organic phase, which now contains monolayer protected gold nanoparticles, is washed repeatedly with water to remove the phase transfer agent. The particles generated using this method range in diameter from 1.5 to 5 nm.

The original rationale of using a two-phase system was due to the differing solubilities of the reagents: the gold salt would not dissolve in toluene, and the thiol would not dissolve in water. One phase synthesis techniques were later developed that used a solvent in which all reagents were mutually soluble. These procedures[27,28] are very similar and can be used to produce nanoparticles of most coin metals, including gold. The synthesis is very similar to the synthesis developed by Brust. The gold salt and thiol are dissolved in the same solution, and an additional solution containing the reducing agent is slowly

added dropwise. The resulting nanoparticles grow and are capped with a monolayer of the thiol present in solution. These particles can later be precipitated, filtered, and washed. The rate at which the reducing agent is added is important, since quick addition often results in increased polydispersity or other problems during growth.[29]

The previous syntheses outlined for producing SAM-coated nanoparticles generate small particles (<10 nm). However, the nanoparticles generated using these methods suffer from a relatively large size dispersion: the width of the size distribution often exceeds 10% or even 20% of the nanoparticle diameter. These poly-dispersed yields are the result of the chemistry employed in the synthesis. The nucleation and growth phases of nanoparticle synthesis are not separate processes; new, smaller crystals continue to nucleate while pre-existing crystals continue to grow.[29]

Several recent attempts have been made to produce nearly mono-dispersed nanoparticles.[30,31] The primarily used synthesis procedure used in this thesis was a modified method developed by Stucky.[32] This method is a simple one-phase synthesis that utilizes a weaker reducing agent to control particle growth. In the original published procedure, hydrogen gold triphenylphosphine chloride is dissolved in benzene with dodecanethiol in a 1:1 molar ratio. After adding the reducing agent, *t*-butyl amine borohydride, at a 10:1 molar ratio to gold, the solution is stirred and heated under reflux for an hour. The size of the nanoparticles is strongly dependent on the temperature at which the reaction takes place. Additionally, it was found that the synthesis is sensitive to the solvent used, with non-polar solvents yielding more mono-dispersed nanoparticles.[32]

In the current body of work, it was necessary to synthesize nanoparticles expressing surface groups that varied from completely hydrophobic to completely hydrophilic. While benzene was successfully used in the original published procedure, ligands used in the current study, 6-mercaptohexanol and 11-mercaptoundecanol, were insoluble in benzene. The use of these ligands was necessary for proper film growth, so a modification to the published synthesis was required. Dichloromethane was identified as a solvent that was sufficiently polar to dissolve these polar ligands and the other reagents, while allowing the synthesized particles to be precipitated, either automatically or with the addition of diethyl ether. The use of a polar solvent broadens the size distribution obtained.[32]

3.4 Purification Methods

The previous listed synthetic methods result in a solution containing the nanoparticles and excess or used reagents. For most applications, before the particles may be used, it is necessary to remove these additional impurities. Several techniques exist to isolate and purifiy nanoparticles. The techniques that will be discussed are vacuum filtration, centrifugation, and dialysis. Centrifugation was primarily used in this work.

Vacuum filtration is a simple and straightforward technique. Following synthesis, if the particles remain soluble in the original solution, a poor solvent must be identified and added to induce precipitation. Following precipitation, the particles are vacuum filtered onto filter paper and washed several times with a solvent capable of dissolving the

impurities and other reagents without dissolving the nanoparticles collected on the filter. The particles are dried on the filter paper and removed as a fine powder.

Another facile method of purification is centrifugation. After synthesis, the particles are precipitated with a poor solvent and centrifuged. The supernatant is poured off and the particles are again dissolved or dispersed. A small quantity of a good solvent can aid in dispersing the nanoparticle pellet, but care must be exercised to not add too much or a significant fraction of the yield will be lost.

Certain impurities, most notably the phase transfer agent TOAB, are very persistent and special techniques must be employed to purify beyond what filtration or centrifugation can accomplish. In Soxhlett extraction, the material to be further purified is placed within a cup of filter material and placed in the Soxhlett apparatus, where a solvent repeatedly rinses the material to be purified. A solvent that is incapable of dissolving the nanoparticles is boiled and recondenses over the material to be purified. For the alcohol and methyl-terminated nanoparticles, acetone and tetrahydrofuran were used. With such a set up, the nanoparticles can be automatically washed as long as desired. This technique has been shown to greatly reduce the amount of impurities, especially the tenacious phase-transfer agent TOAB.[33] However, washing nanoparticles for long periods of time can cause the nanoparticles to aggregate irreversibly. It was experimentally observed that Soxhlett extraction using tetrahydrofuran or especially acetone to purify the nanoparticles used in this thesis would induce aggregation of nanoparticles and produce solubility problems for the resulting material.

Finally, one useful method of purifying nanoparticles is dialysis. In this technique, nanoparticles need not be precipitated prior to purification, and must be in solution for the technique to work properly.[34] This purification technique was used to purify nanoparticles bearing carboxylic acid groups (specifically 11-mercaptoundecanoic acid, 6-mercaptohexanoic acid, and 3-mercaptopropionic acid) as well as nanoparticles presenting sulphonate groups (3-mercaptopropyl sulfonic acid), all of which are water soluble. To perform dialysis, the nanoparticle sample to be purified is placed in a length of sealed dialysis tubing and suspended in a large container of pure solvent. The pore size of the tubing is chosen so that impurities can diffuse out through the tubing while the particles remain. This technique is notable because it is the only technique that does not require the nanoparticles to be precipitated prior to purification, and it can separate water-soluble nanoparticles from salts that are only water-soluble. The only caveat when using this technique is that the pH of the solution may shift enough that the nanoparticles become insoluble and aggregate.

3.5 Phase Separation within a Nanoparticle's Monolayer

The monolayers on a nanoparticle are structurally analogous to the monolayers formed on flat gold surfaces. For both monolayers, the thiols adsorb to the gold surface and form a comparatively dense monolayer. The head groups project outward and comprise the accessible surface of the nanoparticle. In contrast to SAMs formed on flat gold surfaces, the large intrinsic curvature of the nanoparticle monolayer gives rise to phenomena unique to monolayers assembled on nanoparticles and other highly curved surfaces.

Gold nanoparticles synthesized with a two-component SAM display a unique form of phase separation. First observed with scanning tunneling microscopy (STM), the monolayer was observed to exhibit a striated, periodic structure. This morphology was not observed on nanoparticles synthesized using a single thiol, where only individual head groups could be imaged. The spacing between the observed stripes was found to vary with composition and was on the order of the width of an alkylthiol.[35,36] Further studies confirmed that the spacing was not an imaging artifact by establishing that the spacing was independent of the speed at which the region was scanned.[37]

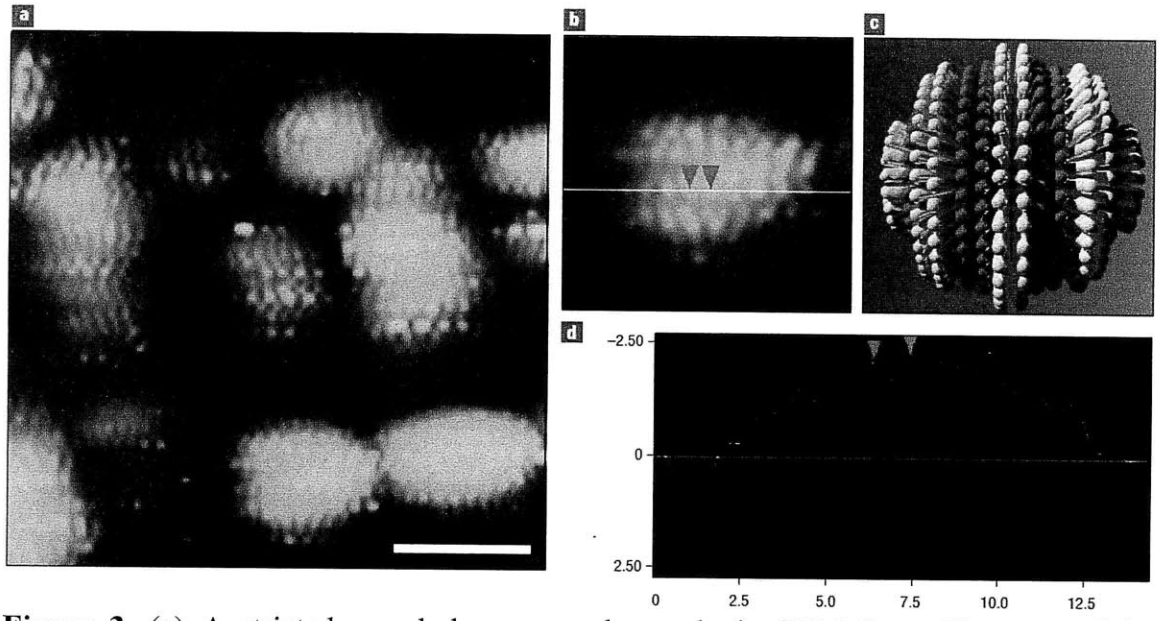

Figure 3. (a) A striated morphology was observed via STM for gold nanoparticles synthesized with a bicomponent monolayer. In this instance, the monolayer consisted of 1-octanethiol and the significantly shorter 3-mercaptopropionic acid. The scale bar represents 10 nm. (b,d) The spacing is defined as the distance between peaks in the height, seen from above (b) and as a cross-section (d). (c) The original structure that was proposed suggested that phase separation resulted in narrow domains. Taken from reference [36].

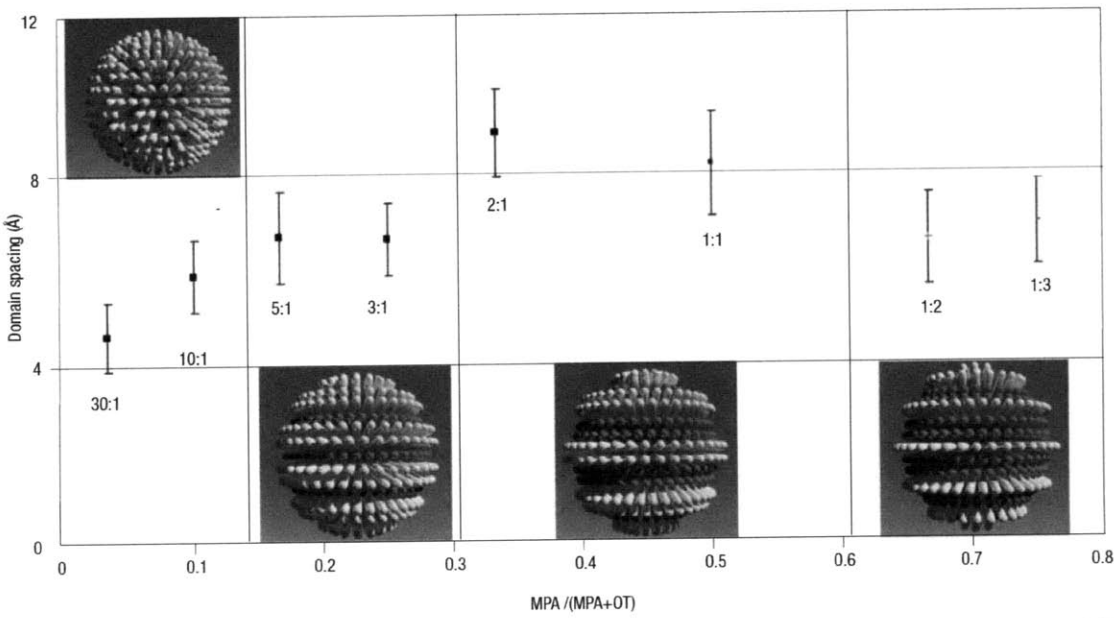

Figure 4. The domain spacing was measured for nanoparticles containing 1-octanethiol (OT) and 3-mercaptopropionic acid (MPA) at numerous ratios. The spacing was consistent with the width of the proposed molecular scale domains. Taken from reference [36].

Phase separation of a two-component SAM on a flat surface is enthalpic in nature and is driven by the intermolecular forces between ligands. Generally, longer molecules tend to overlap more with other longer molecules, and thus have greater van der Waals forces between them. This attractive force leads to the formation of domains. The causes of phase separation on a curved surface have been investigated with molecular dynamics simulations.[38] While attractive forces are still present between the molecules in curved monolayers, the splay caused by being tethered to a curved surface affects the entropic component of the monolayer. The enthalpic benefits longer ligands would experience by remaining adjacent to other longer ligands is offset by entropic benefit gained by forming narrow domains and allowing the tails of the longer ligands to occupy a greater volume. This behavior has been observed with STM on gold and silver nanoparticles.[35-37,39] Furthermore, simulations have found that phase separation may even occur due to surface stresses induced by curvature of the substrate.[40]

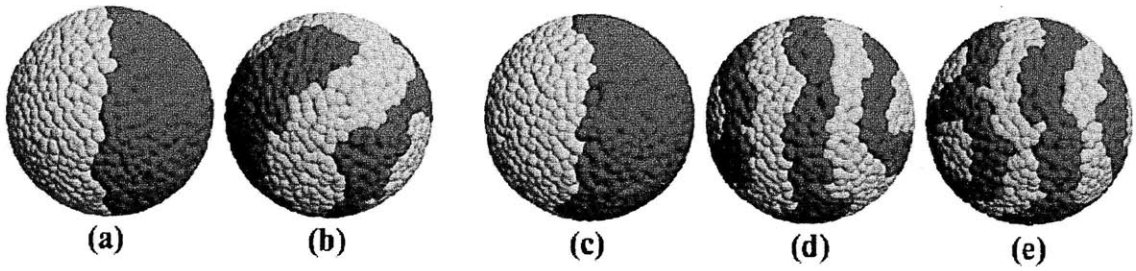

Figure 5. Simulations were used to predict bicomponent monolayer morphology for a variety of conditions. (a) Striped domains did not form when the components were of equal length and identically bulky. (b) When one component possessed a larger headgroup and was more bulky, a contorted morphology appeared. Phase separation is also driven by thiol length in simulations where the headgroup bulkiness was equal (c-e). The equilibrium morphology changed as the length ratio varied from 4:6 (c) to 4:7 (d) to 4:13 (e). Taken from reference [38].

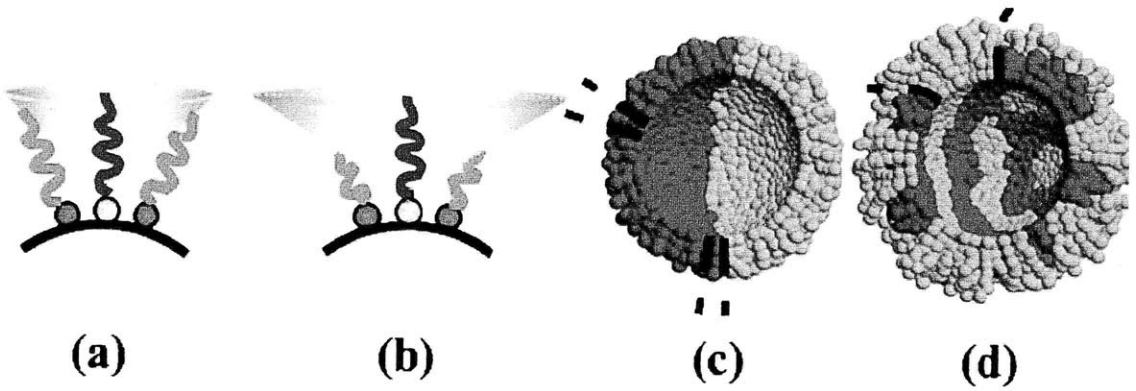

Figure 6. The volume accessible to a thiol surrounded by other thiols of equal length (a) is compared to a longer thiol surrounded by shorter thiols (b). The longer thiol can access volume above shorter thiols, represented by the cone. This is clearly seen when a section of the monolayer is examined. (c) Thiols of equal length access the same volume. (d) Longer thiols adjacent to shorter thiols can access the space above the shorter thiol. Taken from reference [38].

The monolayer morphology has been related to several interesting effects. Nanoparticles cast from solution and allowed to dry on a surface tend to form closely packed nanoparticles films due to assembly via capillary forces. The monolayers can interdigitate or become enmeshed, allowing the core spacing to be below the thickness of two monolayers. Nanoparticles containing a bicomponent monolayer pack more closely than nanoparticles containing a homogenous monolayer comprised of the longer thiol,

indicating a striated morphology affects the ability for particles to interdigitate.[41] Compositionally related morphological changes have also been observed using FTIR spectroscopy. Shifts in the thiols' vibrational peaks demonstrate that the local environment of each component varies depending on composition and morphology.[39]

Additionally, monolayer morphology has been related to interesting behavior with biological membranes. Nanoparticles protected with striated monolayers of certain compositions can diffuse through cell membranes without causing poration or requiring activity from the cell. Nanoparticles whose monolayers have similar surface composition but a non-striated morphology do not passively diffuse through the cell membrane.[42]

Striped nanoparticles can also be used as components of larger systems. A striped monolayer possesses two topological defect sites at the poles of the nanoparticle. In contrast to the rest of the monolayer, these sites are more reactive and more prone to replacement from other thiols in solution. These two sites can be functionalized with reactive groups, allowing the nanoparticles to be cross-linked to form chains.[43] The kinetics of chain formation have been studied[44], and the chemistry has been extended to non-gold/thiol systems, allowing chains of magnetic particles to be assembled.[45] Because the topological defects only exist for nanoparticles with ordered stripes (as in Fig. 5d, in contrast to Fig. 5b), the formation of chains can serve as an indicator of monolayer morphology. Experiments have shown that only intermediate sized particles (2-8 nm) form chains, consistent with results from computer modeling that showed ordered strips would exist only within a range of core sizes.[46]

The morphology of a nanoparticle's monolayer also greatly influences its solubility. Related to the expected linear trend observed for two component SAMs discussed in Section 2.2, if one component of a nanoparticle's monolayer is wetted better by a solvent, the expected trend of nanoparticle solubility in that solvent would be monotonically increasing as that component's fraction increased. This is not the case however, and the experimentally determined solubility trends (Fig. 7) are far more complex than this. Depending on the solvent, the highest solubilities are observed only for the most hydrophobic nanoparticles (Fig. 7a-c), solubility increases with decreasing hydrophilic content reaching a maximum at an intermediate composition (Fig. 7h-j), or only specific compositions are soluble (Fig. 7k-l).[47] The data strongly suggest that monolayer structure influences solubility. As the formation of an interface is a large component to solubilizing an object, these solubility trends indirectly show a complex relationship between structure and interfacial energy.

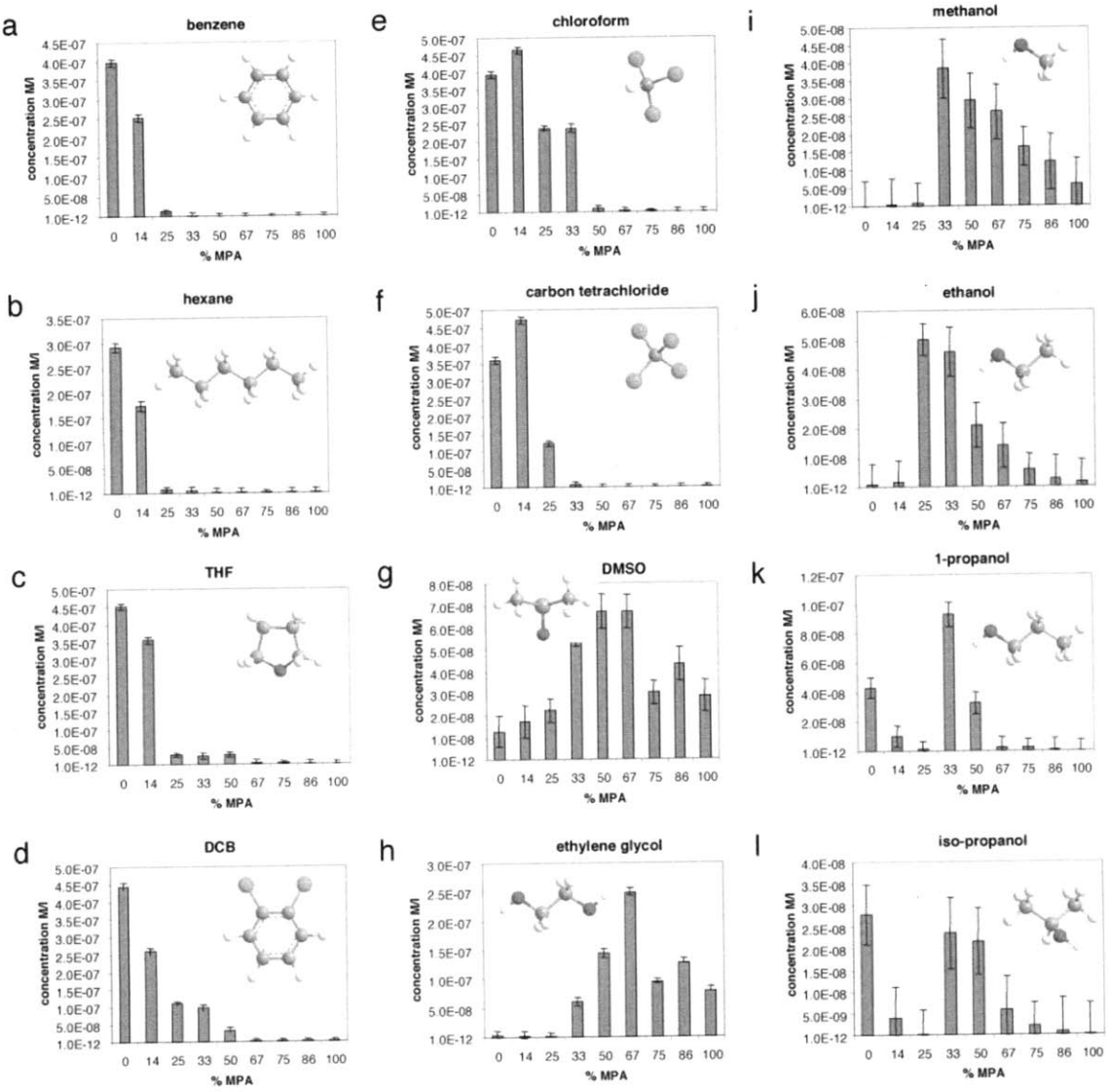

Figure 7. Nanoparticles were synthesized with monolayers containing 1-octanethiol (OT) and 3-mercaptopropionic acid (MPA) at numerous compositions. The saturation concentration (M/L) of the nanoparticles in different solvents was determined via UV/Vis Spectroscopy. The trend of saturation concentration with respect to composition is complex and demonstrates the complicated relationship between surface structure and solubility. Taken from reference [47].

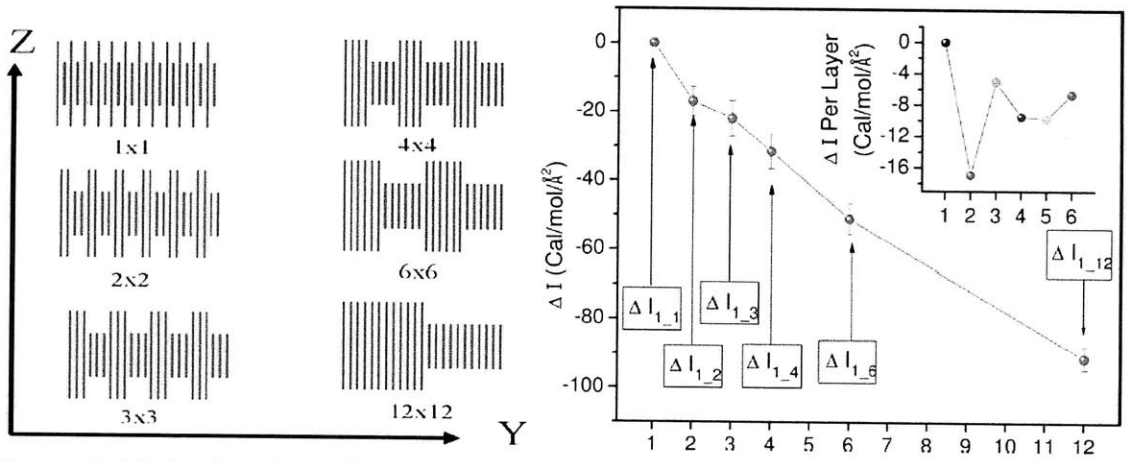

Figure 8. Molecular dynamics simulations indicate a structural dependence of interfacial energy. The interfacial energy of SAMs with identical composition but different structures were investigated. The *nxn* nomeclature (left) denotes *n* rows of OT followed by *n* rows of MPA. This motif was repeated until the total system size simulated was 24 rows. The solvent used was ethanol. (right) The change in interfacial energy is shown with (inset) the change per layer, or row, of thiols. This trend is not constant as would be expected if structure played no role. Taken from reference [47].

3.6 Characterization Methods for Nanoparticles

Several methods are available for characterizing nanoparticles. These techniques were used to ensure the nanoparticles synthesized were the correct size and composition, sufficiently pure, and soluble.

UV-VIS Spectroscopy provides a simple method to assess the solubility of nanoparticles. Small gold nanoparticles in solution have a well-defined and thoroughly characterized peak at 530 nm due to the gold core's surface plasmon.[6] UV-Vis spectroscopy can quickly determine if the synthesized nanoparticles are outside of the desired size range. Furthermore, since many other factors including size and aggregation, affect the absorption spectrum, this technique provides a means to quickly diagnose problems in nanoparticle solutions. Finally, the height of the plasmon's peak reflects the concentration of nanoparticles in solution for a range of concentrations. Thus, UV-Vis

spectroscopy provides a way of quantitatively determining the concetration of nanoparticles in solution provided a standard solution.[47]

Transmission electron microscopy (TEM) is the most direct method of determining nanoparticle core size. Additionally, TEM presents a means to assess the quality of the nanoparticles synthesized. Aberrations in morphology and the level of aggregation present are easily apparent when imaging particles using TEM. Nanoparticles are known to size segregate when allowed to slowly dry after being cast; thus to ensure a representative sample of nanoparticles is imaged, the liquid must be rapidly remove. Experimentally, this is accomplished by drop-casting TEM grids on an absorbent material to wick away the excess liquid.

Scanning probe microscopy techniques are best adapted to evaluate the structure of the monolayer present on nanoparticles. Scanning tunneling microscopy (STM) provides a method to image the monolayer morphology. The technique relies on the extreme sensitivity of the tunneling current between a sample and an atomically sharp metallic tip on distance. Molecular resolution is possible and individual ligands can be resolved.[36,37] Atomic force microscopy (AFM) is another scanning probe technique that under certain conditions can achieve molecular resolution of the nanoparticle monolayer. The combination of these techniques can prove the morphology of nanoparticles at a given composition is the expected morphology.

Dynamic light scattering (DLS) can be used to determine the size distribution of nanoparticles in solution. The nanoparticles used in the current work however, are smaller than the lower limit the technique can accurately size. Thus, DLS does not present a way of determining the size of nanoparticles, but rather a method of confirming the absence of nanoparticle aggregates in solution which would be large enough for DLS to detect.[48]

Finally, nuclear magnetic resonance (NMR) is a powerful tool for characterizing nanoparticles. Following synthesis and purification, a small sample of nanoparticles canbe used to produce a solution in a deuterated solvent. The presence of any free thiol, remaining reagent or other impurities is indicated as sharp peaks in the spectrum. Second, NMR can be used to confirm the composition of nanoparticles. Before aquiring the spectrum, the nanoparticles must first be decomposed to liberate the adsorbed thiols. The decomposition is most readily achieved using a solution of iodine or potassium cyanide. As iodine is more reactive than potassium cyanide, the latter is preferred. The composition can be calculated from comparing the area of peaks unique to each ligand present on the surface.

3.7 Production of films of nanoparticles

In the first chapter, the relevant length scale of the solid-liquid interface was shown to be on the order of a few molecular diameters. Furthermore, the most interesting, heterogeneous interfaces were shown to have domain scales on the order of a few nanometers or less. While SAMs were presented as a means to readily produce chemically tailored surfaces, the domain size of SAMs formed on flat surfaces was found

to be 10 nm or greater, an order of magnitude greater than the length scale of interest. Thus to probe the effect of domain size on interfacial energy, it is necessary to study domains commensurate in size with the molecular diameter of the probe liquid. That is, to fully characterize the effect of composition and domain size, molecular-scale domains must be considered.

SAMs confined to the surface of nanoparticles were shown to exhibit domains as narrow as a single molecule and thus would be an ideal system to study size-dependent effects; however, the established measurement techniques for interfacial energy described in chapter one require macroscopic surfaces. The interfacial energy of nanoparticles can be linked to the saturation concentration in solution; however, solubility is a complex phenomena[47,49], and there would likely be several factors obscuring the role of interfacial energy.

In order to extend the traditional measurement techniques described in the first chapter to the experimentally interesting system presented by structured nanoparticle monolayes, macroscopic surfaces must be constructed from nanoparticles. Nanoparticle films have been studied for numerous applications including catalysis, electrochemistry, sensors, and electronic devices.[6] Several methods have been developed for producing nanoparticle films.

The methods that follow belong to a larger class of film production techniques known as layer-by-layer growth.[50-54] The common motif in this family of techniques is a stepwise

deposition of layers, generally alternating between two materials capable of chemically bonding or otherwise exhibiting an affinity for each other, to build up a film. The first layer of nanoparticles is adhered to the surface using a compound capable of cross-linking the substrate to the nanoparticles gold core. Subsequent layers are deposited by alternatively immersing the film in a solution of cross-linker molecules and the nanoparticle solution. This process can be repeated indefinitely to produce films of the desired thickness. A similar technique exists that uses electrostatic forces to bond layers.[55-57] These films use polyelectrolytes to adhere the nanoparticles to the surface and are suitable only for nanoparticles containing charged groups only, such as carboxylates or sulfonates. The methods used to produce films are described in Appendix A.

3.8 Methods Used to Determine Interfacial Energy

Chapter 1 outlined methods used in general to measure interfacial energy. The most commonly used technique is contact angle measurements, where a drop is placed on a surface and the interfacial energies are calculated from its geometry. This is the primarily used technique in this thesis. The method of tensiometry was also employed to a lesser degree when measuring.

A technique employing an atomic force microscope developed in the scope of this thesis was used to confirm the values of interfacial energy obtained by contact angle measurements in this thesis. Atomic force microscopy (AFM) is often used to generate microsopic topographic images of surfaces with nanometer or even sub-nanometer precision. One variation of the imaging technique, called amplitude modulated AFM (AM-AFM), a cantilever is oscillated at a fixed frequency above a substrate, and the

substrate is moved up or down to maintain the cantilever's vibration amplitude. The probe is scanned across the substrate in a raster-like pattern, producing two sets of data: one of the surface topography and another of the phase difference between the cantilever's actual motion and the cantilever's driving function. AM-AFM can be performed in air, under liquid, or in vacuum. To measure the interfacial energy, a technique termed small amplitude modulation-atomic force microscopy (SAM-AFM) is used. Both the substrate and cantilever are immersed in the probe liquid and the amplitude of the cantilever oscillation is set to be on the order of a nanometer, significantly less than typical amplitudes used during normal imaging conditions. With such a small amplitude of oscillation, the tip of the cantilever will traverse only the interfacial liquid in close proximity to the substrate.

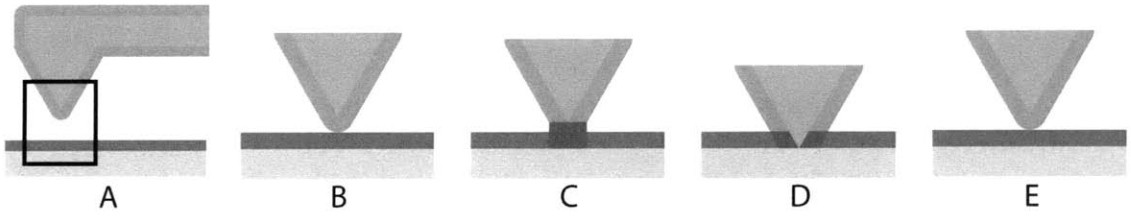

Figure 9. (a) When imaging in a liquid (not shown for clarity), both the cantilever and substrate being imaged will form a solid-liquid interface with the liquid. The volume in close proximity to the surface, or interfacial water, is highlighted for both the cantilever (blue) and the surface (red). (b) In SAM-AFM, the cantilever oscillation is minimal. At the ideal amplitude set point, no bulk liquid exists between the interfacial regions, and the interfacial regions do not intersect. (c) As the tip approaches the surface, the liquid is expelled until (d) the tip just contacts the substrate. (e) To complete the cycle, the tip retracts from the surface, allowing the liquid interfaces to reform.

The interfacial energy can be related to energy lost during each oscillation cycle. As the tip approaches the solid surface, both the tip-liquid and surface-liquid interfaces are destroyed and a new tip-surface interface is formed. In addition to losses due to forming interfaces, other energy losses are incurred from the cantilever's movement in a viscous

medium. To calculate the energy loss, the cantilever is modeled as a mass-spring-damper system; the damping coefficient represents the sum of energy losses. Prior to measuring interfacial energy, the cantilever is calibrated in liquid. By subtracting the phase offset when the tip is far from the substrate (i.e. in what can be considered the bulk liquid) from the phase offset when the tip is probing the interfacial liquid, the energy losses into the bulk liquid can be excluded, and the remaining losses can be assumed to be solely due to surface/tip and interfacial water/tip interactions. It is assumed that during one cycle, the cantilever tip displaces the interfacial liquid in a small volume when it approaches, and the liquid interface reforms when the tip retracts. By reducing the amplitude of the oscillation until tip/substrate interactions are minimal, the energy dissipated per oscillation cycle into the interfacial liquid can be calculated. As the energy to complete the cycle is related to the interfacial energy of the liquid/solid interface by the definitions in Section 1.3, this technique is capable of measuring the local interfacial energy. By calculating the energy dissipated destroying the surface/liquid interface for each point in the phase image, a mapping of the interfacial energy of the interface can be constructed from the phase data. The values for each point can then be averaged to yield the interfacial energy of the substrate.[58]

This technique requires significantly more time and equipment to perform compared to the previous techniques. The value of this technique lies in its ability to produce a map of interfacial energy and its ability to quantify interfacial energy away from the 3-phase line. By showing agreement between measurements from contact angles and this technique, the interfacial energy measured can be verified as representing the interface's average

value, and not a false value due to experimental errors such as contact angle pinning or defects of the surface.

3.9 References

(1) Shafrin, E. G.; Zisman, W. A. *Journal of Colloid Science* **1952**, *7*, 166-177.

(2) Schulman, F.; Zisman, W. A. *Journal of the American Chemical Society* **1952**, *74*, 2123-2124.

(3) Laibinis, P. E.; Whitesides, G. M.; Allara, D. L.; Tao, Y. T.; Parikh, A. N.; Nuzzo, R. G. *Journal of the American Chemical Society* **1991**, *113*, 7152-7167.

(4) Allara, D. L.; Nuzzo, R. G. *Langmuir* **1985**, *1*, 45-52.

(5) Roberts, G. G. *Contemporary Physics* **1984**, *25*, 109 - 128.

(6) Daniel, M. C.; Astruc, D. *Chemical Reviews* **2004**, *104*, 293-346.

(7) Haag, R.; Rampi, M. A.; Holmlin, R. E.; Whitesides, G. M. *Journal of the American Chemical Society* **1999**, *121*, 7895-7906.

(8) Austin, M. D.; Chou, S. Y. *Nano Lett.* **2003**, *3*, 1687-1690.

(9) Hybertsen, M. S.; Venkataraman, L.; Klare, J. E.; Cwhalley, A.; Steigerwald, M. L.; Nuckolls, C. *J. Phys.-Condes. Matter* **2008**, *20*, 14.

(10) Laibinis, P. E.; Whitesides, G. M. *Journal of the American Chemical Society* **1992**, *114*, 1990-1995.

(11) Laibinis, P. E.; Fox, M. A.; Folkers, J. P.; Whitesides, G. M. *Langmuir* **1991**, *7*, 3167-3173.

(12) Harder, P.; Grunze, M.; Dahint, R.; Whitesides, G. M.; Laibinis, P. E. *Journal of Physical Chemistry B* **1998**, *102*, 426-436.

(13) Kim, E.; Whitesides, G. M. *Journal of Physical Chemistry B* **1997**, *101*, 855-863.

(14) Laibinis, P. E.; Bain, C. D.; Nuzzo, R. G.; Whitesides, G. M. *The Journal of Physical Chemistry* **1995**, *99*, 7663-7676.

(15) Folkers, J. P.; Gorman, C. B.; Laibinis, P. E.; Buchholz, S.; Whitesides, G. M.; Nuzzo, R. G. *Langmuir* **1995**, *11*, 813-824.

(16) Folkers, J. P.; Laibinis, P. E.; Whitesides, G. M. *J. Adhes. Sci. Technol.* **1992**, *6*, 1397-1410.

(17) Li, G.; Flores, S. M.; Vavilala, C.; Schmittel, M.; Graf, K. *Langmuir* **2009**, *25*, 13438-13447.

(18) Prime, K. L.; Whitesides, G. M. *Science* **1991**, *252*, 1164-1167.

(19) Bain, C. D.; Troughton, E. B.; Tao, Y. T.; Evall, J.; Whitesides, G. M.; Nuzzo, R. G. *Journal of the American Chemical Society* **1989**, *111*, 321-335.

(20) Schreiber, F. *Prog. Surf. Sci.* **2000**, *65*, 151-256.

(21) Folkers, J. P.; Laibinis, P. E.; Whitesides, G. M.; Deutch, J. *The Journal of Physical Chemistry* **1994**, *98*, 563-571.

(22) Stranick, S. J.; Parikh, A. N.; Tao, Y. T.; Allara, D. L.; Weiss, P. S. *The Journal of Physical Chemistry* **1994**, *98*, 7636-7646.

(23) Holmlin, R. E.; Chen, X. X.; Chapman, R. G.; Takayama, S.; Whitesides, G. M. *Langmuir* **2001**, *17*, 2841-2850.

(24) Turkevich, J.; Stevenson, P. C.; Hillier, J. *Discussions of the Faraday Society* **1951**, 55-&.

(25) Frens, G. *Nature-Physical Science* **1973**, *241*, 20-22.

(26) Brust, M.; Walker, M.; Bethell, D.; Schiffrin, D. J.; Whyman, R. *Journal of the Chemical Society, Chemical Communications* **1994**, 801-802.

(27) Yee, C. K.; Jordan, R.; Ulman, A.; White, H.; King, A.; Rafailovich, M.; Sokolov, J. *Langmuir* **1999**, *15*, 3486-3491.

(28) Kang, S. Y.; Kim, K. *Langmuir* **1998**, *14*, 226-230.

(29) Kimling, J.; Maier, M.; Okenve, B.; Kotaidis, V.; Ballot, H.; Plech, A. *Journal of Physical Chemistry B* **2006**, *110*, 15700-15707.

(30) Stoeva, S. I.; Smetana, A. B.; Sorensen, C. M.; Klabunde, K. J. *Journal of Colloid and Interface Science* **2007**, *309*, 94-98.

(31) Smetana, A. B.; Klabunde, K. J.; Sorensen, C. M. *Journal of Colloid and Interface Science* **2005**, *284*, 521-526.

(32) Zheng, N.; Fan, J.; Stucky, G. D. *Journal of the American Chemical Society* **2006**, *128*, 6550-6551.

(33) Waters, C. A.; Mills, A. J.; Johnson, K. A.; Schiffrin, D. J. *Chem. Commun.* **2003**, 540-541.

(34) Sweeney, S. F.; Woehrle, G. H.; Hutchison, J. E. *Journal of the American Chemical Society* **2006**, *128*, 3190-3197.

(35) Jackson, A. M. Ph.D. Thesis, M.I.T., 2007.

(36) Jackson, A. M.; Myerson, J. W.; Stellacci, F. *Nat Mater* **2004**, *3*, 330-336.

(37) Jackson, A. M.; Hu, Y.; Silva, P. J.; Stellacci, F. *Journal of the American Chemical Society* **2006**, *128*, 11135-11149.

(38) Singh, C.; Ghorai, P. K.; Horsch, M. A.; Jackson, A. M.; Larson, R. G.; Stellacci, F.; Glotzer, S. C. *Physical Review Letters* **2007**, *99*, 4.

(39) Centrone, A.; Hu, Y.; Jackson, A. M.; Zerbi, G.; Stellacci, F. *Small* **2007**, *3*, 814-817.

(40) Singh, C.; Jackson, A. M.; Stellacci, F.; Glotzer, S. C. *Journal of the American Chemical Society* **2009**, *131*, 16377-+.

(41) Hu, Y.; Uzun, O.; Dubois, C.; Stellacci, F. *Journal of Physical Chemistry C* **2008**, *112*, 6279-6284.

(42) Verma, A.; Uzun, O.; Hu, Y. H.; Hu, Y.; Han, H. S.; Watson, N.; Chen, S. L.; Irvine, D. J.; Stellacci, F. *Nat. Mater.* **2008**, *7*, 588-595.

(43) DeVries, G. A.; Brunnbauer, M.; Hu, Y.; Jackson, A. M.; Long, B.; Neltner, B. T.; Uzun, O.; Wunsch, B. H.; Stellacci, F. *Science* **2007**, *315*, 358-361.

(44) DeVries, G. A.; Talley, F. R.; Carney, R. P.; Stellacci, F. *Adv. Mater.* **2008**, *20*, 4243-4247.

(45) Nakata, K.; Hu, Y.; Uzun, O.; Bakr, O.; Stellacci, F. *Adv. Mater.* **2008**, *20*, 4294-4299.

(46) Carney, R. P.; DeVries, G. A.; Dubois, C.; Kim, H.; Kim, J. Y.; Singh, C.; Ghorai, P. K.; Tracy, J. B.; Stiles, R. L.; Murray, R. W.; Glotzer, S. C.; Stellacci, F. *Journal of the American Chemical Society* **2008**, *130*, 798-+.

(47) Centrone, A.; Penzo, E.; Sharma, M.; Myerson, J. W.; Jackson, A. M.; Marzari, N.; Stellacci, F. *Proc. Natl. Acad. Sci. U. S. A.* **2008**, *105*, 9886-9891.

(48) Liu, X.; Dai, Q.; Austin, L.; Coutts, J.; Knowles, G.; Zou, J. H.; Chen, H.; Huo, Q. *Journal of the American Chemical Society* **2008**, *130*, 2780-+.

(49) Ben-Naim, A. *Solvation Thermodyanics*; Plenum Press: New York, 1987.

(50) Liu, Y. J.; Wang, Y. X.; Claus, R. O. *Chem. Phys. Lett.* **1998**, *298*, 315-319.

(51) Shipway, A. N.; Katz, E.; Willner, I. *ChemPhysChem* **2000**, *1*, 18-52.

(52) Musick, M. D.; Keating, C. D.; Lyon, L. A.; Botsko, S. L.; Pena, D. J.; Holliway, W. D.; McEvoy, T. M.; Richardson, J. N.; Natan, M. J. *Chem. Mat.* **2000**, *12*, 2869-2881.

(53) McEvoy, T. M.; Pena, D. J.; Musick, M. D.; Richardson, J. N. *J. Electroanal. Chem.* **2004**, *565*, 121-129.

(54) Musick, M. D.; Pena, D. J.; Botsko, S. L.; McEvoy, T. M.; Richardson, J. N.; Natan, M. J. *Langmuir* **1999**, *15*, 844-850.

(55) Lee, D.; Gemici, Z.; Rubner, M. F.; Cohen, R. E. *Langmuir* **2007**, *23*, 8833-8837.

(56) Lee, D.; Rubner, M. F.; Cohen, R. E. *Nano Lett.* **2006**, *6*, 2305-2312.

(57) Yoo, D.; Shiratori, S. S.; Rubner, M. F. *Macromolecules* **1998**, *31*, 4309-4318.

(58) Voitchovsky, K.; Kuna, J. J.; Contera, S. A.; Tosatti, E.; Stellacci, F. *Nat. Nanotechnol.* **2010**, *5*, 401-405.

Chapter 4: Experimental Results

The central goal of this thesis is to experimentally determine whether the Cassie-Baxter relation remains valid for all patchy surfaces or whether the structure of the surface affects interfacial energy. In particular, surfaces with chemically distinct domains of different sizes will be investigated to test if the Cassie-Baxter expression remains consistent for extremely small domains, and if not, to determine domain size effects on interfacial energy. The systems discussed in the previous chapter present routes to generate surfaces with controllable domain size and chemical functionality. To compare the effect of domain size on interfacial energy, surfaces containing the same surface composition but different domain sizes will be produced. Flat SAMs will serve as the control for surfaces with large (>5 nm) domains in contrast to nanoparticle films with molecular-scale domains. By comparing the behavior of the two sets of surfaces, the effect of domain size can be observed.

4.1 Preparation of Surfaces with Large Domains

Surfaces containing large domains were fabricated by forming self-assembled monolayers containing a mixture of two ligands, in this case 1-octanethiol (OT) as the hydrophobic component and 6-mercaptohexanol (MHol) as the hydrophilic component. These ligands were chosen for three primary reasons. First, the headgroups are very dissimilar in terms of wetting properties and SAMs of each exhibit markedly different contact angles. This contrast is necessary to probe the wetting behavior of mixtures of the ligands. Second, the thiols are suitably long to produce stable films. SAMs formed from shorter thiols have poorer coverage of the substrate, and result in less stable nanoparticles.[1-3] Finally, the resulting monolayer is noncharged. Difficulties in forming

films suitable for contact angle measurements using charged nanoparticles required using layer-by-layer assembly to produce films of non-charged particles.

Bicomponent SAMs are known to phase separate into domains on the order of tens of nanometers.[4] To prepare these surfaces, gold on mica was purchased from Agilent. The mica substrates were divided to form samples approximately 1 cm by 1 cm. These substrates were cleaned by immersion in a piranha bath (4:1 sulfuric acid:hydrogen peroxide) at room temperature for 10 mins. Longer cleaning times were observed to drastically increase the roughness of the gold and also promote separation of the gold from the mica surface. The samples were thoroughly rinsed with deionized water (Millipore, 18.2MΩ) and immediately placed in 10 ml of ethanolic thiol solution. The total thiol concentration was 0.01 mM, and, in addition to solutions containing only MHol or OT, the following ratios of MHol:OT were used: 5:1, 2:1, 1:1, 1:2, 1:5. For the remainder of the experimental work, the composition of the surface will be given as a percentage of one component, with the second understood to contribute the balance. Thus, the SAM concentrations correspond to 100%, 87%, 67%, 50%, 33%, 17% and 0% MHol. The SAMs were allowed to form over a period of 7 days. They were rinsed with ethanol and dried under a stream of nitrogen prior to measurements.

Following the formation of the nanoparticle films, the nanoparticles were imaged using TEM. The size distribution data is shown below, and it was seen that all of the particle distributions were similar, and more importantly within the size range known to display a rippled morphology (see Section 2.5). Slight aggregation occurred, likely attributable to

aging of the nanoparticles in solution or cross-linking from contamination, but this did not significantly impact the formation of the films.

Composition (% MHol)	Median Size (nm)	Standard Deviation (nm)
100%	6.3	7.9
83%	3.6	3.0
67%	8.4	6.1
50%	3.8	5.0
33%	4.3	2.1
17%	4.3	2.0
0%	4.8	1.5

Table 1. MHol/OT Nanoparticle Size Distributions

4.2 Wetting Behavior of Surfaces with Large Domains

Contact angle measurements on the SAMs were performed first. The measurements were made using a VCA1000 goniometer (AST Products, Inc.) The probe liquid was Millipore water (18.2 MΩ) The drops were ensured to be advancing evenly and not pinned. The data are shown in Fig. 1 below.

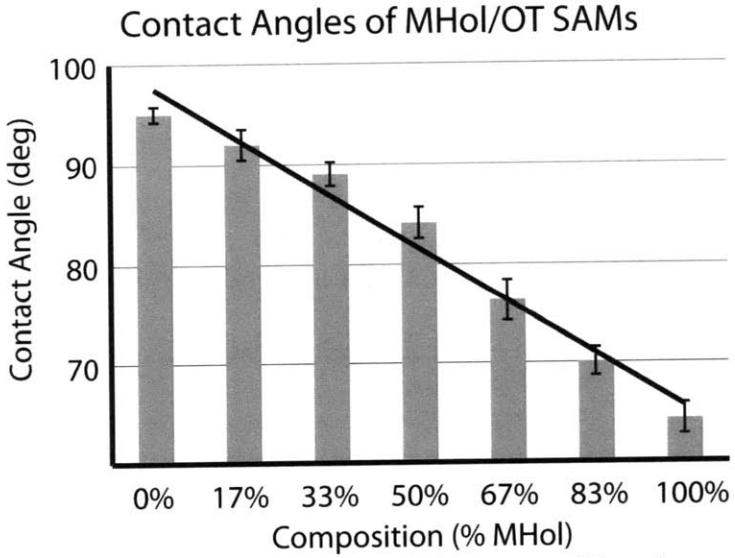

Figure 1. The trend of contact angle is linear with composition, in agreement with the Cassie-Baxter relation. We find that the surface prepared with 0% MHol (100% OT) is the least wetting and has the largest contact angle, with the opposite true for 100% MHol. Each point represents a minimum of 5 measurements, with an average of 9 measurements per composition.

The trend is well described by a linear fit (R^2=0.96), and the Cassie-Baxter relation is clearly adequate to describe these results. After contact angle measurements were performed, the samples were imaged in water (18.2 MΩ, Millipore) using the technique described in Section 3.8, and a representative image is shown below in Fig. 2. The domain size is well above 10 nm, and thus these surfaces would be representative of surfaces bearing large domains. Furthermore, the ratio of the ligands as determined by the ratio of surface area fraction appeared consistent with the nominal composition. The interfacial energy of the SAMs as calculated from the AFM data is plotted against the values obtained from contact angle measurements in Fig. 2.

The measurements obtained using the AFM technique and traditional contact angle measurements are linearly correlated. However, the values calculated using the AFM technique vary noticeably in magnitude from the contact angle data. The difference is due to the error sensitivity of a geometric factor used to account for interface and cantilever-tip geometry, as well as additional losses in the AFM method that remain constant for all measurements.[5]

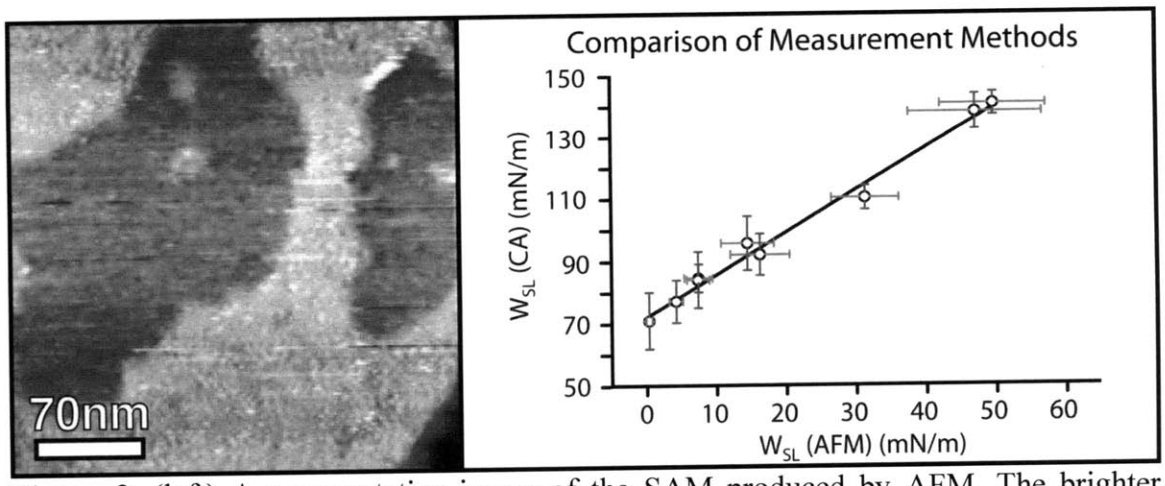

Figure 2. (left) A representative image of the SAM produced by AFM. The brighter regions correspond to domains of the longer ligand, OT, while the darker regions correspond to domains of MHol. The domain size is observed to be on the order of tens of nanometers. (right) The work of adhesion measured using traditional contact angle measurements is contrasted with the work of adhesion obtained using the SAM-AFM technique described in Section 3.8. The values are related via a linear relation, with excellent agreement ($R^2 = 0.98$).

4.3 Synthesis of MHol/OT Nanoparticles

In order to produce nanoparticle films with identical surface compositions as the aforementioned slides, nanoparticles were first synthesized with the same compositions. The method selected to produce these nanoparticles is a modified version of one-phase synthesis.[6] A more common synthetic procedure performed in ethanol[7] was originally tested, but was abandoned as the nanoparticles generated were too soluble in ethanol to be precipitated leading to low yields. The modified procedure was performed in dichloromethane (DCM) and at a smaller scale than the published procedure, as described in the previous chapter.

For these syntheses, the reaction was performed in a sealed round bottom flask while held at 60° C and constantly stirred. Following the addition of the reducing agent, the reaction mixture turned from a transparent solution, to a clear brown solution, until finally

becoming a dark red, opaque solution after approximately 10 minutes. The reaction was allowed to continue for 1 hour, when the flask was removed from the heat bath. After allowing the nanoparticle solution to cool, approximately 50 ml of diethyl ether was added to induce precipitation. Diethyl ether was identified as the only commonly available solvent that could readily precipitate alcohol-bearing nanoparticles.

The nanoparticles were allowed to precipitate overnight. The supernatant, which had a light yellow-brown color indicative of the presence of smaller, non-metallic nanoparticles, was poured off, and the remaining nanoparticles were transferred to 50 ml centrifuge tubes. Diethyl ether was added to reach a volume of 50 ml, and the solutions were centrifuged for 15 min. Following centrifugation, the nanoparticles remained as a pellet at the bottom of the centrifuge tube, and the supernatant was poured off. A small amount of ethanol (< 0.5 ml) was added followed by brief sonication to disperse the pellet. Diethyl ether was added to reach a volume of 50 ml, and this process was repeated five times. The first two cycles would have a supernatant with a slight yellow-brown color, but following cycles were clear, demonstrating the removal of the smaller nanoparticles.

4.4 Preparation of Nanoparticle Films

For the films made with MHol/OT nanoparticles, glass slides were used as the substrate. Each slide was first cleaned with isopropanol, and then with piranha as described in the previous chapter. The slides were rinsed and silanized. Any slides displaying a white, foggy residue after silanization were discarded, as this demonstrates excessive polymerization of the silane due to the presence of water or piranha residue.

Saturated solutions of the nanoparticles were prepared by adding the entire yield of each synthesis to 400 ml of ethanol. The silanized slides were immersed in the nanoparticle solution for 2 days to generate the initial layer. To crosslink the next layer of nanoparticles, the slides were immersed in 400 ml of 10 mM 1,9-nonanedithiol solution in ethanol. To prevent cross-contamination, each set of slides corresponding to a unique composition was crosslinked using its own dithiol solution. Following the deposition of 5 layers, the slides were rinsed with ethanol and allowed to dry.

The quality and coverage of the nanoparticle films were determined by taking sections of the films and imaging with AFM. The areas sampled came from multiple slides and multiple locations within each slide. Representative images of the films are shown below. It is important to note that in every case, the film had achieved complete coverage. That is, for every composition, the film was defect free and nanoparticles completely covered the surface. Furthermore, roughness analysis of the areas imaged (excluding scratches made to estimate film thickness) showed that the films had comparable and low roughness. The roughness of the films is summarized in the chart below.

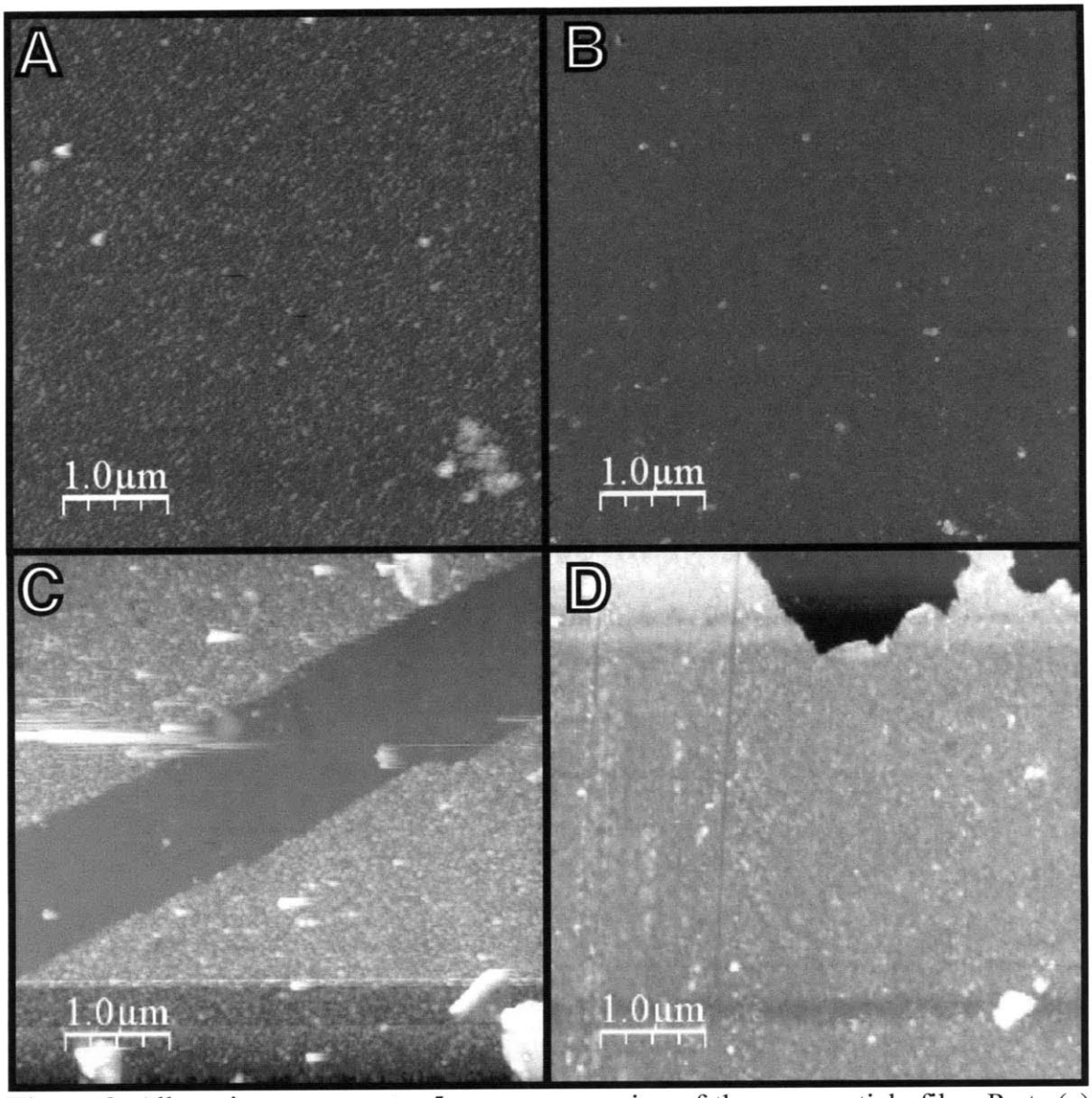

Figure 3. All sections represent a 5 um square region of the nanoparticle film. Parts (a) and (b) show complete coverage by nanoparticles. For (c) and (d), the surfaces were scratched to ascertain film thickness. Roughness was measured away from the scratched regions. (a) 0% MHol, 5.4 nm RMS. (b) 33% MHol, 2.0 nm RMS (c) 0% MHol, 3.0 nm RMS, 6.2 nm thickness. (d) 100% MHol, 4.84 nm RMS, 18.1 nm thickness.

Composition (% MHol)	Roughness (nm RMS)	Roughness Standard Deviation (nm RMS)	r factor	r factor Standard Deviation
100%	15.0	8.8	1.11	0.06
83%	15.0	9.9	1.11	0.07
67%	14.5	9.1	1.30	0.07
50%	8.9	2.7	1.08	0.04
33%	8.5	10.7	1.14	0.27
17%	12.3	8.2	1.17	0.19
0%	6.2	1.1	1.13	0.08

Table 2. MHol/OT Nanoparticle Film Roughness Data

4.5 Wetting Behavior of Surfaces with Molecular Domains

Contact angle measurements were performed on the MHol/OT nanoparticle films using deionized water (Millipore, 18.2MΩ) and a DSA100 goniometer (Kruss GmbH). The work of adhesion for the water/nanoparticle film interface calculated from the contact angles is plotted below.

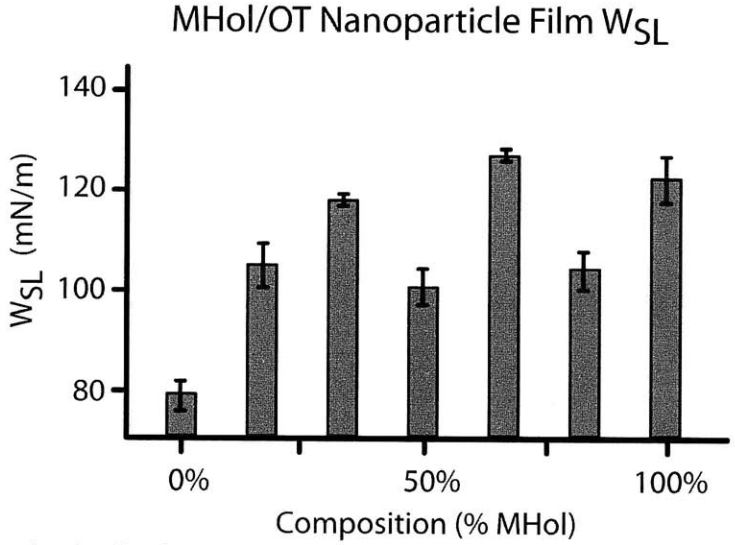

Figure 4. The work of adhesion (W_{SL}) of the water/nanoparticle film interface as a function of nanoparticle composition.

The trend measured deviates significantly from the linear relation expected from the Cassie-Baxter theory. Measurements of the interfacial energy trend were also made using SAM-AFM to confirm the validity of the contact angle trend. This set of measurements is plotted alongside the contact angle results in Fig. 5.

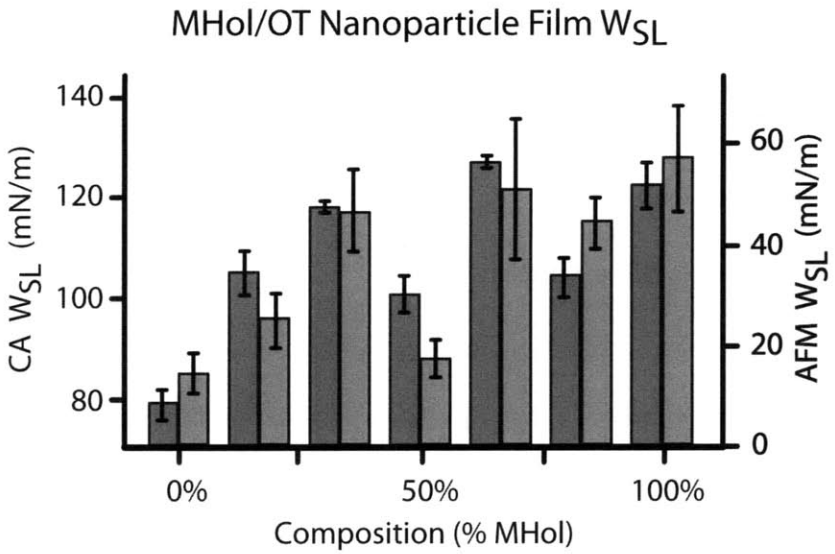

Figure 5. W_{SL} obtained from contact angle measurements (left, blue) is contrasted with W_{SL} obtained from SAM-AFM (right, red).

The trend obtained by AFM follows the trend obtained from the contact angle results. Most noticeably, this trend is strongly non-linear and further is non-monotonic. The fact that these two series agree is important since it demonstrably proves that the unexpected deviations obtained from contact angle are not due to defects in the film or contact angle pinning. The AFM technique measures the average work of adhesion over a small 40 nm square window away from the three-phase line. In addition to excluding pinning, this ensures several important conditions: First, mechanical deformation of the film can be ruled out as a cause of the deviation since the measurements are made away from the three-phase line. Furthermore, any other phenomena associated with the liquid-air interface, such as the presence of contaminants acting as surfactants during the contact angle measurements, can be assumed to not be the cause of the deviation. Second, as the window measured using the SAM-AFM technique is so small, the effect of roughness at larger length scales can be ruled out. Finally, the uniformity of the measurements ensures a homogeneous surface. That is, the variation within the surface exists at length scales smaller than the measurement window; the nanoparticles do not assemble into domain of

different wetting properties (as observed with the SAMs), so pinning at chemically inhomogeneous boundaries is not a cause of this phenomena. Thus, it can be safely concluded that this trend is genuine and not an artifact of the measurement technique.

4.6 MUDol/OT Nanoparticle Films

Nanoparticle films synthesized using a longer alcohol-terminated ligand, 11-mercaptoundecanol (MUDol) were produced following the same protocol as the MHol/OT nanoparticle films, with the only exception that the MHol was substituted with MUDol. These films serve as an interesting contrast to the MHol/OT films since the alcohol group projects further than the methyl group of OT. From the graph below (Fig. 6), the deviation from a linear trend is not as extreme (R^2=0.93).

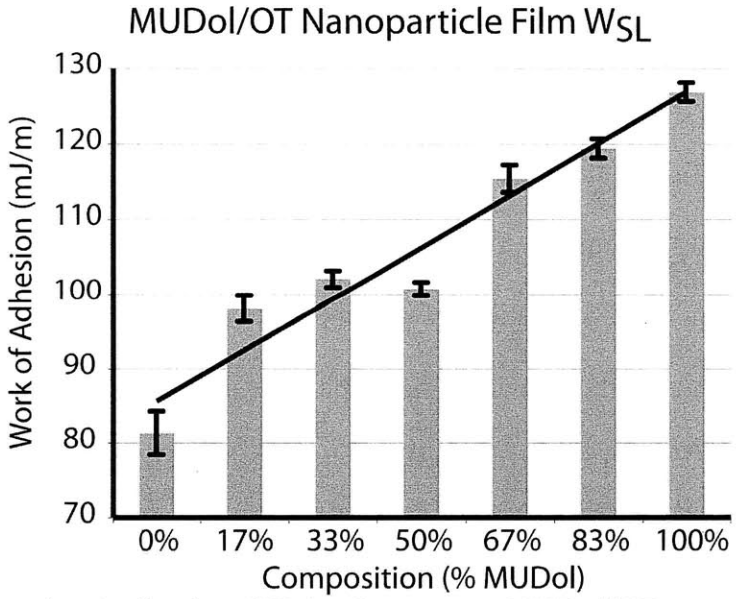

Figure 6. The work of adhesion (W_{SL}) of water on MUDol/OT nanoparticle films is plotted as a function of nanoparticle composition. In contrast to the behavior observed with MHol/OT nanoparticle films, this trend is comparatively linear (R^2 = 0.93).

4.7 Exploring Films with Other Chemistries

Nanoparticle films with other chemistries have been attempted, though with limited success. Two alternative hydrophilic groups of interest are carboxylic acids and sulfonic acids. Suitable ligands with carboxylic groups that are readily commercially available include 3-mercaptopropionic acid (MPA), 6-mercaptohexanoic acid (MHA), and 11-mercaptoundecanoic acid (MUA). Nanoparticles containing these ligands may be synthesized using the one-phase synthesis described in the previous chapter. The reagents are highly soluble in ethanol but the nanoparticles readily precipitate following synthesis. The resulting nanoparticles can be purified via vacuum filtration following precipitation. Commercially available ligands with sulfonic acid groups include 3-mercaptopropyl sulfonic acid (MPSA) and 11-mercaptoundecyl sulfonic acid (MUS). Nanoparticles may be synthesized from these ligands using the same one-phase synthesis in ethanol, with the exception of MPSA, with is synthesized in methanol due to its low solubility in ethanol.

These nanoparticles are highly soluble in water due to the presence of their highly polar, charged groups. The layer-by-layer technique employed for the alcohol-containing nanoparticles was used for these particles by using aqueous nanoparticle solutions. These attempts were deemed futile, as few to no particles were observed to adsorb to the functionalized glass surface. It was thought that the electrostatic repulsion from the charged surface prevented the formation of a complete layer. Another attempt used a solution of carboxylic acid containing particles in ethanol. By slightly acidulating the solution, the nanoparticles could be made soluble in ethanol. However, no significant assembly was observed to occur. This is most likely due to the inhibition of the formation

of thiolate species from the thiol groups on the cross-linker molecules. The presence of a thiolate intermediary is thought to be necessary for the place-exchange reaction that would link particles to the glass surface[8].

Another attempt at forming films from charged nanoparticles used the polyelectrolyte poly(allyl amine) (PAH). When dissolved in water, this polymer is positively charged and can be used to assemble layers with negatively charged polymer. An attempt to use this method to generate smooth, flat nanoparticle films was made by first depositing a thin film of PAH onto a glass slide, followed by a single layer of nanoparticles. Multiple layers can be deposited, but due to the intermixing of layers observed in polyeletrolyte multilayers in literature, a minimal film consisting of a single layer was desired. Significantly more nanoparticles adsorbed using this method compared to the previously described layer-by-layer attempt. However, a significant fraction of the surface remained uncoated by nanoparticles. Measurements made via tensiometry showed negligible differences across compositions, indicating the nanoparticles had minimal coverage. Representative images of the surfaces are shown below in Fig. 7.

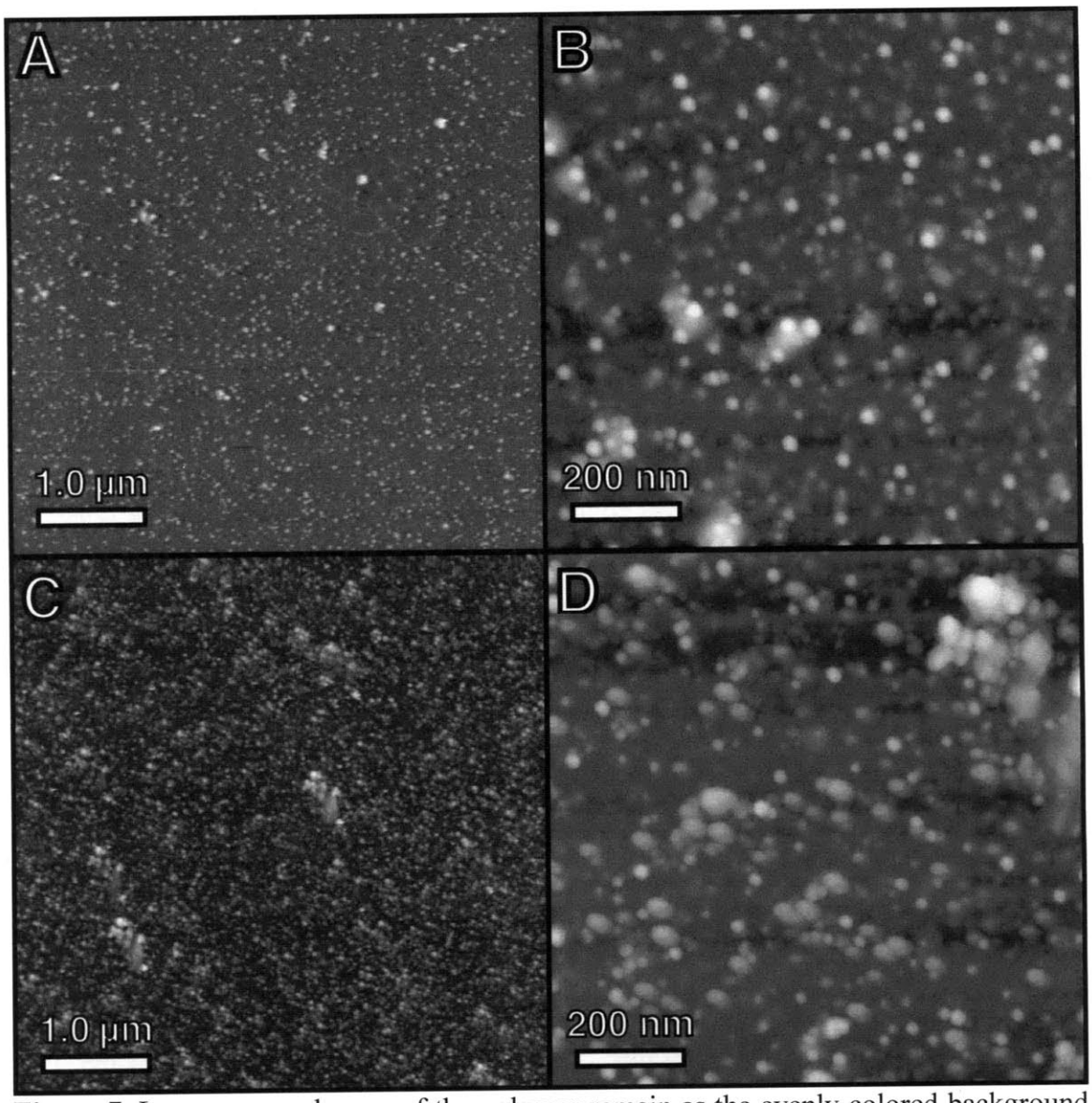

Figure 7. Large, exposed areas of the polymer remain as the evenly colored background of each image. Coverage in all samples is incomplete, and deposits of the polymer are visible as the shapeless protrusions from the surface. (a) 5:1 MPSA:OT. (b) 2:1 MPSA:OT. (c) and (d) 100% MPSA.

4.8 Results

Previous studies have tested the validity of the Cassie-Baxter expression for surfaces presenting large domains, namely bicomponent SAMs, and found the expression to be accurate.[9] The MHol/OT SAMs were observed to phase separate into domains with a minimum dimension greater than 5 nm. Both the contact results and the SAM-AFM

results found the interfacial energy varied linearly with surface composition ($R^2 = 0.96$). Due to the slight quadratic nature of this trend, possibly due to boundary region effects[10], a quadratic fit was also used. The R^2 of this fit was 0.940 for contact angle and 0.413 for SAM-AFM, exceeding the critical R^2 (α=0.001) for the number of degrees of freedom. An ANOVA analysis of the residuals (α=0.01) did not show a statistically significant relationship between compositions.

Furthermore, the trend obtained via contact angle measurements was linearly related to the SAM-AFM measurements ($R^2 = 0.947$). These results provide additional proof that the Cassie-Baxter relation holds for SAMs with large domains, and additionally demonstrates that the new SAM-AFM technique accurately measures the work of adhesion. The values calculated from the model of the SAM-AFM technique are not the same as the values derived from the contact angle measurements, but are related via a linear relation. The expression used to calculate the work of adhesion from the AFM data is sensitive to the geometry of the interface and tip, and other non-interfacial dissipative channels may exist. These factors are responsible for the larger error bars of the AFM results, and the disagreement in absolute value of the work of adhesion. However, using a series of samples, a conversion relation can be found to convert the SAM-AFM results to the work of adhesion that would be measured from contact angle or tensiometry.[5]

Having established that the Cassie-Baxter relation accurately models the interfacial energy of patchy surfaces with large domains, the analogous MHol/OT system presenting molecular-scale domains can be tested. Nanoparticle films were produced from

nanoparticles synthesized with the same thiol compositions as the SAMs. Using AFM, it was seen that complete coverage was obtained and there were no observed defects that could contribute to contact angle pinning. The average roughness of all films was 12 nm RMS. The variation between different slides of the same composition was at most 7.6 nm, and between different points on the same slide was 5.8 nm RMS. An ANOVA analysis of the films' roughness shows no statistically significant variation (α=0.05). Thus, variations in roughness would not account for variations of the work of adhesion between different compositions. Additionally, the *r* factor computed for these samples was not incorporated into the calculation of the work of adhesion for these films.

The contact angle measurements were taken on two slides from each composition, with 12 points per slide. A *t*-test (α=0.05) shows no statistically significant difference between the measurements on each slide. Thus, variations due to possible damage or defects on a single slide are not responsible for variations between different compositions.

The W_{sl} results of the nanoparticle films were analyzed similarly to that of the SAMs. A quadratic regression was performed on the contact angle and SAM-AFM data, with R^2 coefficients of 0.081 and 0.257 respectively, indicating a very poor fit. One notable feature of the trend of the work of adhesion of the nanoparticle films is that the trend is non-monotonic with respect to composition (Fig. 5). To test whether this non-monotonicity is statistically significant, an ANOVA analysis was performed on the residuals, showing a strong dependence between composition and the work of adhesion.

Of special interest is the prominent minima at 50% MHol. If the work of adhesion for the 50% MHol films is lower than the work of adhesion of the 33% MHol films, the trend is clearly non-monotonic. A t-test (α=0.01) of the SAM-AFM and contact angle values for the 33% MHol and 50% MHol nanoparticle films shows that this is indeed the case. In addition to the poor linear fit of the data, this non-monotonic behavior with respect to composition demonstrates that the Cassie-Baxter expression does not accurately model the interfacial energy of this system.

Additionally, the non-monotonicity is not due to a single composition. An ANOVA of the residuals from a linear fit of the SAM data show the regression describes the trend well, with F/F* of 0.338 and 0.053 for the contact angle and SAM-AFM data, respectively, with <1% confidence level. An ANOVA of the residuals of the nanoparticle film data shows a significant deviation from the fit, with F/F* of 23.7 and 1.87 for contact angle and SAM-AFM data, respectively. Removing a single composition from the contact angle and SAM-AFM data result in a minimum F/F* of 17.3, with the sole exception of removing the 50% MHol points in the SAM-AFM dataset, yielding an F/F* of 0.43. This final point is not surprising given the relatively larger error bars of the SAM-AFM data.[11]

The data of the MUDol/OT nanoparticle films was statistically tested in a similar fashion. While the trend did not stray from the predicted linear fit as markedly (R^2=0.93) as the MHol/OT system, the residuals were statistically significant. The residuals of the linear fit were found to be compositionally dependent (α=0.01) with an F/F* of 3.37.

Furthermore, the values for the 33% MUDol and 50% MUDol compositions were tested for non-monotonicity. A *t*-test (α=0.01) indicated the values are statistically dissimilar. Thus, the MUDol/OT system also exhibits non-monotonicity. Interestingly, the non-monotonicty is evident at the same composition range.

In conclusion, the work of adhesion trend observed for the nanoparticle films is not well described by Cassie-Baxter theory. The theory is successful modeling the interfacial energy of patchy surfaces of identical surface composition but with larger domains, highlighting the role of domain size in determining interfacial energy of a patchy surface. The trend is unexpectedly and non-intuitively non-monotonic. By ruling out surface defects and roughness, and via the agreement of two different measurement techniques, the deviation from the observed trend can be attributed to surface structure effects. The next chapter will discuss possible size-dependent mechanisms that cause these deviations from Cassie-Baxter theory.

4.9 References

(1) Bain, C. D.; Troughton, E. B.; Tao, Y. T.; Evall, J.; Whitesides, G. M.; Nuzzo, R. G. *Journal of the American Chemical Society* **1989**, *111*, 321-335.

(2) Prime, K. L.; Whitesides, G. M. *Science* **1991**, *252*, 1164-1167.

(3) Daniel, M. C.; Astruc, D. *Chemical Reviews* **2004**, *104*, 293-346.

(4) Stranick, S. J.; Parikh, A. N.; Tao, Y. T.; Allara, D. L.; Weiss, P. S. *The Journal of Physical Chemistry* **1994**, *98*, 7636-7646.

(5) Voitchovsky, K.; Kuna, J. J.; Contera, S. A.; Tosatti, E.; Stellacci, F. *Nat. Nanotechnol.* **2010**, *5*, 401-405.

(6) Zheng, N.; Fan, J.; Stucky, G. D. *Journal of the American Chemical Society* **2006**, *128*, 6550-6551.

(7) Kang, S. Y.; Kim, K. *Langmuir* **1998**, *14*, 226-230.

(8) Hostetler, M. J.; Templeton, A. C.; Murray, R. W. *Langmuir* **1999**, *15*, 3782-3789.

(9) Laibinis, P. E.; Bain, C. D.; Nuzzo, R. G.; Whitesides, G. M. *The Journal of Physical Chemistry* **1995**, *99*, 7663-7676.

(10) Woodward, J. T.; Gwin, H.; Schwartz, D. K. *Langmuir* **2000**, *16*, 2957-2961.

(11) Kuna, J. J.; Voitchovsky, K.; Singh, C.; Jiang, H.; Mwenifumbo, S.; Ghorai, P. K.; Stevens, M. M.; Glotzer, S. C.; Stellacci, F. *Nat. Mater.* **2009**, *8*, 837-842.

Chapter 5: The Breakdown of Cassie-Baxter Theory and Considerations for a New Theory

5.1 The Need for a New Theory

For the majority of experimental work, the theories of Wenzel and Cassie-Baxter have been given the greatest support due to their direct applicability. The Cassie-Baxter approach was originally developed to account for the non-wetting behavior observed of porous surfaces, and while the Cassie-Baxter approach is typically used in the case of extreme surface roughness[1,2], it in fact does not incorporate a measure of roughness as seen in Wenzel's approach.[3,4] Instead, it treats the rough surface as a heterogeneous surface presenting to the liquid a mixed surface comprised of trapped air pockets and the wetted, protruding asperities. As a theory describing heterogeneous surfaces, the Cassie-Baxter formula has been successfully applied to smooth surfaces expressing chemically inhomogeneous domains.[5]

In the preceding chapter, it was shown that for surfaces containing large domains, such as the SAMs, the Cassie-Baxter formula describes the interfacial energy well. Thus, for surfaces with large domains, the Cassie-Baxter approach is sufficient to capture the wetting behavior over the complete range of compositions. The data obtained on the nanoparticle films, which in contrast present molecular-scale domains, calls into question the applicability of the Cassie-Baxter approach for all heterogeneous surfaces.

The goal of this chapter is to demonstrate that interfacial energy has a structural component and to present an early understanding of the molecular-scale mechanisms responsible for this dependence. The structural component will be limited to the

organization of the chemical groups on the surface, that is, whether they are grouped in large or molecular-scale domains. Evidence for size-dependent wetting phenomena will be given followed by results from molecular dynamics simulations of the experimental system. Finally, additional experimental results will be given to support the wetting mechanisms posited to exist. A quantitative model has not yet been developed, but it is hoped that analyzing the wetting of complex heterogeneous interfaces in light of these mechanisms will enable the development of more refined quantitative models.

5.2 A General Framework

As discussed in the first chapter, the properties of the 'interfacial liquid', or liquid near the interface in a solid-liquid interface, varies from those of the bulk liquid. That is, the presence of the solid perturbs the equilibrium properties of the nearby liquid. In theoretical and computer models, the structure of the interface has been largely studied as the density profile as a function of distance from the solid surface. This profile is almost always calculated for a completely homogenous surface. For such a surface, the structure of the interfacial water is inherently one-dimensional. It has been observed that the nature of the solid greatly determines the density profile of the interfacial liquid: hydrophilic surfaces demonstrate a narrower transition length from interface to bulk, while hydrophobic interfaces are characterized by a region of low-density and a longer transition length.[6]

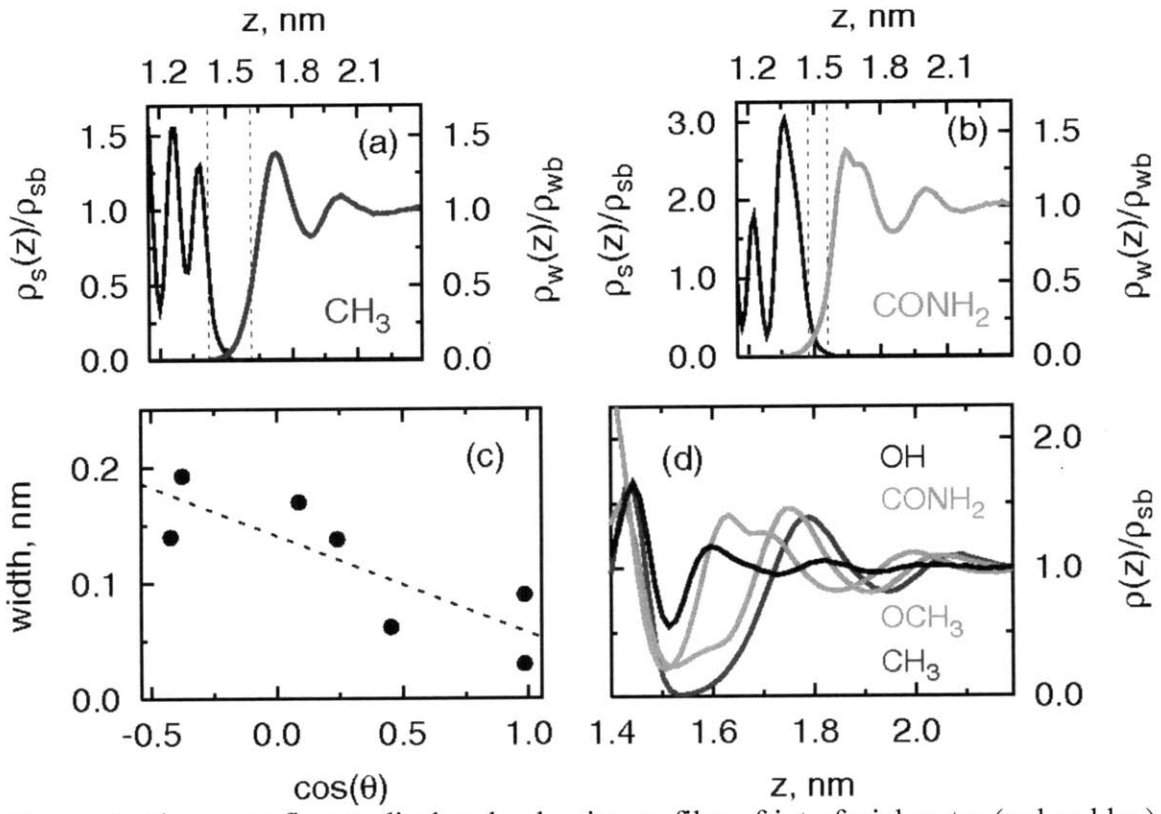

Figure 1. The upper figures display the density profiles of interfacial water (red or blue) for two different SAMs (black). The interfacial width, denoted by dashed lines, is seen to be greater for hydrophobic CH_3-terminated SAMs (blue) than for hydrophilic $CONH_2$-terminated SAMs (red). The interfacial thickness is correlated to the wettability of the surface, represented as the cosine of the contact angle, as shown in the lower left plot. Density profiles obtained with other terminal groups are plotted in the lower right. The hydrophobicity increases in the order $CH_3 > OCH_3 > CONH_2 > OH$. Note especially the difference between the OH and CH_3 density profiles. (Taken without permission from reference 6.)

For a heterogeneous surface, the density profile will vary perpendicular as well as parallel to the surface. This effect is most notable at the boundaries between chemically dissimilar domains, where the density profile must transition continuously from one domain to the next. In the case of large domains, where the domain size is much larger than this transition length, the density above each domain away from the boundary can be assumed to be the same as a surface composed entirely of that solid material. Near the domain boundaries, it is assumed a transition occurs from one density profile to the other. Support for this concept has been given by experimental work.[5] With the exception of the

boundary regions, the wetting behavior of each domain is independent of the rest of the interface. The Cassie-Baxter relation is accurate for such surfaces due to this separability.[1,7]

A surface with only molecular-scale domains can be equivalently viewed as a surface composed only of boundaries. The interfacial liquid structure will not resemble that of either homogeneous surface, but will more closely resemble the liquid near boundaries. The variation between large and molecular-scale domain trends is assumed to stem from this difference in interfacial liquid structure. To understand what size-dependent mechanisms may be responsible, each domain type will be treated independently whether it is solvophilic or solvophobic. As the majority of the research has been performed using water, the words hydrophilic and hydrophobic will be used instead, though the work can be generalized beyond water.

5.3 Cavitation and Solubility of Small Hydrophobic Objects

The interfacial energy of the hydrophobic domains will be analyzed first. The goal of this section is to identify how the size of a hydrophobic domain would affect the interaction between a liquid and itself. The most significant results regarding this topic come from solution theory, especially the studies of gas solubility in water. Experimental results show saturation concentration has a complex dependence on temperature and the presence of other solutes, and considerable theoretical effort has been made to interpret these trends.[8,9]

The process of dissolution of a solute can be conceptually decomposed into two distinct steps. In the first step, the liquid structure is kept frozen, and the solute is inserted into a volume capable of accommodating it. If no such volumes exist, the volume can be 'carved out' of the solvent. Once the solute is placed in the solvent, the solvent can then be relaxed and allowed to rearrange around the solute.[8,10] The volume that accepts a solute is termed a cavity. Whether or not solvation occurs is determined by the Gibbs free energy of the process, which can be split into the energetic cost of creating a cavity, the energy of the solute/solvent interactions, and an entropic component.

In the case of large objects, the interface and volume occupied are much larger than the size of the solvent molecules and can be well defined. A strong linear dependence exists between saturation concentration and surface area for solutes in this size range.[11] For large solutes, the formation of an interface, which includes breaking the hydrogen bonds that were present at the interface, dominates the energetic cost of cavity formation.[12] The process of cavity formation becomes more complex when the solute is commensurate in size with the solvent molecules themselves. In this case, the local fluctuations in solvent density that occur at equilibrium produce voids between the solvent molecules that can accept smaller solutes, analogously to the existence of vacancies in crystalline materials. Thus while enthalpic contributions dominate in the case of large solutes, entropy carries a larger role for small solutes.[13]

The length scale at which the transition from the small- to large-scale hydration occurs has been computationally determined to be approximately 1 nm.[14,15] The general schema

of these calculations closely follows the process outlined above: a solvent is simulated and the relative probabilities of inserting hard spheres of a given radius are calculated. From these probabilities, the Gibbs free energy of solvation can be calculated. The presence of ions or cosolvents can affect where this transition occurs, and in the case of water-ethanol, the transition point is relatively stable up to 40% ethanol. The addition of NaCl up to 2.0 M likewise has a minor effect on this length.[14] While the addition of cosolvents or ions may not affect the transition length, the excess Gibbs free energy is affected, modifying the saturation concentration Finally, it is important to note that this transition is not abrupt but is continuous.

The length scale at which this transition occurs, 1 nm, is the same length scale characteristic of the structured surfaces discussed in Chapter 2, including the nanoparticle films under study. As the interfacial energy component dominates the Gibbs free energy of this process, the interfacial energy of the solute can be found by dividing the Gibbs free energy of solvation by the solute's surface area. For large solutes, this ratio is constant and is equal to the surface energy of the liquid. For smaller solutes, this ratio is size-dependent and approaches zero as the size approaches zero (Fig. 2).

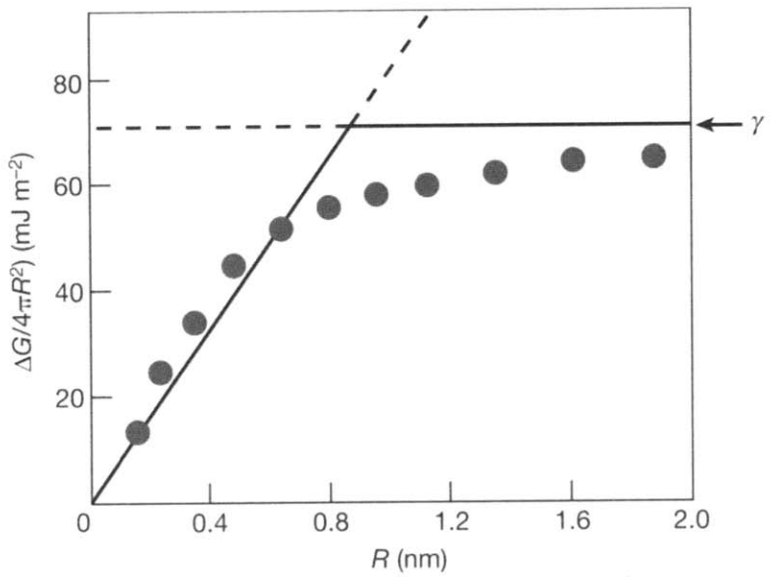

Figure 2. Gibbs free energy of cavity formation per unit surface area as a function of solute radius. For large solutes, the energy/surface area ratio approaches a constant equal to the surface energy of the liquid (γ). For smaller solutes, the energy rapidly decreases below approximately 1 nm. From reference 13.

This trend in effective interfacial energy shows the origin of size-dependence of the total interfacial energy. Hydrophobic domains that are below this transition length can be bridged by water and minimally perturb the hydrogen-bonding network. Thus, smaller domains are more easily wetted. Larger domains induce a greater restructuring of the liquid, reminiscent of that above homogenous hydrophobic domains. The interfacial energy contribution of larger domains would lie in the regime where interfacial energy is constant, as seen in the size agnostic Cassie-Baxter relation. It should be pointed out that while the structure of water is described as bridging over the molecular-scale hydrophobic domains, the structure of the water is dynamic and is in no way a rigid or static structure.[13]

5.4 Confinement: Liquid in Narrow Spaces

The wetting behavior of hydrophilic patches is expected to have a similar size-dependent relation. The behavior of water with nanostructured features has largely been studied via

modeling due to practical limitations associated with experimental work. The wetting and drying of patchy surfaces with molecular-scale hydrophilic domains has been extensively modeled.[16-20] These studies modeled surfaces presenting molecular-scale hydrophobic and hydrophilic patches, and found that the presence of hydrophilic groups greatly impeded drying of the surface, even when present in low concentrations. This behavior implies a non-linear relationship between overall wettability and the hydrophilic surface fraction, with sparser hydrophilic groups having a disproportionally large effect on interfacial energy.

From these models, it is not straightforward to isolate the effect of hydrophilic patch size on interfacial energy as clearly as the hydrophobic case. This is largely due to additional complexities present in the systems modeled. In all of the listed studies, molecular scale hydrophobic domains are simultaneously present, confounding the effect of the hydrophilic domains. Furthermore, one such study showed that patchy surfaces significantly resisted drying, but the geometry studied was two parallel surfaces 2 nm apart[16]; additional confinement effects are expected in this orientation.

Confined water and its modified dynamics is another topic that has been thoroughly modeled. Several studies have been carried out to investigate how the behavior of water varies when confined to a small volume. The confining system is most commonly a set of grooves in a material whose hydrophobicity/-philicity can be modified, though other geometries have been considered.[21-23] The primary outcome of this research is the demonstration that confined water exhibits markedly different dynamics than that of bulk

water. Experimental measurements of on inverse micelles confirm that the rheological properties of confined water differ from bulk water.[24] Furthermore, wetting/de-wetting transitions of water confined within nanotubes have been observed when the nanotube diameter is changed.[25] The geometry of these systems preclude extrapolation to the behavior of water on a flat surface.

Proteins have already been discussed as systems that possess nanostructured patterned surfaces of varying hydrophilicity. The water-protein interface has been extensively studied and modeled due to its importance in biological function.[26] Molecular dynamics simulations predict water at the protein surface would exhibit a different hydrogen-bonding structure and modified diffusivity.[27] Experimental measurements of interfacial water dynamics at the protein interface have confirmed that interfacial water behaves different from bulk water.[26] As proteins present a mixture of hydrophilic and hydrophobic domains but lack a means of tuning domain size or surface composition, the relationship between domain size and interfacial energy cannot be deduced directly from existing data.

5.5 Competing Interactions

Cavitation was shown to have a more pronounced effect as the hydrophobic domain size shrank. In turn, the effective interfacial energy of the hydrophobic domains would decrease. Thus if two interfaces have equivalent surface compositions, but one has large domains while the other has molecular scale domains (<1 nm), the system with molecular scale domains would be expected to have a lower interfacial energy and be more easily wet. Conversely, confinement would only be apparent where the hydrophilic domain size

is molecular scale. Contrary to cavitation, confinement effects are expected to make the surface less wetting due to the restriction of location and orientation of the interfacial liquid. Thus, the hydrophilic contribution to interfacial energy would be expected to increase when confinement effects are present.

These two effects act in opposite manners, depending on each component's domain size. The wetting of the different domain types has been treated independently, but cross-over effects are likely where both domain sizes are commensurate with the size of the wetting liquid, and thus the length-scale for wetting behavior transitions. Relating the structure of the system to interfacial energy requires understanding how domain size varies as a function of the monolayer composition. As discussed in Section 3.5, nanoparticles with intermediate compositions are expected to have a striated morphology, with the minority phase having the narrowest domains. In the 1:5 and 5:1 hydrophilic:hydrophobic compositions, molecular scale domains would be present only for the hydrophilic or hydrophobic components, respectively. The 2:1, 1:1, and 1:2 compositions will contain molecular-scale domains <1 nm, with slightly differing domain widths.[28,29] Since with the current knowledge it is impossible to deduce the magnitude of each effect, or how their interaction would affect their magnitudes, the relative shift of the interfacial energy at this composition cannot be predicted. Experimental results to be described later this chapter yield evidence that both effects are present, and appear to be very similar in magnitude.

5.6 Molecular Dynamics Simulations of Interfacial Water

Molecular dynamics simulations of striped nanoparticle systems were carried out in collaboration with Sharon Glotzer's group at the University of Michigan, Ann Arbor.

From this data, we were able to investigate whether the proposed mechanisms would be present in the system, and furthermore at which compositions each effect would be present. The system modeled was a single nanoparticle in a volume containing 12944 water molecules, with periodic boundary conditions. Three compositions (1:2, 1:1 and 2:1) of striped nanoparticles were modeled, each nanoparticle containing 362 ligands arranged on a sphere 4 nm in diameter. The SPC/E model for water was employed. Each ligand was modeled using the OPLS force field where the thiol groups were fixed, allowing the outer atoms to move. As a control for surfaces containing large domains, nanoparticles with the same composition but containing only two domains were modeled as well. The systems are represented in Fig. 3.

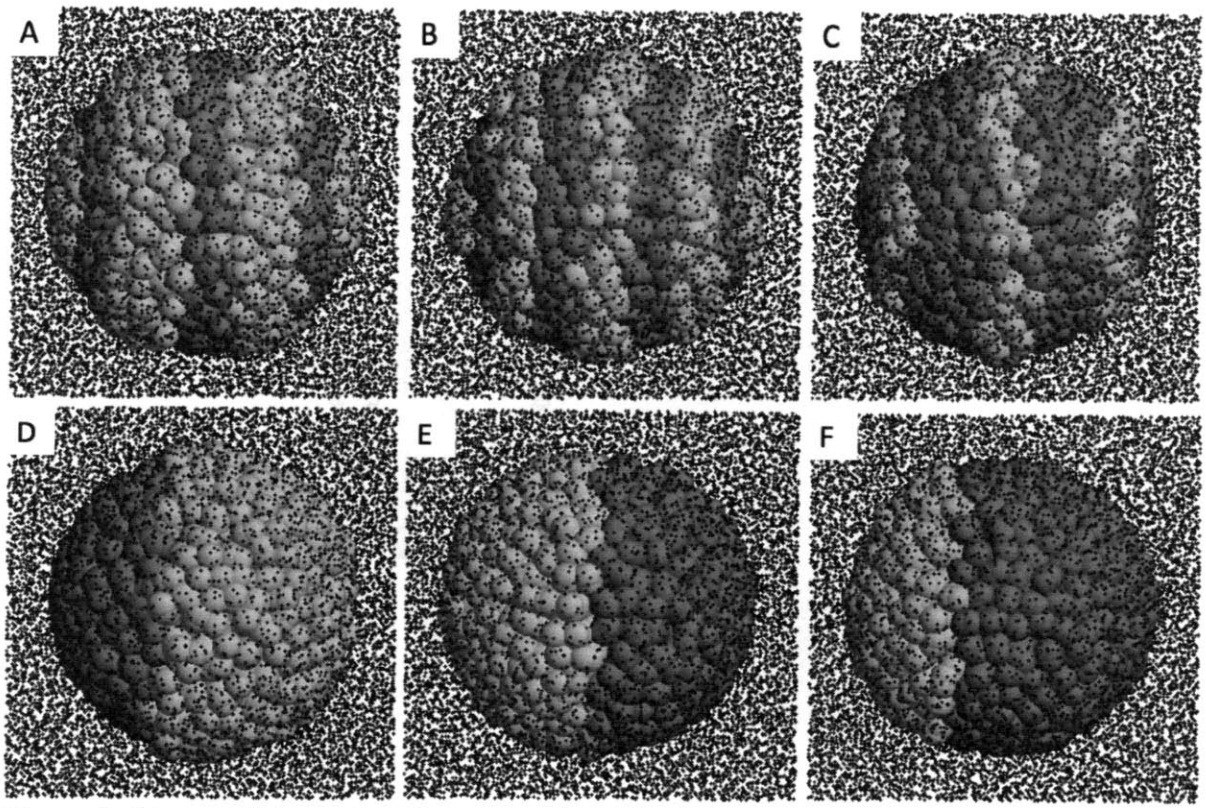

Figure 3. Nanoparticle systems in water. The red spheres correspond to MHol's alcohol headgroups white the yellow spheres correspond to the methyl headgroups of OT. (a-c) Striped nanoparticles and (d-f) Janus nanoparticles were both modeled, with the Janus

nanoparticles serving as a control group corresponding to large domain SAMs. Three compositions were used: (a,d) 33% MHol, (b,e) 50% MHol, and (c,f) 67% MHol.

From this data, the density of interfacial water was calculated by time averaging the position of the water molecules (namely the position of the oxygen atoms). Because all the systems exhibited cylindrical symmetry, density profiles could be calculated by averaging latitudinally. The results are shown in Figure 4; note that the color scale is not linear. In these plots, the density profile has been unrolled longitudinally, with each 'pole' of the sphere at 0° and 180°. In the case of the nanoparticles containing two single non-molecular scale domains (left), the density profile is constant within each domain, with a single transition occurring at the boundary between domains. For nanoparticles presenting a monolayer containing molecular scale domains (right). The profile appears corrugated, with hydrophobic groups lowering the water density near the surface. The differences in solvent density for other compositions are shown in Fig. 5.

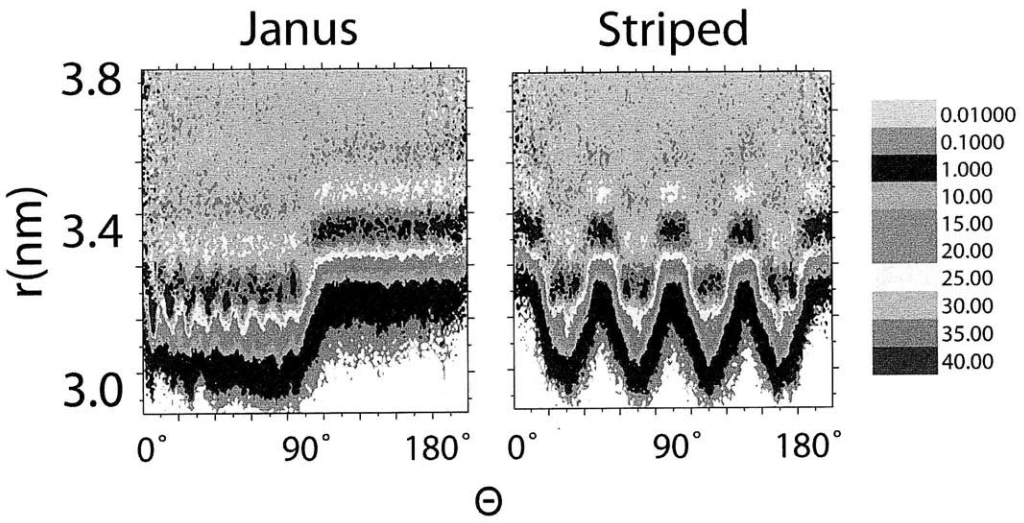

Figure 4. The water density profile around a 50% MHol Janus (left) and a 50% MHol striped (right) nanoparticle is plotted as a function of distance from the nanoparticle center and the longitudinal angle. For the Janus plot, the left half represents the volume above the hydrophilic ligands (MHol), while the right represents the region above the

hydrophobic ligands (OT). For the striped plot, the high and low areas represent the regions above OT and MHol stripes, respectively. Note the transition between domains at 90° in the Janus plot.

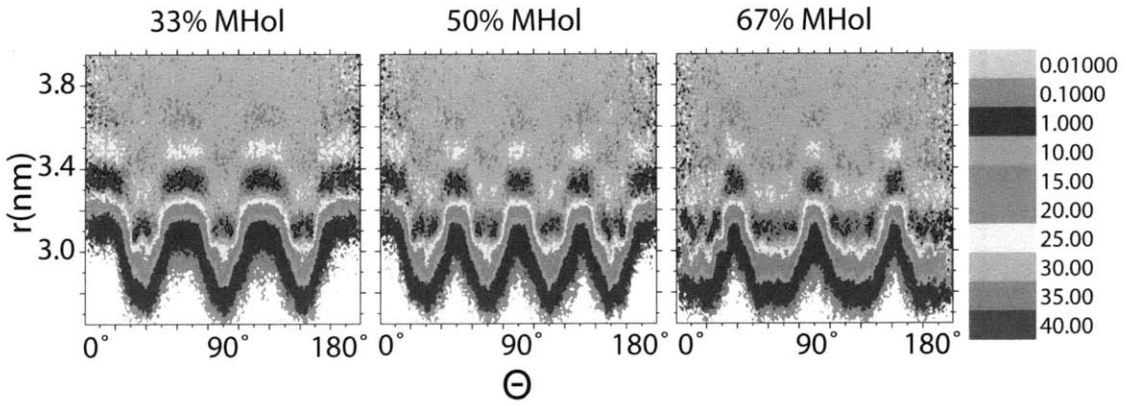

Figure 5. The solvent density around striped nanoparticles are shown for 33% MHol, 50% MHol, and 67% MHol. A sizeable portion of the water nearest the nanoparticle surface resembles the boundary region seen in the Janus nanoparticle.

These plots demonstrate the complexity inherent in describing the density above a nanostructured surface. The density over a large domain is well described by a one dimensional density function with a narrow transition occurring at the boundary between domains. When the domains become commensurate in size to the liquid, the density profile of the liquid above the molecular scale domains appears as a piecewise composite of the component density profiles with some deviations from the large domain system. Most notably, above narrow hydrophobic domains, the density of the interfacial water can be seen to be slightly higher than in the large domain case.

From these simulations, the presence of these effects can be quantitatively calculated by comparing the number of water molecules in a volume of interfacial water above each domain type. These trends are plotted in Fig. 6, one each for the hydrophobic domains and hydrophilic domains. Note that the average number between groups displays a large

disparity: This is due to the slight length difference between the ligands and the interfacial drying (or 'vacuum' layer) that occurs above hydrophobic surfaces.

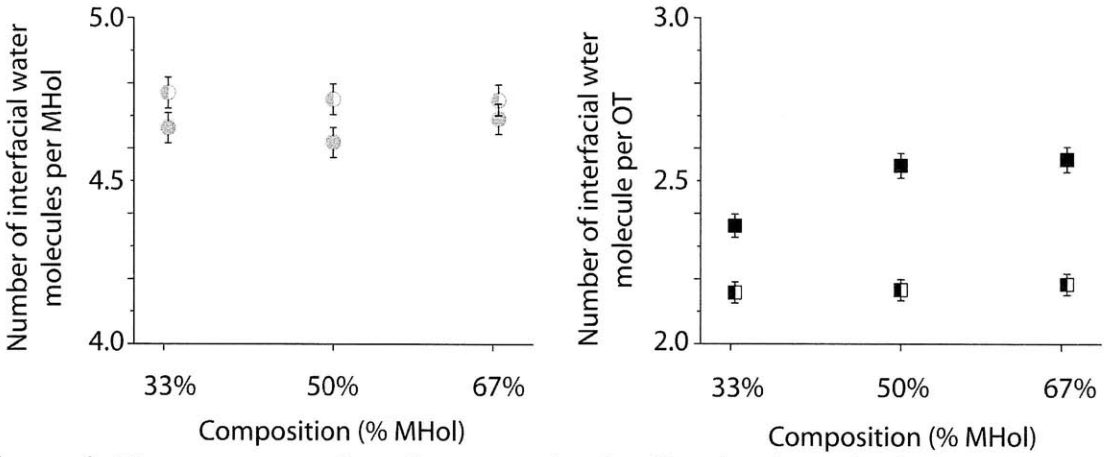

Figure 6: The average number of water molecules directly above the hydrophilic MHol (left) and hydrophobic OT (right) domains are plotted above for striped (filled) and Janus (half-filled) nanoparticles. The volume used for averaging extends a fixed distance from the center of the nanoparticle, leading to a lower average for the longer OT domains. The density for hydrophilic regions remains comparatively constant. The average density for the striped systems is slightly lower, and a small dip exists at 50% MHol. The effect of cavitation can be seen in the right plot, where the water density increases over the narrowest domains, as opposed to the larger domains of the Janus particles where more complete drying at the surface occurs.

The effect of cavitation is clearly seen in right plot of Figure 6. As the domain size decreases, the water density increases significantly. Furthermore, an interaction between neighboring domains is seen by comparing the 1:1 and 1:2 systems. Between these systems, the size of the hydrophobic domain is essentially constant, but the size, and consequentially density profiles, of the hydrophilic domains changes. This is revealed as a small density difference between the two systems. The density variation over the hydrophilic domains in various systems is not as clear as that observed above the hydrophilic domains, but is still statistically significant. Again, the density is presumably affected by both the size of the domain and interplay between the liquid wetting neighboring domains.

From these results, it is reasonable to assume that the proposed effects are present in the system under study and do significantly affect the density profile of the interfacial liquid of a nanostructured surface. From quantitative expressions of interfacial tension (or equivalently energy), the interfacial energy directly derives from variations in the density profile. Because the density profile of a mixed interface composed of large domains, such as the SAMs formed on flat substrates, greatly resembles the density profiles present on surfaces on homogeneous composition. The Cassie-Baxter expression is accurate for such surfaces (neglecting boundary corrections and pinning effects) because each domain possesses a single interfacial energy, and the total interfacial energy would reflect the compositionally weighted sum of each domain's interfacial energy. For the case of nanostructured interfaces, where the domains are commensurate in size to the liquid wetting them, the interfacial energy of each domain deviates from the expected value. Furthermore, it becomes difficult to discuss or isolate the interfacial energy of a single domain because the adjacent domains strongly affect the local density of water.

5.7 Experimental Confirmation

The wetting behavior of the nanostructured surfaces under study is posited to be controlled by two effects, which I have termed cavitation and confinement. In order to test whether the proposed effects were present, it would be necessary to shift the relative magnitudes of the effects. Cavitation is known to be less likely to occur when ions are present in solution.[14] The salting-out effect of hydrophobic molecules has been studied computationally[10] and experimentally.[30] The ability of each salt to vary composition is

described by the Setchenow equation, and salts can either increase or decrease solubility.[31,32]

To experimentally confirm that these effects are present, additional measurements were performed on the same surfaces using solutions of sodium chloride, which is known to impede cavitation.[10] It was observed that the shift for each surface was not proportional to the interfacial energy of the substrate, supporting the presence of the two proposed effects. The interaction of the salt solutions and the hydrophilic groups is not readily apparent and is likely more complex than that of the hydrophobic groups.

In addition to modifying the probability of cavity formation, the addition of a salt to water is known to affect the surface tension.[33] However, the difference in the liquid's surface tension is not sufficient to explain the variations observed in the work of adhesion. The work of adhesion is calculated from the Young-Dupré equation: $W_{SL} = \gamma(1+\cos(\theta))$. If the variation in the work of adhesion were due solely to changes in the surface tension (γ) of the liquid from the addition of the salt, the work of adhesion for all samples measured would scale with the same factor: the ratio of the liquids' surface tensions. This is not the case. Instead, it can be seen that the trend in deviations from the Cassie-Baxter expectation, graphically represented as the line fitted to the homogeneous compositions, varies significantly between the set of measurements made with pure water and water containing a salt, as shown in Fig. 7.

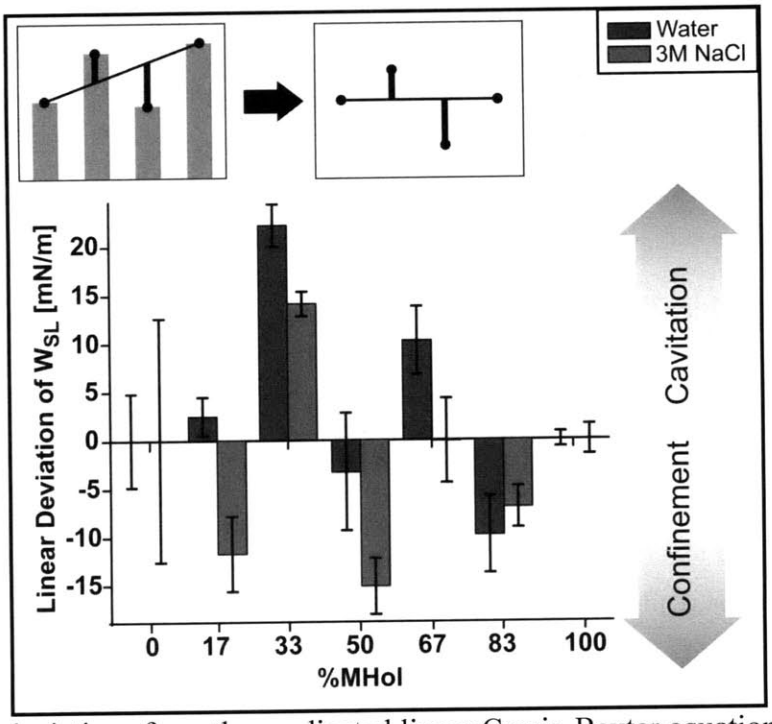

Figure 7. The deviations from the predicated linear Cassie-Baxter equation (see inset) are plotted for measurements taken with pure water (blue) and a 3 M NaCl solution (green). Deviations that were far from the predicted trend move closer to the linear fit (33%, 67% and 83%) while those that were near the predicted trend move further away (17%, 50%). This indicates two competing forces were responsible for the deviations.

To proceed with the analysis of the data, the deviations from the Cassie-Baxter formula are calculated (Fig. 7). The difference in the two sets of deviations represents the effect of reducing the effects of cavitation. Because the linear Cassie-Baxter relation describes the trend observed with surfaces bearing large domains, the deviations are interpreted as representative of the overall influence of the wetting mechanisms previously described. The deviations do not fall on straight line, as would be the case if they were due solely to surface tension differences between the salt and no-salt conditions. Furthermore, not all deviations occur in the same direction, supporting the co-existence of two effects that are opposite in magnitude.

The most curious point of Figure 7 is that of the 1:1 or 50% composition. At this point, both hydrophilic and hydrophobic domains are the width of a single molecule, and both effects are predicted to be strongly present. This point exhibited little deviation when measured when no salt was present, but a large deviation when measured with 3 M NaCl. This large difference indicates that both effects were present originally at similar magnitudes, essentially canceling each other out. The presence of salt reduced the effect of cavitation revealing the effect of confinement.[34]

5.8 References

(1) Cassie, A. B. D.; Baxter, S. *Trans. Faraday Soc.* **1944**, *40*, 0546-0550.
(2) Marmur, A.; Bittoun, E. *Langmuir* **2009**, *25*, 1277-1281.
(3) Wenzel, R. N. *Industrial & Engineering Chemistry* **1936**, *28*, 988-994.
(4) Wenzel, R. N. *Journal of Physical and Colloid Chemistry* **1949**, *53*, 1466-1467.
(5) Woodward, J. T.; Gwin, H.; Schwartz, D. K. *Langmuir* **2000**, *16*, 2957-2961.
(6) Godawat, R.; Jamadagni, S. N.; Garde, S. *Proc. Natl. Acad. Sci. U. S. A.* **2009**, *106*, 15119-15124.
(7) Good, R. J. *Journal of the American Chemical Society* **1952**, *74*, 5041-5042.
(8) Ben-Naim, A. *Solvation Thermodyanics*; Plenum Press: New York, 1987.
(9) Weiss, R. F. *Deep-Sea Research* **1970**, *17*, 721-735.
(10) Graziano, G. *J Chem Phys* **2008**, *129*, 084506.
(11) Hermann, R. B. *The Journal of Physical Chemistry* **1972**, *76*, 2754-2759.
(12) Stillinger, F. H. *J. Solut. Chem.* **1973**, *2*, 141-158.
(13) Chandler, D. *Nature* **2005**, *437*, 640-647.
(14) Rajamani, S.; Truskett, T. M.; Garde, S.; Chandler, D. *Proc. Natl. Acad. Sci. U. S. A.* **2005**, *102*, 9475-9480.
(15) Lum, K.; Chandler, D.; Weeks, J. D. *The Journal of Physical Chemistry B* **1999**, *103*, 4570-4577.
(16) Giovambattista, N.; Debenedetti, P. G.; Rossky, P. J. *J. Phys. Chem. C* **2007**, *111*, 1323-1332.
(17) Giovambattista, N.; Lopez, C. F.; Rossky, P. J.; Debenedetti, P. G. *Proc. Natl. Acad. Sci. U. S. A.* **2008**, *105*, 2274-2279.
(18) Luzar, A.; Leung, K. *J. Chem. Phys.* **2000**, *113*, 5836-5844.
(19) Leung, K.; Luzar, A. *J. Chem. Phys.* **2000**, *113*, 5845-5852.

(20) Imabayashi, S.; Gon, N.; Sasaki, T.; Hobara, D.; Kakiuchi, T. *Langmuir* **1998**, *14*, 2348-2351.
(21) Kondratyuk, P.; Yates, J. T. *Accounts Chem. Res.* **2007**, *40*, 995-1004.
(22) Schoen, M. *Phys. Chem. Chem. Phys.* **2008**, *10*, 223-256.
(23) Sacquin-Mora, S.; Fuchs, A. H.; Schoen, M. *J. Chem. Phys.* **2004**, *121*, 9077-9086.
(24) Fayer, M. D.; Levinger, N. E. In *Annual Review of Analytical Chemistry, Vol 3*; Annual Reviews: Palo Alto; Vol. 3, p 89-107.
(25) Kyakuno, H.; Matsuda, K.; Yahiro, H.; Fukuoka, T.; Miyata, Y.; Yanagi, K.; Maniwa, Y.; Kataura, H.; Saito, T.; Yumura, M.; Iijima, S. *J. Phys. Soc. Jpn.*, *79*, 4.
(26) Kasemo, B. *Surf. Sci.* **2002**, *500*, 656-677.
(27) Bizzarri, A. R.; Cannistraro, S. *J. Phys. Chem. B* **2002**, *106*, 6617-6633.
(28) Jackson, A. M. Ph.D. Thesis, M.I.T., 2007.
(29) Jackson, A. M.; Hu, Y.; Silva, P. J.; Stellacci, F. *Journal of the American Chemical Society* **2006**, *128*, 11135-11149.
(30) Smith, S. P.; Kennedy, B. M. *Geochimica et Cosmochimica Acta* **1983**, *47*, 503-515.
(31) Baldwin, R. L. *Biophys. J.* **1996**, *71*, 2056-2063.
(32) Hribar, B.; Southall, N. T.; Vlachy, V.; Dill, K. A. *Journal of the American Chemical Society* **2002**, *124*, 12302-12311.
(33) Collins, K. D.; Washabaugh, M. W. *Q. Rev. Biophys.* **1985**, *18*, 323-422.
(34) Kuna, J. J.; Voitchovsky, K.; Singh, C.; Jiang, H.; Mwenifumbo, S.; Ghorai, P. K.; Stevens, M. M.; Glotzer, S. C.; Stellacci, F. *Nat. Mater.* **2009**, *8*, 837-842.

Chapter 6: Conclusions and Future Work

6.1 Conclusion

The primary goal of this thesis has been to demonstrate a case where the conventional manner of interpreting interfacial energy of surfaces is not capable of capturing the behavior of surfaces with a higher level of complexity. The impact of this is potentially far-reaching, as a great deal of modern science is concerned with non-trivially patterned surfaces. The reason this effect has not been more thoroughly explored is due to the difficulty associated with fabricating surfaces with controllable surface features in the appropriate size range. Conversely, many naturally existing patchy systems, such as proteins, are not easily adapted to traditional methods of measuring interfacial energy.

This thesis opportunistically used an established material process with a novel material, striated nanoparticles. Circumventing the tendency of bicomponent monolayers to phase separate into large domains was made possible by forming monolayers on small gold nanoparticles. While the experimental technique employed in this thesis produces films with these properties, the resultant films occupy a very narrow slice of the entire domain of applicable surfaces, and only serve as a demonstration of the failure of the Cassie-Baxter theory.

Via molecular dynamics simulations, the local solvent structure was examined and was found to be domain size dependent. Rather than the simplistic homogeneous domains envisioned in traditional Cassie-Baxter theory, the liquid near the surface was in the vicinity of numerous chemically dissimilar domains. The small domain size does not

permit the simplifying assumptions made in Cassie-Baxter theory. Instead, the entire neighborhood can influence local wetting properties in a complicated and yet unclear manner.

The most immediate question raised by this work is: If the Cassie-Baxter model is insufficient for calculating the interfacial energy of multi-component surfaces, what should replace it? Developing a quantitative expression for interfacial energy that is applicable to surfaces with domains of all shapes and sizes, any surface morphology including roughness, any surface chemistry, and for any liquid is the ultimate goal. Such a goal is rather lofty as interfacial energy is most likely not well described by a few parameters characterizing the liquid and surface, but is instead an emergent property of a more complex system. Such complexity is not apparent when the system under study is itself simple, as would be the case of the single component-single liquid systems studied in an effort to parameterize interfacial energy, as discussed in Chapter 1. This chapter will outline avenues of research that the current work opens, with a brief discussion of considerations relevant to each.

6.2 Future Experimental Directions

Departing from the current system under study, there are multiple directions of research open that would illuminate the role of structure on interfacial energy. The liquids studied so far have had similar sizes and behavior. Notably, water and glycerol form very strong hydrogen bonds between themselves. An interesting topic of study would be observing how the mechanisms presented would vary if the solvent molecules were much larger. As most solvents are of similar size, such effects would not be commonplace in nature. This

route could, however, produce a model experimental system where the magnitude of the effects are exaggerated, making them easier to isolate. Furthermore, more interesting liquids, possessing a more definite structure themselves, could be study. Liquid crystals and ionic liquids could have the orientations significantly modified by the underlying substrate. The organization imposed by the surface on the interfacial liquid could propagate further into the liquid, and such substrates could be technologically useful to modify the local behavior of liquid crystals.

Another route to generating a larger field of data to inform a new model of interfacial energy relies on modifications of the substrates studied. For instance, the MHol:OT series of films demonstrated a non-monotonic trend in interfacial energy, whereas the similar MUDol:OT set of films had a less non-monotonic trend. The appearance of non-monotonicity is especially intriguing as it does not follow conventional predictions and is unintuitive. The difference in length of the ligands was posited to be responsible for the non-monotonicity observed in the previously two systems: the longer hydrophilic ligands were both solvophilic and flexible, preventing the proposed mechanisms of cavitation and confinement from determining wetting behavior. A large systematic study generating films with all possible length variations would produce a mapping of the degree of non-monotonicity. Understanding the transition from monotonic to non-monotonic behavior would be useful in explaining drying of patchy surfaces.

In addition to pinpointing the transition from monotonic to non-monotonic behavior, such a large systematic study on ligand length would enable calculations of the 'blurriness' of

the longer ligand, akin to the measurements of the boundary width performed on partially grown SAMs. In this study, partially formed hydrophobic SAMs were grown on hydrophilic gold substrates. By analyzing the deviation from the Cassie-Baxter prediction, the width of the boundary, or transition, region between the monolayer and the substrate could be estimated. This was found to be similar to the length of the ligand itself. Such a result makes sense, as the edge ligands would be able to stand perpendicular or lie parallel to the substrate. This measurement in effect measures the length of the protrusions from the surface, or more accurately the volume the protrusion is capable of occupying. If this mode of analysis were to be applied to the striped nanoparticle system where the length margin of the two ligands is known, the relative effects on protrusion mobility may be studied. By knowing the expected volume occupied *vs.* calculated volume occupied, the restrictedness of the protrusions may be calculated. This can produce an additional means of quantifying the magnitudes of confinement and cavitation.

As water is such an important solvent, especially in biology, the effect of different salts on wetting is an important topic to study. Trends in anion/cation size and charge could be studied by numerous measurements using a variety of salts in water at a number of concentrations. Such measurements would be especially useful in establishing whether or not specific ion effects occur in the case of wetted striped-nanoparticles. Specifically, whether or not ions have a non-negligible role in the confinement effect could be determined, as ions of different sizes would have different behavior when confined.

Furthermore, as ions have a strong effect on cavitation frequency, the charge and size of the ions should greatly determine the extent of this effect.

Finally, measuring the wetting behavior of striped nanoparticle films composed of charged ligands would be useful in estimating the strength of the proposed effects when the hydrophilic group has significantly stronger interactions with the liquid. As the partial films produced using charged nanoparticles were highly wetting, and as a very wide range of charged nanopartcle compositions are water soluble, it can be assumed that the majority of such charged films are very wetting and thus would have similarly low interfacial energies. Further study is warranted since a majority of biological interfaces are composed of charged groups. The presence of strong electrostatic interactions is important, because such strong interactions may overwhelm any slight energetic benefit or cost from the proposed mechanisms. If the electrostatic interactions are indeed dominant, these effects can be ruled out or minimized in the understanding of structured surfaces with charged groups. More likely however, surface structure effects would remain in the presence of charged groups, and the structure of the interfacial liquid would be complicated by yet another consideration. To accomplish this experimental work, a method for producing stable, smooth, complete films of charged nanoparticles must be developed. As discussed in Chapters 2 and 3, in the current body of work, such films presented numerous difficulties preventing their inclusion in the interpretation the interfacial energy of structured surfaces.

6.3 Extending the work computationally

Similar to mapping the parameter space experimentally, an interesting project would be modeling all similar variations. The wetting effects could be isolated and linked definitively to the underlying substrate structure. Such a result would generate a new structure-aware relation for interfacial energy. This expression would be useful to estimate interfacial energy of other systems without the time required for MD simulations.

A recent report has associated the frequency of cavity formation with a surface's hdyrophobicity. This analysis is quite provocative because it correlates the wettability and thus interfacial energy of an interface to a parameter than can be readily measured computationally. Whereas other computational modeling investigations into wettability focused primarily on the average liquid density profile near the surface as discussed in the first chapter, this method can capture the time-dependent fluctuations inherent in the liquid. The variation in cavity formation at the surface has been shown to be a far better predictor of wetting behavior.[1] It would be interesting to simulate surfaces similar to the striped nanoparticle films and to calculate the surface wettability directly from the cavity statistics. As the original paper correlated their computational results to experimental measurements of interfacial energy, extracting interfacial energies of the simulated systems should be achievable. This new technique has already been applied to protein systems with intriguing results.[2] This work has the potential to overturn the conventional hydrophobic/philic scales used to understand protein interfaces.

In addition to extending the basic science of interfacial energy, computational modeling could be useful in understanding and exploring solvent driven self-assembly. If a computationally efficient model of interfacial energy could be developed in the manner stated above, it would facilitate the development of a gradient approach method to exploring hydrophobic effect based self-assembly. This would extend on Tanford's original concept that protein assembly is driven by minimization of interfacial energy. A more efficient estimator of interfacial therefore would allow for rapid prototyping of self-assembled systems. This could enable more efficient design of patchy particle and peptide systems

This thesis demonstrated an unexpected non-monotonic trend in interfacial energy on composition. This trend is nonintuitive and demonstrates that interfacial energy may exhibit bistability dependent on structure. In self-assembling systems, this can lead to a kineticly trapped state, where the system remains on one side of the dip because rearranging would reduce the wettability transitionally and thus be energetically disfavored. Such nuances in assembly would not be accessible with coarser models of interfacial energy.

6.4 Link to Biology

As physiological conditions include a moderate concentration of a variety of salts, understanding the role various salts, or even combinations of salts, have on the interfacial energy is important to understanding how interfaces affect biological systems. One particular question remains unanswered since first posed in 1888. The so-called Hofmeister series of anions studies the effect of anion charge, size and concentration on

the saturation concentration of proteins. While the resulting effect is not identical for all proteins, the results are so similar that the aptitude of each ion to 'salt in' or 'salt out' proteins is essentially constant.[3] Proteins are charged molecules, but the salt concentration effect is separable from the colloidal stability trend calculable from DLVO theory. Interestingly, increased salt concentration does not always decrease the protein saturation concentration—some salts actually increase the solubility of proteins. These results, in addition to the sensitivity of size and charge of the ions, as well as the demonstrated link between ion concentration, cavity formation and surface tension, indicate a possible link between the Hofmeister series and cavity formation. As protein interfacial energy is not easy to experimentally measure, a more exact model of interfacial energy that encompasses the protein's surface structure may elucidate the relationship between structure and solubility.

In addition to proteins, there are artificial molecules that have important roles in biological interactions. Poly(ethylene oxide) (PEO) has a simple structure, but several reports indicate it has a hydration shell similar to proteins. PEO is also unique in that it is a well-known example of non-monotonic behavior.[4] The oxygen is capable of hydrogen bonding and is classified as mildly hydrophilic while the intervening methylene groups are clearly hydrophobic. It would be expected a polymer with one intervening methylene group would be more soluble than PEO. This is actually not the case, as PEO is significantly more water-soluble than the polymers with one more or one less methylene unit. This has been linked to the local structure of water. Extending the concepts

developed for 2-dimensional surfaces to quasi 1-dimensional systems like these polymers would enable predictions of polymer solubility.

PEO additionally is technologically important, as it is a highly protein resistant surface. It is theorized that its hydration shell prevents proteins from adsorbing, as prior to adsorption, the hydration layer would need to be stripped from both the protein and polymer. Other protein resistant surfaces have also been discovered[5]; in general, these surfaces are neutrally charged and have a mixture of chemical groups that is on average hydrophilic. Understanding the interfacial energy, and more specifically the structure of the interfacial liquid, of such substrates would enable a unified understanding of protein resistance and aid further design of protein resistant coatings.

6.5 Technological Applications

While the current work is not technologically applicable, it is not difficult to see opportunities where the current findings may be employed to design surfaces with new, useful properties. In addition to the previously mentioned technological applications (surfaces that control the alignment of liquid crystals, developing tools for the design of self-assembling systems, more soluble molecules, and protein resistant surfaces), a more thorough knowledge of the structural effect can enable the design of super-hydrophobic coatings. As discussed in Chapter 1, superhydrophobic coatings utilize a hierarchical approach where intrinsically non-wetting coatings are enhanced by incorporating additional levels of roughness. A mixture of two components may exist where not only is the trend of interfacial energy against composition non-monotonic, but that there is a minimum at an intermediate composition. That is, a mixture of the two components is

less wetting than either component alone. This may provide a method to produce a chemical coating to enhance the overall hydrophobicity of the surface.

6.6 References

(1) Godawat, R.; Jamadagni, S. N.; Garde, S. *Proc. Natl. Acad. Sci. U. S. A.* **2009**, *106*, 15119-15124.

(2) Acharya, H.; Vembanur, S.; Jamadagni, S. N.; Garde, S. *Faraday Discuss.* **2010**, *146*, 353-365.

(3) Cacace, M. G.; Landau, E. M.; Ramsden, J. J. *Q. Rev. Biophys.* **1997**, *30*, 241-277.

(4) Israelachvili, J. *Intermolecular and Surfaces Forces: Second Edition*; Second ed.; Academic Press: Boston, 2000.

(5) Prime, K. L.; Whitesides, G. M. *Science* **1991**, *252*, 1164-1167.

Appendix A: Experimental Methods

A.1 SAM Preparation

The following procedure was employed to generate all SAMs used, and is generally applicable to any mixture of alkylthiols. Gold on mica (Agilent) was cut to produce coupons approximately 1 cm square. The surfaces were cleaned by immersion in room temperature piranha solution (3:1 sulfuric acid:hydrogen peroxide) for 15 minutes. Longer times were found to have an adverse effect on surface roughness and also promoted delamination of the gold layer from the mica substrate. Following the brief immersion, the substrates were rinsed with deionized water (Millipore, 18.2 Mohm) and dried under a stream of nitrogen. The samples were placed in vials containing 10 ml of 0.1 mM thiol solutions in ethanol. The vials were kept at room temperature for 7 days, when the samples were removed and rinsed with ethanol.

A.2 Nanoparticle Synthesis

In a 150/100 ml round bottom flask, in an oil bath set to 60 C and constantly stirred:

80 ml DCM	
thiol mixture (see below)	2 mmol
494.7 mg $HAuPPh_3Cl$	1 mmol

When the solution approaches boiling point of DCM (39 C), add:

869.7 mg t-butylamine borane complex	10 mmol

Cap tightly using yellow plastic cap, secured using a flask holding arm. Preferably, use a high pressure, sealable reaction vessel. Allow the reaction to proceed for 1 hour. Remove from heat after 1 hour. When at room temperature, precipitate and clean particles using centrifugation.

Thiol Quantities

The left column expresses the quantity of the individual thiol in mmol. The thiols included here are 6-mercaptohexanol (MHol), 11-mercaptoundecanol (MUDol), 1-octanethiol (OT), 1-decanethiol (DT), 1-nonanethiol (NT), and 1-dodecanethiol (DDT).

	MHol	MUDol	OT	DT	NT	DDT
mw	134.24	204.37	146.29	174.35	160.32	202.4
d	0.981	s	0.843	0.824	0.842	0.845
2.00	273.7	408.7	347.1	423.2	380.8	479.1
1.67	228.1	340.6	289.2	352.6	317.3	399.2
1.33	182.5	272.5	231.4	282.1	253.9	319.4
1.00	136.8	204.4	173.5	211.6	190.4	239.5

0.67	91.2	136.2	115.7	141.1	126.9	159.7
0.33	45.6	68.1	57.8	70.5	63.5	79.8
0.00	0.0	0.0	0.0	0.0	0.0	0.0

*Quantities in the above table are expressed in units of ml, except in the case of solids (s), which are expressed in mg.

It was found repeated centrifugation (5 times, 45ml DCM or Et_2O) were sufficient to clean the particles. In the case of the nanoparticles containing alcohol groups, it was found that 0.25-0.5 ml of EtOH and brief sonication would greatly aid in dispersing the pellet prior to addition of 45 ml of diethyl ether, the poor solvent used to precipitate these particles. The particles can be washed several times this way until an acceptable level of purity is achieved. NMR analysis of the resulting dried particles cleaned using 5 rounds of centrifugation showed negligible amounts of impurities.

For nanoparticles containing a charged group, such as the sulfonic acid 3-mercaptopropyl sulfonic acid, a different synthetic method must be employed: Add the thiols (0.45 mmol total, example quantities given below) to 100 ml MeOH in 250 ml r.b. flask. Sonicate to dissolve. (Note: OT = octanethiol)

	OT (uL)	MPSA (mg)
hOT	78.1	
1:5	65.1	13.4
1:2	52.1	26.7
1:1	39.1	40.1
2:1	26.0	53.5
5:1	13.0	66.8
hMPSA		80.2

Add 177.2 mg $HAuCL_4$ (0.45 mmol) and sonicate to dissolve. Stir continuously.

In a separate beaker, add 250 mg $NaBH_4$ to 50 ml MeOH. Agitate or sonicate briefly to dissolve. Fresh $NaBH_4$ must be used and the solution should actively bubble. Add the reducing solution dropwise to the gold/thiol solution. Stir for 20 min after addition is complete. The particles can be easily cleaned via vacuum filtration and thorough washing with methanol.

A.3 NMR Analysis

Dissolve 10-20 mg of purified NP sample in 0.850 ml d-DMSO, D_2O, or $CDCl_3$ as appropriate depending on nanoparticle composition and sonicate to dissolve fully. Confirm absence of free thiol first with ^1H NMR (300 MHz Varian). Free thiol and other contaminants, including solvent that was not removed, will be easily visible as sharp peaks.

Decomposition of the particles can be performed using two different methods. With iodine, a solution of 10 mg in 10 ml $CDCl_3$ is prepared and a volume of this solution appropriate for the amount of nanoparticles to be decomposed is added to the solvent from the NMR tube from the previous step. Sodium cyanide or potassium cyanide may also be used. Approximately 20-30 mg can be added to water or DMSO, depending on the nanoparticle solution solvent. Decomposition is complete once a precipitate forms. If a non-deuterated solvent was used, the solvent must be removed by rotovap or vacuum, and replaced with a deuterated solvent. Acquire spectra with ^1H NMR (500 MHz Varian).

Composition is determined most easily using the peaks from the methylene adjacent to the terminal functional group or methyl group, using the methylene adjacent to the thiol group to check the quantities.

A.4 NP films

This technique is rather flexible and numerous substrates may be used. For glass substrates, the silane molecule 3-mercaptopropyl trimethoxylsilane (3-MPTMS) is used to functionalize the surface. This compound reacts with hydroxyl groups present on the surface. Freshly cleaned and highly hydrophilic borosilicate glass slides and coverslips were used in this thesis. The procedure to prepare the substrate is as follows: The surfaces are cleaned first by hand using isopropanol to remove surface contaminants left from the slide production and handling. After the slides are dried, they are placed in a piranha bath (4:1 sulfuric acid : hydrogen peroxide (30%)) for 45 minutes. It is important that the slides are copiously rinsed with water so that no piranha solution remains. To accomplish this, a holder was built that allowed flushing the samples under a stream of deionized water in an inverted position. While remaining in an inverted position, the samples are dried completely using a hot air gun. Slides are inspected and washed and dried again if necessary.

To deposit the silane, the samples are placed, still inverted and still in the holders, into a dessicator containing 4 opened vials, each containing approximately 100 uL of 3-MPTMS. A vacuum is drawn and the samples are exposed to the 3-MPTMS vapors for 45 minutes. Any visible, white marks on the surface indicate polymerization. Substrates may be salvaged with extensive sonication in acetone, though it is best to discard slides with defects.

Following silanization, the glass substrate is exposed to a nanoparticle solution and the first layer is allowed to adsorb. The solvent used to produce the nanoparticle solution depends on the composition of the nanoparticle monolayer. Ethanol is an excellent solvent for particles with alcohol groups, while toluene is an excellent solvent for particles displaying primarily methyl groups. The formation of each layer is complete within 24 hours.

To continue growth, the nanoparticle films are placed in a solution containing linear dithiol molecules. The selection of the dithiol will depend on the monolayer thickness of the nanoparticles. 1,9-nonanedithiol was used for the films in this thesis. These molecules

can bond to the gold cores of two different nanoparticles, and thus will serve as a cross-linker. When the nanoparticle film is placed into the dithiol solution, the dithiol molecules replace thiols in the nanoparticle monolayer. After partial substitution, the nanoparticle film will have several thiol groups on the surface. When placed in the alternate solution, nanoparticles in solution can bind to the surface using these thiol groups. This process can be repeated to produce several layers. The final layer of nanoparticles deposited is not exposed to the dithiol solution. In this way, the nanoparticle monolayer presented on the surface of the nanoparticle film can be assumed to be identical to the monolayer of the original, unsubstituted nanoparticles.

For charged nanoparticles, the following method was attempted: A glass slide or coverslip is again used as the substrate. The substrate is cleaned in a solution of 3:1:1 water:hydrogen peroxide (30%):ammonium hydroxide, yielding a negatively charged surface. The substrate is immersed in a solution containing a charged polymer (1%wt pollyallylamine hydrochloride in water) for 15 minutes. The polymer adsorbs to the surface giving the surface a positive surface charge. The sample is rinsed with water and immersed in a solution of negatively charged particles for a minimum of 15 minutes, during which nanoparticles adsorb to the surface. Finally, the films are thoroughly rinsed and dried.

Biographical Note

Jeffrey J. Kuna received a Bachelor of Science degree in Mechanical Engineering from Northwestern University in June, 2004. At MIT, he studied under Professor Francesco Stellacci. He served as a teaching assistant for the undergraduate course 3.012, "Fundamentals of Materials Science and Engineering". With Francesco Stellacci, he co-instructed 3.153, "Nanoscale Materials". His publications are listed below.

Kuna, J.J., Voitchovsky, K., Singh, C.; Jiang, H.; Mwenifumbo, S.; Ghorai, P.K.; Stevens, M.M., Glotzer, S.C.; Stellacci, F. "The Effect of Nanometre-Scale Structure on Interfacial Energy", *Nature Materials*, 10, 837-842, 2009

Voïtchovsky, K.; Kuna, J.J.; Antoranz Contera, S.; Tosatti, E.; Stellacci F. "Direct mapping of the solid-liquid adhesion energy with sub-nanometer resolution", *Nature Nanotechnology*, 5, 401-405, 2010

Hung, A.; Mwenifumbo, S.; Mager, M.; Kuna, J.J.; Stellacci, F.; Yarovsky, I.; Stevens, M. "Ordering Surfaces on the Nanoscale: Implications for Protein Adsorption", *JACS*, accepted.